A high-throughput experimental and computational approach for high voltage Mn-based spinel materials exploration

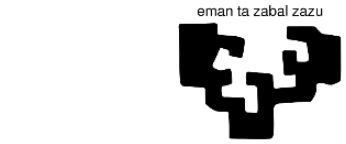

Universidad del País Vasco
Euskal Herriko Unibertsitatea

Author:

Iciar Monterrubio Santin

Co-directors:

Montserrat Casas Cabanas

Amaia Saracibar Ruiz Ocenda

2023

eman ta zabal zazu

Universidad del País Vasco
Euskal Herriko Unibertsitatea

CIC energiGUNE
MEMBER OF BASQUE RESEARCH & TECHNOLOGY ALLIANCE

A high-throughput experimental and computational approach for high voltage Mn-based spinel materials exploration

Doctor of Philosophy by:

Iciar Monterrubio Santin

Supervisors:

Montserrat Casas Cabanas

Amaia Saracibar Ruiz Ocenda

Marine Reynaud

A Gonzalo,

'Todos somos polvo de estrellas'.

Acknowledgements

It would not be possible to carry out this extensive work without many of you and I want to thank you for the professional and personal support of many of you, and, of course, I want to thank the **Basque Government** for my PhD grant (PRE_2021_2_0160).

I want to thank firstly all the **women in science** that have been examples and references for me to keep fighting and understanding that I can be here. I want to thank from Ada Lovelace, the first computer programmer, till the women that nowadays surround me. I thank my supervisors, Montse, Amaia and Marine for this opportunity, for believing in me and for being part of this references of women leading science. It would not be possible to say how much I have learnt from you in so many different disciplines. **Marine**, aunque no aparezca tu nombre en la portada de este libro para mi eres una más de mis directoras de tesis. Has estado ahí desde el primer momento con tu ilusión y pasión intrínsecas hacia la ciencia. Desde ese diciembre de 2018, cuando comencé a trabajar de técnica de laboratorio, que llegué al CIC como una niña rodeada de juguetes que quería aprenderlo todo, hemos compartido numerosos momentos a nivel científico y personal. Siempre recordaré el principio de esta aventura a tu lado. Tu fuiste la primera en apoyarme para hacer un doctorado y la que se sentó conmigo en los sofás para explicarme que iba a comenzar también una aventura computacional, me asusté, y aquí estamos. **Montse** gracias por enseñarme que la calma y la compostura es la mejor amiga en los momentos de incertidumbre y por apoyarme en los momentos duros con ternura y cariño. Me sorprendes cada día y me siento muy afortunada de trabajar contigo. **Amaia**, tu guía y apoyo han sido esenciales para mí, especialmente para el trabajo computacional realizado tan desconocido para mi cuando empecé. Estoy profundamente agradecida por tu dedicación a todos los niveles.

También quiero agradecer su apoyo y aportación a este trabajo a los coautores de algunas partes de este manuscrito. **Eku**, Evaristo, coautor, compañero y, sobre todo, amigo, ya van 12 años de aventuras juntos, me cuesta decidir en qué sección ponerte. Sin ti

Batteryino habría sido una mera ilusión abstracta. Cuantas horas en cursos de Arduino por las tardes cuando todos se iban a su casa a descansar, cuantas horas de peleas con nuestros brazos robóticos, la impresora 3D, la CNC, las bombas, … Gracias por tu apoyo infinito a nivel laboral y personal. Quien habría dicho que con todas aquellas horas de saltarnos clases para comer tostadas en Granada nos iban a traer hasta aquí. **Isma**, gracias por tu curiosidad y tus ganas de ayudar, sin ti Batteryino habría sido un reto más lejano. Gracias a **Javier Carrasco** por toda su ayuda y apoyo con la parte computacional que tan lejana se me hacía al comenzar la tesis. Y gracias a **Oier L.** por su inmensa ayuda con los cálculos generados y con todas las dudas que se me han planteado en este tiempo, he aprendido mucho de ti y gracias por tu apoyo a nivel personal y por preocuparte por mí. **Marcus**, el alemán menos alemán que he conocido, me ha encantado compartir nuestros viajes a ALBA y te agradezco infinitamente tu disponibilidad constante para ayudarme cuando lo he necesitado. Estoy deseando compartir más ciencia, conversaciones sobre viajes y vidas alternativas, y cervezas contigo. También quiero agradecer su trabajo y consejos a **Aitor H**., sin tí quién sabe cuánto habría tardado en identificar esos *antisite defects*.

Quiero agradecer su trabajo desde RR.HH. a **Elena V.** por todas sus sonrisas al llegar cada día durante estos 5 años en el CIC y por sus gestiones no solo para que el centro vaya bien si no para que nosotras estemos bien. A **Aloña** que ha permitido y trabajado para que podamos patentar nuestro material. A **Asier** por creer también en mí y abrirme las puertas. Gracias a **Esti, Mercedes**, **Cristina**, **Miriam**, **Leire** y a todas las demás por participar en que el centro funcione. A **Ana M.** por su escucha y apoyo.

Especialmente quiero agradecer su trabajo para mejorar el centro a todas las personas que han pasado y están en el **comité de empresa**. No siempre es fácil y siempre supone un esfuerzo extra en un día a día en el que todas estamos hasta arriba de trabajo. Me alegro de haber compartido este camino durante un tiempo con vosotras. Mi agradecimiento y admiración también a todas las mujeres que participan y hacen posible el women in science. Gracias **Maica** por unirnos a todas.

Gracias a **JuanLu** por guiarme hasta Vitoria, aunque los caminos se separasen han sido muchos los momentos disfrutados juntos. Y, gracias a **Jon** y **Carlos** por proponerme en una noche etílica mandar mi CV al CIC allá por junio de 2018. I also want to thank all my colleagues and friends from CIC for their company during all these years. Without the coffees, the meals, the tears and the shared laughter, everyday life would not have been the same. Gracias a **Mikel, Jean-Luc, Oier A., Alfonso, Jon, Rosalía, Dome, Grazia, Edurne, Montse G., Alex, Rocio, Manar, Remy, Paul, Damien, Simon, Ade, Pedram, Naiara, María J., Sona, Begoña, Nuria, Pedro, Luis A., Luis, Iñigo, Ivan, Afshin, Sam, Nagore, Marina, Aitor, Fran, Artem, Roshan** y a tantos otros.

A mis compas del protocorner, **Guillermo, June, Nestor, Ander, Silvia** y **Laida** por todas las risas y apoyo y, sobre todo, comida compartida, incluso la llegada de lugares cuestionables para Nestor. Y MUY especialmente gracias a **Esti, Marian, Gelines, Sergio, Migue, Ainhoa, Maha, Nico, Joseba** y a nuestros eramus **Coca, Eku, Carlos** y **Violeta**. Que gran placer compartir mi vida con todos vosotros. Tantos momentos compartidos que no tengo palabras para describir cuando os quiero y cuanto os agradezco estar en mi vida. Gracias a **Álvaro** por estar siempre ahí para todo lo que ha pasado en mi caótica vida desde que te conozco, gracias por estar para cervezas y risas, pero sobre todo gracias por estar ahí cuando las risas se hacen lejanas.

Gracias a mi cuadrilla de Romo, mis hippies preferidos en el mundo, mis brujas. Gracias **Elena, Bitxor, Aitor, Bego** y demás ortigueiros. Por los viajes hechos, los que vendrán y por nuestra futura ecoaldea. Por estar ahí en todos los momentos importantes. Gracias a **Mari** e **Ire** por apoyarme incondicionalmente y ayudarme a tomar perspectiva y ordenar mis ideas. Gracias a las dos por creer en mí y en mi locura. Por seguir cumpliendo años juntas. Gracias a **Blanca** por sus visitas, por nuestras noches de chino y por estar ahí incluso para limpiar cuando yo no puedo. Este camino empezó a tu lado cuando nos mudamos a Euskadi. Y, gracias a todas las personas que habéis estado cerca estos años acompañandome: **Gio, Mayte, Layla, Elena, Neus, Flippy, Tami, Ana V., Kenari,**

Carlos, Julen, Marina, Lasas, Vero, Matil, Andrea, Ane, Lorea, Lau, los clowns, Mo, Susana (endoeuskadi)**.**

Gracias a **Maria** y **Bamba** por abrirme las puertas a su casa y a Senegal, a **Hiwa** y al pueblo iraní, y gracias a tantas otras personas que me han acogido durante todos los viajes que he realizado estos años. Me ha dado fuerzas para seguir adelante y creer en las personas.

Mi más sincero agradecimiento a mis mujeres de Llena de mí y La tribu por estar en lo más profundo. **Nora**, lo que creas es mágico. Gracias **Ibo, Patti, Sara, Eider, Ainhoa, Ane, Garazi, Lauren, Aide.** Gracias a **Alba** por además abrirme a todos los ámbitos de su vida y ser mi compañera de aventuras por el desierto.

Y, por su puesto, gracias a mi familia por su apoyo y por estar siempre disponibles para mí. A mis padres, **Juan y Conchi**, por escucharme en los momentos más oscuros, por todos los tuppers para que pudiese trabajar más tiempo, por facilitarme siempre todo. A **Pilar** por estar siempre ahí para escucharme en mis rareces y darme nuevas perspectivas. A mi hermano, **Héctor**, tú me advertiste lo difícil que era esta senda, gracias a ti y a **Noe** por estar mi vida. A todos mis abuelos, y especialmente a **Julio** y **Vicenta**, de los que he aprendido más de lo que se puede aprender en los libros. Gracias por enseñarme a trabajar duro y a la vez a disfrutar de la vida y ponerme en el centro. Y gracias a **Hipa**, por darme besos, alegrarse siempre que estamos juntas y por sacarme a pasear tres veces al día incluso cuando no he sido capaz de soltar la tesis.

Gracias a **Gonzalo**, esta tesis te la dedico a tí, aunque no puedas leerla, la siento tan tuya como mía y siempre has sido la primera persona que esperaba que la tuviese.

Por último, me doy las **gracias a mí** por haber atravesado todos los momentos difíciles, que no han sido pocos, por haberme atrevido a conocerme mejor y seguir avanzando.

RESUMEN

En la próxima década, a medida que las aplicaciones sigan creciendo, se espera que aumente significativamente la demanda de baterías recargables que sean respetuosas con el medio ambiente. Las baterías de iones de litio son actualmente las baterías recargables más potentes y de mayor capacidad disponibles y se espera que mantengan su posición de liderazgo en el futuro previsible. Sin embargo, todavía es necesario aumentar su densidad energética y durabilidad, así como abordar los problemas de seguridad intrínsecos de esta tecnología hoy en día. Sin embargo, el enfoque manual convencional para el descubrimiento de materiales requiere mucho tiempo y es costoso. Por lo tanto, hay una necesidad apremiante de métodos innovadores y herramientas mejoradas para acelerar la identificación y comprensión de nuevos materiales para baterías. De hecho, se prevé que la combinación de detección computacional de materiales, técnicas de experimentación de alto rendimiento y la integración de inteligencia artificial (IA) dentro de las plataformas de aceleración de materiales (MAP) acelerará notablemente el proceso de descubrimiento y desarrollo de nuevos materiales para baterías en un futuro próximo.

Durante esta tesis, en primer lugar, se ha desarrollado con éxito una plataforma autónoma para la síntesis eficiente de materiales inorgánicos electroactivos con capacidades de alto rendimiento. Esta plataforma permite utilizar una amplia variedad de enfoques sintéticos como sol-gel, pechini y estado sólido. Integra un módulo interno, llamado Batteryino-I, creado de forma casera, que permite la mezcla de reactivos minimizando la manipulación manual y ofreciendo versatilidad, además permite realizar actualizaciones de forma sencilla, acordes a las nuevas necesidades que puedan surgir. La cantidad de muestra sintetizada suele ser de entre 200 y 500 mg, lo que distingue esta plataforma de otros enfoques, como los de película fina o de gota, en los que se produce una cantidad mucho menor de muestra final. Este enfoque permite que todas las caracterizaciones se puedan realizar en la misma muestra

garantizando así la representatividad. Además, Batteryino-I permite la síntesis de doce muestras de forma simultánea. La efectividad y reproducibilidad de esta plataforma se demuestra mediante el estudio de dos sistemas: (i) examinando los parámetros estructurales para la síntesis sol-gel de $LiFe_{0.5}Mn_{1.5}O_4$ y (ii) realizando la síntesis combinatoria sol-gel en el sistema de óxido Li-Mn-Ni. Los resultados obtenidos demuestran la importancia de esta plataforma automatizada y su papel en el avance crucial hacia el desarrollo de plataformas de aceleración de materiales autónomas para el desarrollo de materiales inorgánicos.

Tras el desarrollo de Batteryino-I, la espinela $LiFe_{0.5}Mn_{1.5}O_4$ ha sido seleccionada para su estudio debido a su funcionamiento a altos voltajes, así como por su bajo coste y su mayor sostenibilidad en comparación con otros materiales comúnmente usados en baterías de iones litio. El $LiFe_{0.5}Mn_{1.5}O_4$ exhibe una capacidad teórica de 148 $mAhg^{-1}$ y funciona a voltajes de más de 5 V frente a Li/Li^+. Para comprender mejor este material se ha llevado a cabo una investigación teórico-experimental de sus propiedades estructurales y electroquímicas.

Desde un punto de vista teórico se ha estudiado la estabilidad de fase y la evolución del voltaje de diferentes distribuciones metálicas Fe/Mn en el $LiFe_{0.5}Mn_{1.5}O_4$ durante la deslitización/litiación utilizando cálculos de teoría funcional de la densidad (DFT) con dos enfoques diferentes: el funcional Perdew-Burke-Ernzerhof (PBE) más la corrección empírica U de Hubbard (PBE+U) y el funcional con aproximación restringida y normada adecuadamente (SCAN). Los hallazgos indican que la distribución de metales de transición dentro de $LiFe_{0.5}Mn_{1.5}O_4$ tiene un impacto mínimo en su estabilidad de fase y comportamiento de voltaje, y sugieren que el proceso electroquímico se lleva a cabo a través de un mecanismo de solución sólida. La actividad redox, estudiada mediante cálculos de carga Bader y cáculos de densidad de estados, de $Li_xFe_{0.5}Mn_{1.5}O_4$ está principalmente gobernada por el par redox $Mn^{3+/4+}$ en el rango de $1 \geq x \geq 0.5$, mientras que el par redox $Fe^{3+/4+}$ opera en la región de $0.5 \geq x \geq 0$. Una investigación adicional del proceso redox revela

una contribución aniónica que, en el caso del funcional SCAN, se muestra reversible.

A este análisis computacional ha sido seguido de un estudio experimental de alto rendimiento, mediante el uso de Batteryino-I, en el que se ha sintetizado $LiFe_{0.5}Mn_{1.5}O_4$ en diferentes condiciones estudiando una selección de parámetros sintéticos (temperatura de recocido, tiempo de recocido, rampa de enfriamiento, rampa de calentamiento, tiempo de formación de gel, posición en el módulo automatizado, posición en el horno y exceso de Li añadido al inicio de la síntesis) y sintetizando un total de aproximadamente 150 muestras de $LiFe_{0.5}Mn_{1.5}O_4$. Durante este estudio se ha prestado especial atención a la caracterización estructural de los materiales obtenidos y su correlación con los parámetros de síntesis utilizados. Empleando diversas técnicas de caracterización como la Microscopía Electrónica de Barrido (SEM), la Espectroscopía Mössbauer, la Difracción de Rayos X (XRD), la Difracción Neutrónica de Polvo (NPD), así como la Espectroscopía de Absorción de Rayos X Extendida (XANES) y la Espectroscopía de Absorción de Rayos X con Luz Sincrotrón Extendida (EXAFS), se ha podido obtener una comprensión detallada de las propiedades y estructuras de las muestras estudiadas. La caracterización estructural reveló porcentajes distintos de hierro en posiciones tetraédricas, conformando defectos de tipo *antisite* entre las posiciones de Fe y Li. La presencia de este tipo de defectos ha sido asociada con una expansión estructural. Los estudios electroquímicos realizados han demostrado que las muestras con menos defectos *antisite* generan un rendimiento superior, con un *plateau* redox de Fe más prolongado, una mayor capacidad de descarga y una mayor retención de capacidad mostrando la gran la importancia del control de la síntesis para optimizar la eficiencia del almacenamiento de energía.

Además, el estudio in operando de Difracción de Rayos X sincrotrón (DRXs) ha permitido confirmar el mecanismo por solución solida sugerido por el estudio teórico. Gracias al análisis de los procesos redox realizado in operando de Espectroscopía de Absorción de

Rayos X (EAX), se confirmaron los dos procesos redox distinguidos mediante el estudio teórico a aproximadamente 4.0 V y 5.0 V respecto a Li/Li^+ atribuidos a los procesos redox de $Mn^{3+/4+}$ y $Fe^{3+/4+}$, respectivamente.

Gracias a los conocimientos adquiridos mediante los estudios teórico y experimental, el $LiFe_{0.5}Mn_{1.5}O_4$ sintetizado, con baja cantidad de defectos, opera a voltajes de hasta 5.1 V frente a Li/Li^+ y ofrece capacidades de hasta 130 $mAhg^{-1}$ a una velocidad de descarga 1D con un voltaje promedio de 4.4 V. Estos resultados son los más altos reportados hasta el momento para este material y, además, representan una densidad de energía de hasta 572 Wh/kg (y potencialmente capaz de presentar >660 Wh/kg). Este valor sería superior al del comercial $LiNi_{0.6}Mn_{0.2}Co_{0.2}O_2$ (622NMC), que posee capacidad de descarga de 170 $mAhg^{-1}$ a voltaje de corte de 4.3 V y con un voltaje promedio de 3.8 V. Además, el $LiFe_{0.5}Mn_{1.5}O_4$ da como resultado una reducción del 66% de los elementos críticos (Li, Ni, Co).

En resumen, esta tesis representa una contribución significativa a la investigación de materiales y tecnología de almacenamiento de energía. La combinación de enfoques teóricos y experimentales de alto rendimiento ha permitido una comprensión integral de $LiFe_{0.5}Mn_{1.5}O_4$ como un material prometedor para baterías de iones de litio. El desarrollo de la plataforma Batteryino-I y la investigación subsiguiente resaltan la importancia de la automatización y el control de la síntesis para optimizar la eficiencia en el desarrollo de nuevos materiales para el almacenamiento de energía. Además, los resultados de este trabajo alientan una mayor investigación sobre el $LiFe_{0.5}Mn_{1.5}O_4$, con su excepcional estabilidad, rendimiento mejorado y bajo costo, como una opción interesante para la próxima generación de baterías de iones de litio respetuosas con el medio ambiente de alto voltaje.

Esta tesis allana el camino hacia la innovación acelerada en el campo de los materiales para baterías, ofreciendo una visión

integral de cómo abordar los desafíos clave en el desarrollo de baterías más potentes, seguras y sostenibles.

SUMMARY

Lithium-ion batteries (LIBs) currently stand as the most performant rechargeable batteries in the market although increasing their energy density, durability, sustainability, and safety is still needed. To accelerate materials discovery, high-throughput (HT) computational and experimental techniques are required, as the conventional manual approach is time-consuming and costly.

In this thesis, an autonomous platform has been successfully developed for the synthesis of inorganic materials with HT capabilities. It integrates an in-house built module that enables the mix of reagents minimizing manual handling. This platform allows to synthesize, following different synthetic approaches (i.e., sol-gel, pechini and solid-state), 200-500mg of 12 samples simultaneously, ensuring that all characterizations are done on a single batch to ensure representativeness. The efficiency of this platform is showcased by performing sol-gel synthesis of two systems: (i) $LiFe_{0.5}Mn_{1.5}O_4$ (LFMO), to evaluate different synthetic parameters, and (ii) the Li-Mn-Ni oxide system to explore a part of the phase diagram.

The high voltage LFMO spinel has been further studied in detail. This system was selected due to its environmental friendliness and low cost, as well as, for exhibiting a theoretical capacity of $148mAhg^{-1}$ and operating at high voltage (c.a. 4.4 V *vs*. Li/Li^+ in average). To understand its electrochemical behavior, a computational analysis considering different Fe/Mn distributions has been performed. Structural parameters and electrochemical behavior including phase stability, voltage evolution and redox processes upon (de)lithiation has been evaluated. Afterwards, a HT experimental screening of synthetic parameters has been done focusing on the impact of synthetic parameters and antisite defects on LFMO's structural and electrochemical properties, showcasing the importance of controlled synthesis in minimizing antisite defects to optimize its energy storage efficiency. By the combination of theoretical and HT experimental approaches this thesis sheds light to comprehensively understand LFMO behavior as a promising material for LIBs.

List of Acronyms, Symbols and Fundamental Constants

A: surface area, *A*.

AI: artificial intelligence

C(D)-rate: charge-discharge rate

CASM: clusters approach to statistical mechanics

CC : constant current

CCCV : constant current constant voltage

CE: coulombic efficiency

CNC: Computer Numerical Control

C-rate: charge rate

DFT: density functional theory

DMC: dimethyl carbonate

DMC: dimethyl carbonate

DOS: density of state

D-rate: discharge rate

DW: Distilled water.

$E^{0,(-)}$: negative electrode potential in standard conditions

$E^{0,(+)}$: positive electrode potential in standard conditions

E^0: Standard electrode potential

$E_{Li_{x1}Fe_{0.5}Mn_{1.5}O_4}$: total energy per formula unit of the least lithiated phase in LFMO

$E_{Li_{x2}Fe_{0.5}Mn_{1.5}O_4}$: total energy per formula unit of the most lithiated phase in LFMO

EC: ethylene carbonate

EES: electrochemical energy storage

E_{Li}: total energy per Li atom of bulk *bcc metallic Li*

EMC: ethyl methyl carbonate

ESSs: energy storage systems

EVs: electric vehicles

EXAFS: extended X-ray absorption fine structure

F.u.: formula units

F: Faraday constant

GGA: Generalized Gradient Approximation

Hcp: high cell parameter

HT: high throughput

HTS: high-throughput synthesis

I: total current flowing through an electrode,

ICP: Inductively coupled plasma

IS: isomer shift

J: Current density

LCMO: $LiCo_{0.5}Mn_{1.5}O_4$

LCO: $LiCoO_2$

Lcp: low cell parameter,

LDA: Local Density Approximation

LFMO: $LiFe_{0.5}Mn_{1.5}O_4$

LFP: $LiFePO_4$

Li/V_{Li}: Li vacancies

LIBs: Lithium-ion batteries

LMO: $LiMn_2O_4$

LNMO: $LiNi_{0.5}Mn_{1.5}O_4$

MAPs: Materials Acceleration Platforms

Mcp: medium cell parameter

mGGA: meta-generalized-gradient approximation

MGI: Materials Genome Initiative

Mi: Mass of reactants

n: number of transferred electrons

NCA: $LiNi_{1-x-y}Co_xAl_yO_2$

NMC: $LiNi_{1-x-y}Co_xMn_yO_2$

NMP: N-Methyl-2-pyrrolidone

NPD: Neutron Powder Diffraction

p: Specific power

PBE: Perdew-Burke-Ernzerhof

PBE+U: Perdew-Burke-Ernzerhof plus the empirical Hubbard U correction functional

PC: propylene carbonate

PDOS: projected density of states

PEGDME: poly(dimethoxy ethylene glycols)

PEO: poly(ethylene oxide)

PITT: Potentiostatic Intermittent Titration Technique

$P_{V:}$ Power density

PVDF: polyvinylidene fluoride

PVDF-HFP: polyvinylidene fluoride-hexafluoropropylene

Q: Charge capacity

QS: quadrupole splitting

$Q_{V,th}$ Theoretical charge density

$Q_{V,th}$: volumetric energy density,

R: distance in XAS

Redox: reduction-oxidation

SCAN: Strongly Constrained and Appropriately Normed

SEM: Scanning Electron Spectroscopy

ss: Debye Waller factor

SSCE: solid state ceramic electrolytes

SSPE: Solid-state polymer electrolytes

sXRDP: Synchrotron X-ray powder diffraction patterns

U: cell voltage

VASP: Vienna Ab initio Simulation Package

Vi: Volume of the reactants

WE: Working electrode

WID: line width

XANES: X-ray absorption near edge spectra

XAS: X-ray absorption spectroscopy

XRD: X-ray diffraction

ΔG: Gibbs free energy of the reaction

ΔfE : formation energies

Table of contents

CHAPTER 1: General introduction

1.1. Energy storage scenario

The accelerated release of carbon dioxide (CO_2) into the atmosphere from the combustion of fossil fuels and biomass is intensifying the adverse impacts of climate change, particularly global warming (Figure 1). The incessantly increasing energy demand for grid, transport, and portable applications is therefore becoming a major challenge in this century. Thus, there is a pressing need to achieve an environmentally sustainable energy supply, where energy storage will play an essential role.[1]

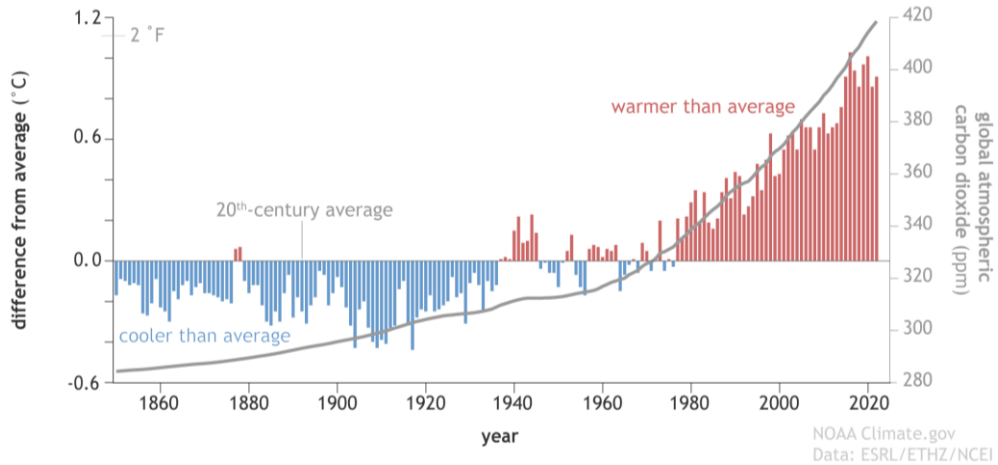

Figure 1: Yearly global surface temperature and atmospheric carbon dioxide (1850-2022)[2].

Since the 1980s, there has been a threefold surge in the consumption of electricity, driven by its usage in residential, commercial, and industrial sectors. Coal is a major source of CO_2 and other harmful pollutants that negatively affect the global ecosystem. The introduction of renewable energy policies, following the establishment of the Kyoto protocol (2005) and the Paris agreement (2016), has boosted the use of these alternatives to coal usage. The efficient storage of electricity produced by renewable energies, through the further integration of energy storage systems

(ESSs) into the power grid, becomes crucial for the successful implementation and amplification of these new sustainable technologies playing a vital role in advancing the decarbonization. These ESSs are also indispensable in remote areas, serving for peak energy demands and emergency operations.

The field of energy storage encompasses five different technologies according to the physical or chemical processes that are used: mechanical, chemical, thermal, electrical, and electrochemical energy storage. Their main applications are described in Table 1.

Technology	Applications
Mechanical	Off-grid, black start, hydroelectric ES
Chemical (Hydrogen)	-Seasonal ES
Thermal	Process optimization and energy efficiency in industry
Electrical	Frequency regulation ESS in the grid
Electrochemical	EVs and portable ES

Table 1: Comparison of the characteristics and applications of the energy storage (ES) technologies.

On the other hand, the growing market of electric vehicles (EVs) is expected to further amplify the demand for electricity. The European Commission has set an ambitious target to reduce greenhouse gas emissions from the transportation sector by more than 60% by 2050, with EVs being the preferred technology for facilitating this transition.[3] It is anticipated that EVs will largely replace conventional gasoline-powered vehicles in the foreseeable future. Moreover, recent legislation passed by the European Union in March 2023 has effectively banned the sale of new vehicles equipped with combustion engines, hybrids, and plug-in hybrids from 2035 onwards.[4]

The rechargeable battery, serving as the essential core component of EVs, necessitates superior performance.[5] The automotive industry seeks batteries with higher energy density and power capabilities to enhance the performance and competitiveness of EVs compared to those with internal combustion engines, allowing for longer driving ranges. Currently, the most promising EVs have a

range limited, in the very best case, to around 775 km,[6] while improving battery safety under demanding operating conditions remains a significant challenge.

Electrochemical energy storage systems offer high energy density, and they are usually oriented to short-medium term storage, i.e., portable energy storage applications and EVs.

1.2. Electrochemical energy storage though rechargeable batteries

Batteries are electrochemical energy storage (EES) systems that convert electrical energy into chemical reactions or vice versa through reduction-oxidation (redox) reactions. Batteries consist of two electrodes (referred to as positive and negative) separated by an electrolyte, and whose potential difference indicates the driving force or electromotive force that enables the flow of electric current within the system. The redox reactions take place exclusively in these electrodes and allow to store or use the energy, while the electrolyte acts as electronic insulator and ionic conductor by facilitating controlled ion movement and preventing short circuits.

There are two types of batteries depending on their reversibility. On the one hand, **primary batteries** in which the redox reaction that occurs between electrodes is irreversible. They present lower power and higher capacity than secondary batteries, making them useful for applications such as watches, pregnancy tests, vehicle keys, etc. On the other hand, **secondary batteries** in which the redox reactions are reversible, allow continuous charge and discharge of the system increasing their cycle life. Among these rechargeable batteries, there are five main commercial technologies: Lead acid, Nickel-cadmium (Ni-Cd), Nickel-metal hydride (Ni-MH), redox flow batteries and lithium-ion batteries (Li-ion).

The performance evaluation of electrochemical power sources is done based on several magnitudes. In the following paragraphs the main magnitudes and concepts are described.

Cell potential or cell voltage

The cell voltage, U, is the measure of the potential difference between two electrodes in an electrochemical cell and it is a crucial magnitude in battery performance. The Gibbs free energy of the reaction, *ΔG*, is the maximum accessible energy from a cell and the cell voltage is derived from the free energy of the chemical reaction as described in the Nerst equation (1). If we ignore entropic effects, the chemical potential can be approximated to the total energy computed by DFT calculations, as it represents the partial molar quantity of the Gibbs free energy.

(1) $$U^0 = \Delta E^0 = E^{0,(+)} - E^{0,(-)} = \frac{-\Delta G^0}{n \cdot F} \quad [V]$$

$E^{0,(+)}$ = positive electrode potential
$E^{0,(-)}$ = negative electrode potential
n= number of transferred electrons
F= Faraday's constant

Current density

The current density, *j,* is the ratio of the total current flowing through an electrode, *I,* to its surface area, *A*.

(2) $$j(t) = \frac{I(t)}{A} \quad [A/m^2]$$

Charge capacity

Charge capacity, *Q*, refers to the overall quantity of electric charge that can be provided by a cell.

(3) $$Q = \int_{t1}^{t2} I(t).dt \quad [Ah]$$

Coulombic efficiency

The coulombic efficiency is commonly employed to characterize the effective battery capacity. In rechargeable batteries, it denotes the proportion between the discharge capacity following a complete charge and the charging capacity within the same cycle.

(4) $$CE = \frac{\text{Discharge capacity}}{\text{Charge capacity}} x\ 100 \quad [\%]$$

It is influenced by factors such as electrolyte breakdown, material aging, environmental temperature, and variations in charge-discharge current rates; all of them impact the battery's discharge effectiveness.[7]

Theoretical specific capacity and volumetric energy density

The theoretical specific capacity, q_{th}, is the amount of charge per kg of reactants, $m_{i,}$ and is given by:

(5) $$q_{th} = \frac{n\ .\ F}{\sum_i m_i} \quad [\text{Ah/kg}]$$

The theoretical volumetric energy density, $Q_{V,th}$ is calculated by dividing the total charge by volume of the reactants, V_i.

(6) $$Q_{V,th} = \frac{n\ .\ F}{\sum_i V_i} \quad [\text{Ah/l}]$$

The charge-discharge rate

The charge-discharge rate, also known as the C-rate and D-rate, is a measure used to describe the number of hours required for a complete charge or discharge of a cell. In this context, C represents the theoretical charge capacity of the cell in ampere-hours (Ah) and D represents the theoretical discharge capacity of the cell in ampere-hours (Ah). Hence, for example, 2C and C/2 stand for a current theoretically allowing a full discharge in 30min and 2h, respectively. It can be expressed as follows:

(9) $$C - rate\ or\ D - rate = \frac{charge\ or\ discharge\ current}{Theoretical\ capacity}$$

Discharging the cell at higher currents usually results in a decrease in the achievable final capacity due to kinetic limitations stemming from both the battery's internal resistance and the resistance at the electrode-electrolyte junction. These constraints impede the internal mechanisms responsible for the movement of charged particles,

subsequently leading to voltage drops, a phenomenon known as polarization.

Rate capability

The rate capability is the discharge or charge capacity of a material or cell at different currents. In this thesis, the term rate capability will be used to describe the capacity of the electrochemical cell during cycling at various C-rates and D-rates.

Theoretical specific power and power density

Specific power *p,* and power density, $P_{V,}$ are normally used to describe the rate capability of cells. They represent the amount of power delivered per unit mass or unit volume of a cell respectively.

(7) $$p = \frac{I \cdot \Delta E^0}{\sum_i m_i} = q_{th} . \Delta E^0$$ [W/kg]

(8) $$P_V = \frac{I \cdot \Delta E^0}{\sum_i V_i} = Q_{V,th} . \Delta E^0$$ [W/l]

Self-discharge

Self-discharge refers to the natural process by which a battery loses its stored charge over time, even when it is not being actively used. This phenomenon occurs due to internal chemical reactions within the battery that cause a gradual discharge of energy. It is measured in percentage over time.

Cycle life

Cycle battery life refers to the number of charge and discharge cycles that a rechargeable battery can undergo while maintaining a certain level of capacity and performance. Each complete charge and discharge cycle contributes to the gradual wear and degradation of the battery's chemical composition and physical structure, ultimately leading to a reduction in the battery's overall capacity and efficiency over time. Monitoring and understanding the cycle battery life is crucial for estimating

the usable lifespan of rechargeable batteries in various devices and applications.

The five main technologies of secondary batteries and their characteristics are presented in Table 2.

	Lead acid	**Ni-Cd**	**Ni-MH**	**Redox flow**	**M-ion**
Negative electrode	Pb	Cd	Intermetallic alloys	Porous electrode with anolyte (V-based)	Carbon-based
Positive electrode	PbO_2	$Ni(OH)_2$	$Ni(OH)_2$	Porous electrode with catholyte (V-based)	Li/Na-based transition metal compounds
Electrolyte	H_2SO_4	Aqueous solution (KOH)	Aqueous solution (KOH)	-	Organic solvent
Energy density ($WhKg^{-1}$)	30-40	40-70	60-120	10-20	270
Coulombic efficiency (%)	50-92	70-90	66	80	90+
Self-discharge (% $month^{-1}$)	3-20	10	30	5	<1
Cycle life	500	1000	1500	15000	4000
Application example	Vehicle start engine	Electronic devices	Electronic devices and EVs	Grid ES	Portable electronics and EVs

Table 2: Comparison of the intrinsic characteristics of the five main secondary battery technologies.[8–13]

In the realm of available technologies, Li-based batteries have emerged as a leading contender due to their exceptional energy

density and versatile design characteristics (Table 2). Consequently, they have become the focal point of considerable interest and scrutiny at both fundamental and applied levels.[14] Lithium-ion batteries are relevant for all types of applications, whether they are portable, mobility-related, and now that their price is more competitive, also for grid applications.

1.3. Lithium-ion reversible batteries

Lithium-ion batteries (LIBs) have been commercialized by Sony since the early 1990s[15]. Compared with other commonly rechargeable batteries like Ni-Cd, Ni-MH and Lead-acid batteries, LIBs are featured by high energy and power density, long service life and environmental friendliness.[16] This technology is centered around the use of lithium-intercalation compounds, which have a crystalline structure that allows the insertion or intercalation of lithium ions. During charge, the lithium ions (Li^+) move from the cathode to the anode through the electrolyte, and conversely in the case of discharge. The insertion/deinsertion of lithium into the electrodes allows the redox reactions occurring in the host materials to balance the charges as shown in Figure 2.

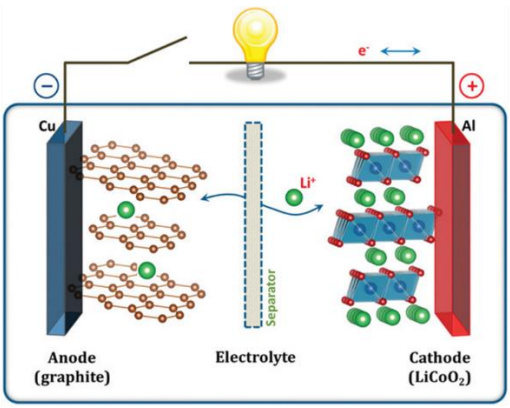

Cathode reaction: $LiCoO_2 \rightarrow Li_{1-x}CoO_2 + xLi + xe^-$

Anode reaction: $6C + xLi^+ + xe^- \rightarrow Li_xC_6$

Overall battery reaction: $LiCoO_2 + 6C \rightarrow Li_{1-x}CoO_2 + Li_xC_6$

Figure 2: Schematic diagram of Li-ion batteries behavior using as example a graphite anode and a $LiCoO_2$ cathode. The reactions involved in the process are described below. Reproduced from Goodenough et al. 2013.[17]

In LIBs, graphite-based materials are commonly used as negative electrodes (referred as to **anodes**) due to the cost-effectiveness and widespread availability of carbon. Additionally, graphite is a popular choice due to its stability in accommodating lithium insertion.[16] However, the lithium insertion capacity of graphite, 372 $mAhg^{-1}$, is one order of magnitude lower than that of Li metal electrodes, 3862 $mAh \cdot g^{-1}$, making it an area of interest for further improvement.[18] Lithium metal electrodes are considered key in batteries beyond the current LIB technology due to their high energy density, although they still face several stability challenges due to the formation of dendrites that compromise the intrinsic safety of the battery. In recent years, significant efforts have been dedicated to optimizing negative electrode materials. This has led to the development of several new materials, including silicon, alloys, and metal oxides.[19] However, these new materials are still far below the Li metal energy density, 3862 $mAh \cdot g^{-1}$ (not shown in Figure 3 because its capacity falls out of scale), being Si-C based anodes those with the highest capacity, around 1200 $mAh \cdot g^{-1}$ (see Figure 3).

Electrolytes utilized in LIBs can be categorized into two groups: liquid electrolytes and semisolid/solid-state electrolytes. **Liquid electrolytes** typically consist of lithium salts, including $LiBF_4$, $LiPF_6$, $LiN(CF_3SO_2)_2$ LiTFSI, and $LiB(C_2O_4)_2$ LiBOB, which are dissolved in organic carbonates like ethylene carbonate (EC), propylene carbonate (PC), ethyl methyl carbonate (EMC), dimethyl carbonate (DMC), and their mixtures.[20]

The development of solid electrolytes currently holds significant importance, mainly driven by concerns regarding the flammability of conventional liquid electrolytes and, also, because they are more suitable for the use of Li-metal anodes as they prevent dendrite growth. **Solid-state polymer electrolytes (SSPE)** are typically composed of lithium salts as conducting salts, along with high-molecular-weight polymer matrices such as polyvinylidene fluoride (PVDF), poly(ethylene oxide) (PEO), and polyvinylidene fluoride-hexafluoropropylene (PVDF-HFP).[21,22] A common way to increase the conductivity of the polymer is the addition of a plasticizer to form **gels or semi-solid electrolytes.** PC, EC and poly(dimethoxy ethylene glycols) (PEGDME) are the most commonly used

plasticizing agents.[23] On the other hand, oxide and sulfide families are the most studied **solid state ceramic electrolytes (SSCE)**. Among oxide ceramic electrolytes $Li_7La_3Zr_2O_{12}$ (LLZO) and $Li_{1+x}Al_xTi_{2-x}(PO_4)_3$ (LATP) are the most common.[24,25] Sulfides capture attention because they are easier to mechanically process but they react with moisture to release hydrogen sulfide (H_2S) that can be lethal in a certain threshold.[26]

Solid-state polymer electrolytes present clear advantages over both liquid and solid state ceramic electrolytes, offering enhanced safety, flexibility, density, and design versatility. However, solid state ceramic electrolytes can be coupled with cathodes operating at higher voltages. Both solid state polymer and ceramic electrolytes have the potential to suppress or prevent dendrite growth under specific conditions.

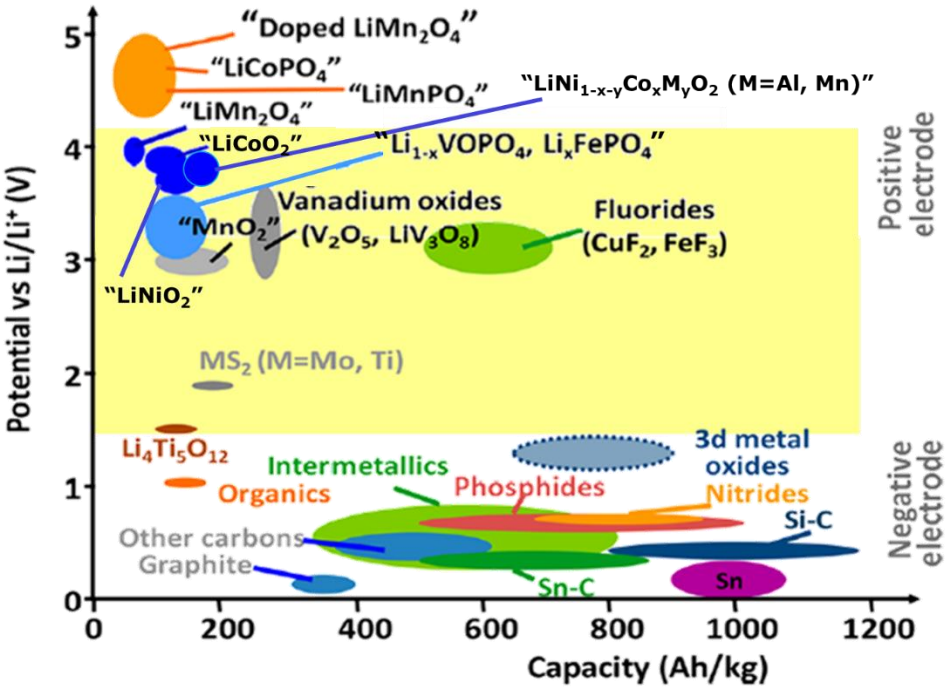

Figure 3: Relationship between voltage and capacity depicted for both positive and negative electrode materials currently in use or being seriously considered for the next generation of rechargeable Li-based cells. The yellow area corresponds to moderate operation potentials within the electrolyte stability window. Adapted from Palacin et al. 2021.[27]

To create efficient and affordable batteries, positive electrode materials (referred as to cathodes) with good ionic conductivity are needed to achieve high reversibility. Another concern is their price and availability, together with its thermal stability. **Cathodes** consist of complex lithiated compounds including, among the most studied materials, the commercial layered oxides $LiCoO_2$ (LCO), $LiNi_{1-x-y}Co_xAl_yO_2$ (NCA), and $LiNi_{1-x-y}Co_xMn_yO_2$ (NMC); spinel $LiMn_2O_4$ (LMO) and its variations $LiM'_{0.5}Mn_{1.5}O_4$ (LMM'O, M'=Ni, Fe, Co); and triphylite $LiMPO_4$ (LMP, M=Fe, Mn). The energy density of cathode materials can be improved either by increasing the voltage by means of metal substitutions (i.e., Fe for Mn in triphylite or Mn for Ni in spinels) or by increasing the capacity, a strategy typically followed for example when increasing the Ni content of layered oxides. The crystal structures of these three families are shown in Figure 4. In the following sections, they will be discussed in more detail to conclude, in Section 1.4.3., with an extended discussion on the $LiFe_{0.5}Mn_{1.5}O_4$ (LFMO) spinel that has been selected as principal material of study in this thesis.

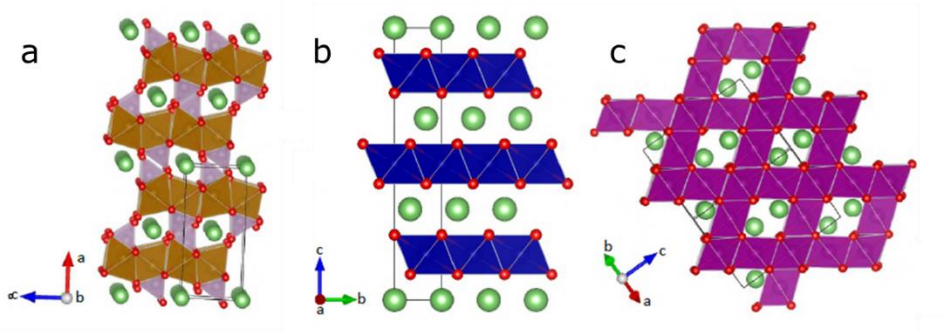

Figure 4: Crystal structures of a) triphylite, b) layered oxide and c) spinel. Green spheres represent lithium, red spheres oxygen, gray tetrahedra PO_4 and brown, blue and purple octahedra MO_6.[28–30]

1.4. Main families of positive electrode materials

1.4.1. Polyanionic phospho-olivine triphylite

The polyanionic phospho-olivine triphylite, $LiFePO_4$ (LFP), whose structure is depicted in Figure 6-a, was first tested as cathode material by Padhi *et al.* in 1997[31]. It has become the most

extensively studied compound within this family and is commercially available, also with Mn partial substitution to enhance the operation voltage (LFMP). Triphylites crystallize in the orthorhombic *Pnma* space group. The structure comprises corner-shared FeO_6 (MnO_6) octahedra, and LiO_6 octahedra sharing edges parallel to the b-axis and interconnected by PO_4 tetrahedra. In the fully lithiated phase, Fe^{2+} (Mn^{2+}) oxidizes to Fe^{3+} (Mn^{3+}) upon complete lithium extraction.[32,33] Its three-dimensional structure allows high reversibility, exceptional thermal stability, and performance, even at high rates. Additionally, this material is cost-effective and exhibits low toxicity. LFP has a theoretical capacity of 170 mAh/g at 3.4 V *vs*. Li/Li^+,[34,35] resulting in limited energy density. It has however low electronic conductivity (10^{-9} $S.cm^{-1}$ at room temperature), which requires carbon coating and/or nanosizing to enhance electron transport.[36]

Various types of insertion materials have been reported by combining polyanionic units with other elements possessing high electronegativity. An especially attractive classification of cathodes consists of alkali metal fluorophosphates that display increased redox potentials attributed to the intrinsic electronegative nature of fluorine. Expanding on this concept, Barker *et al.* were pioneers in reporting $LiVPO_4F$ as a cathode with an operational potential of 4.1 V *vs.* Li/Li^+ in 2003.[37] This breakthrough initiated a surge of investigations into a multitude of fluorophosphate cathodes such as Li_2CoPO_4F, $LiTiPO_4F$ and Li_2FePO_4F.[38]

1.4.2. Transition metal layered oxides

Transition metal layered oxides have been extensively studied as cathode materials for LIBs since 1980 when Mizushima *et al.* first proposed $LiCoO_2$ (LCO) as cathode material.[39] LCO demonstrated outstanding performance, leading to the commercialization of the first Li-ion battery by Sony. It crystallizes in trigonal *R*-3*m* space group with CoO_6 and LiO_6 octahedra alternating in layers as can be seen in Figure 4-b in a closed packed array. During charge, Co^{3+} oxidizes to Co^{4+}. However, when highly delithiated, the material undergoes irreversible structural changes and becomes chemically unstable posing safety risks. For this reason, in practice, its practical

capacity is limited by this irreversibility reaching only ~150 mAh g^{-1}, slightly above half of its theoretical capacity.[40] $LiNiO_2$ (LNO) was explored as an alternative but faced challenges due to the similar cation size between Li^+ and Ni^{2+}, resulting in lithium-deficient phases ($Li_{1-x}Ni_{1+x}O_2$) where Ni^{2+} cations occupy the lithium layer, hindering ion diffusion.[41] Incorporating cobalt and aluminum doping addressed these issues, leading to the commonly used composition $LiNi_{0.80}Co_{0.15}Al_{0.05}O_2$ (**NCA**). This modification enhances thermal stability and prolongs the battery's lifespan due to stronger bonding between aluminum and oxygen (Al-O) delivering a relatively high capacity of > 180 mAh.g^{-1} at 3.7V *vs*. Li/Li^+ and is now used commercially in vehicle battery applications.[42–44] Manganese has also been studied as an affordable alternative, but direct synthesis of $LiMnO_2$ is difficult due to the Jahn-Teller effect of Mn^{3+}. The synthesis including Ni leads to structural defects while this is restricted in presence of cobalt, enabling $LiNi_{1/3}Mn_{1/3}Co_{1/3}O_2$ (333**NMC**)[45]. Different formulations like $LiNi_{0.5}Mn_{0.3}Co_{0.2}O_2$ (532NMC)[46] and $LiNi_{0.6}Mn_{0.2}Co_{0.2}O_2$ (622NMC)[47,48], with higher nickel content have been explored, but still thermal stability becomes a concern. Nowadays, $LiNi_{0.8}Mn_{0.1}Co_{0.1}O_2$ (811NMC) has garnered significant interest due to its benefits compared to cathodes with lower nickel content having a capability of ≈200 mAhg^{-1} and an average voltage of 3.8V *vs.* Li/Li^+.[49–51] Core-shell structures with a nickel-rich core and manganese-rich shell offer a solution by combining high capacity with thermal stability. Concerns regarding the use of cobalt, due to the scarcity of cobalt resources and high price fluctuations, have renewed interest in cobalt-free compositions, such as Ni-rich[52] and Mn-rich layered oxides.[53]

Another popular strategy to increase the capacity of layered oxides are Li-rich compositions (i.e., $Li_{1+x}M_{1-x}O_2$ materials that accommodate extra lithium atoms in the TM positions of layered oxides). Analyzing the band structure of these compounds has revealed that one of the oxygen's $2p$ orbitals exhibits weak bonding characteristics, behaving in a manner similar to a non-bonding orbital. This is attributed to its minimal overlap with the $2s$ orbital of lithium (Figure 5-A). As a result, along with the formation of the anti-bonding $(M-O)^*$ band resulting from the metal-oxygen bonds,

the presence of this extra non-bonding orbital (also called as $Li{-}O{-}Li$) facilitates the extraction of additional electrons when cations undergo oxidation. This leads to an enhanced capacity without compromising the structural stability of the electrode material. By altering the characteristics of transition metals ($3d$, $4d$, $5d$) and consequently modifying the relative positioning of the $(M{-}O)^*$ and $Li{-}O{-}Li$ bands, it becomes feasible to manage and regulate the redox reactions of both cations and anions. According to this, the band structure can be classified in three cases, as can be seen in Figure 5-B-D: the typical cationic redox process (B) occurs when O and metal bands do not overlap, reversible anionic redox (C) occurs when electron removal results in a two-band redox process giving extra capacity, and irreversible anionic redox (D) occurs when electron removal results in a one-band redox leading to O_2 gas release upon electron removal. The Li-rich research is focused in achieving reversible anionic redox processes within these family as oxygen redox processes contribute to the total capacity of the material.[54]

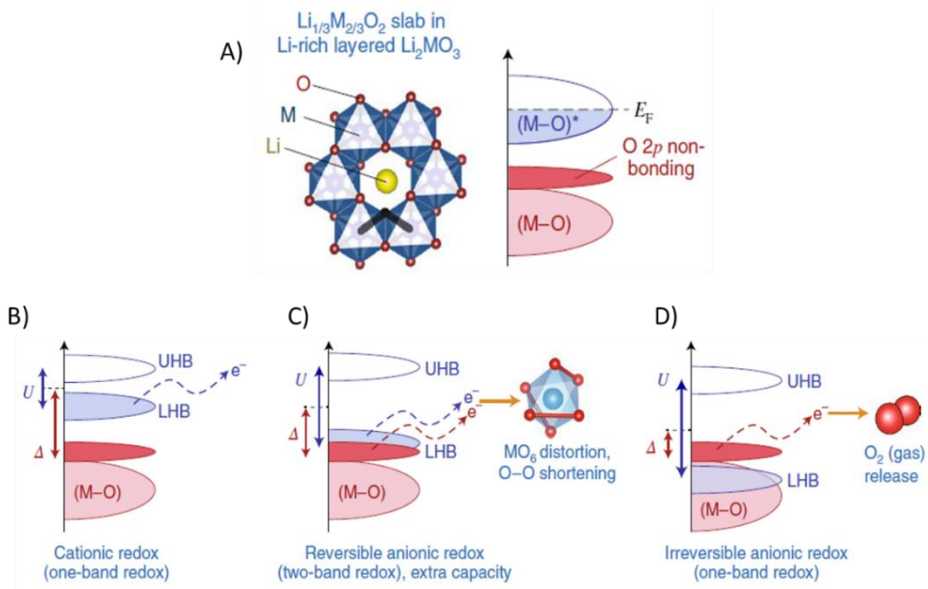

Figure 5: Li-rich layered oxide crystallographic and band structures (A) and the classification of its band structure in three scenarios: B) Cationic redox, C) Reversible anionic redox, and D) Irreversible anionic redox. UHB and LHB denote the upper and lower Hubbard bands respectively. Reproduced from Assat et al. 2018.[54]

1.4.3. High voltage Manganese-based spinel oxides

Spinel-type materials, typically with the formula AB_2O_4 (where A and B represent metal ions), are popular for their capacity to host a variety of metals. This kind of materials have been used in many fields such as semiconductors[55,56], catalysis[57] and conductive films[58,59] and have demonstrated to be effective cathode materials. $LiMn_2O_4$ was first proposed by Thackeray *et al.* in the early 80's[60,61]. In Figure 4-c the LMO structure is depicted. It adopts the cubic *Fd-3m* space group, where manganese forms octahedral units (MnO_6) that share corners with lithium tetrahedra (LiO_4) and edges with additional manganese octahedra (MnO_6).[62] LMO provides good ionic and electrical properties, high electronic conductivity, low cost, high theoretical capacity (148 $mAhg^{-1}$), and environmental friendliness when compared to other materials.[63,64] Furthermore, Mn spinels are characterized by their high voltage (~4.0 *vs.* Li/Li^+ in LMO for the redox couple used commercially, $Mn^{3+/4+}$) in comparison with layered oxides and polyanionic compounds and by their noteworthy intrinsic 3D lithium conductivity.

In 1996, NEC became the first company to commercialise $LiMn_2O_4$ as a LIB cathode material in small portable devices, marking a significant milestone in the development of this technology. Since then, it was used in some rechargeable LIBs for electric vehicles, and currently, LMO is used in blends to enhance the power capability of layered oxides such as nickel cobalt aluminium (NCA) and nickel manganese cobalt (NMC)[65]. These blends allow for optimized performance by combining different lithium metal oxides, achieving a balance of characteristics necessary for specific battery applications[66–68].

In LMO, manganese exhibits an average oxidation state of +3.5 and can both accommodate and donate lithium ions. When the material is charged, lithium ions abandon the structure and all the manganese oxidizes to Mn^{4+}, resulting in the formation of Mn_2O_4. Conversely, during discharge, extra lithium ions are inserted into the structure, forming the $Li_2Mn_2O_4$ phase where all manganese ions are in the Mn^{3+} state.[61] However, LMO has a major drawback that

originates from the fact that Mn^{3+} is a Jahn Teller (JT) active ion, which causes large distortions in the crystal structure of the material during the charging and discharging, leading to poor capacity retention over prolonged cycling. An average oxidation state of manganese lower than +3.5 induces JT effect, thus, the extra lithium insertion when passing from $LiMn_2O_4$ to $Li_2Mn_2O_4$ has been observed to lead to rapid capacity degradation due to the structural deterioration. Additionally, Mn^{3+} disproportionates into Mn^{2+} and Mn^{4+}, and Mn^{2+} is irreversibly dissolved in the electrolyte in presence of acidic species and associated factors such as pH changes and side reactions. This results in loss of active material, impedance rise, and Mn^{2+} migration-deposition on the anode, significantly impacting its long-term performance. Consequently, the redox activity of this spinel is practically limited to the $Mn_2O_4/LiMn_2O_4$ reaction, which restricts its energy density. These effects can be minimized by making partial substitution of Mn in the LMO by other transition metal divalent and trivalent ions, such as Co^{2+}, Ni^{2+}, $Fe^{3+/2+}$, Mg^{2+}, Cr^{2+}, Zn^{2+}, Cu^{2+}, Al^{3+}, or Sc^{3+} [69–72]. These substitutions have been shown to improve the cycling stability within the 4 V region, and in certain cases provide additional electrochemical activity at higher potentials *vs.* Li^+/Li.

In this context, $LiM_{0.5}Mn_{1.5}O_4$ (M = Fe, Co, Ni)[73] compositions have attracted substantial research attention because they allow for significantly increasing the average voltage. Table 3 summarizes the most relevant parameters related to these metal substitutions in relation to LMO and the voltage-capacity curve of these materials is shown in Figure 6. The most relevant characteristics of these metal substitutions will be further discussed next.

Spinel	Theoretical capacity ($mAh \cdot g^{-1}$)	Discharge operating voltage vs. Li/Li^+ (V)	Transition metallic ordering	Sustainability	Metal cost
$LiMn_2O_4$	148	4.0 and 4.1	No	High	Low
$LiCo_{0.5}Mn_{1.5}O_4$	147	4.0 and 5.1	No	Very low	Very high
$LiNi_{0.5}Mn_{1.5}O_4$	147	4.70 and 4.75	Yes, depending on the synthetic conditions	Low	High
$LiFe_{0.5}Mn_{1.5}O_4$	148	4.0 and 5.0	No, according to this work	High	Low

Table 3: Comparison of relevant parameters among LMO, LCMO, LNMO and LFMO spinels[30,54,74–81].

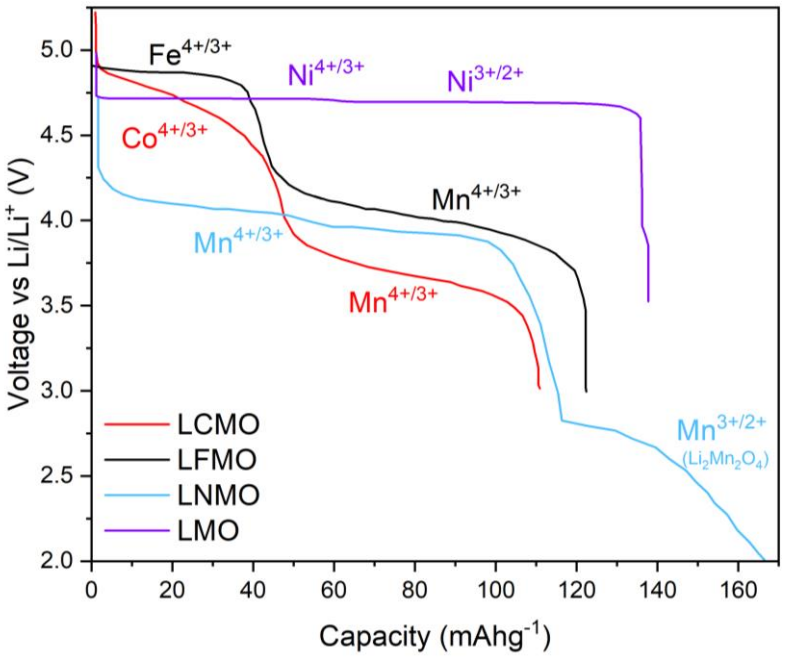

Figure 6: Experimental curves for LMO, LCMO, LNMO and LFMO adapted from refs.[74,78,82,83]

$LiCo_{0.5}Mn_{1.5}O_4$ (LCMO)

LCMO has been studied from a theoretical point of view revealing that it can operate in the 5V regime within the $LiCo_xMn_{2-x}O_4$ (x= 0, 1, 1.5, 2) composition, much higher than other studied materials. It was predicted to operate at voltages between 3.95V, for x=0, and 4.47V *vs.* Li/Li^+, for x=1.[84] Experimentally it has been observed that it operates at voltages up to 5.1 V *vs.* Li^+/Li, where the $Co^{3+/4+}$ redox couple plateau is observed,[75] and no cation ordering has been shown between transition metals in the structure.[80] However, as it can be seen in Figure 6, LCMO does not reach the theoretical capacity. In addition, the high toxicity and cost of cobalt, as well as the geopolitical and ethical issues associated with its extraction, render Ni and Fe substitutions more appealing.

$LiNi_{0.5}Mn_{1.5}O_4$ (LNMO)

LNMO spinel has been intensively investigated since the 2000's[85,86] due to its ability to operate at higher voltage than LMO while keeping its theoretical capacity of 147 $mAhg^{-1}$. LNMO presents an extended two-step plateau centered at around 4.7 V *vs.* Li^+/Li, which is attributed to Ni^{2+} oxidation to Ni^{3+} and Ni^{4+}, with both processes separated by ~0.05 V, as depicted in Figure 6. Both experimental and theoretical studies have shown that the voltage and composition curves of LNMO are altered depending on the distribution of Ni^{2+} and Mn^{4+} ions within the crystal structure[76,81,87]. Indeed, LNMO undergoes a reversible order-disorder transition from a disordered (*Fd*-3*m*) structure into a transition-metal ordered one (space group $P4_332$) around 700ºC. From a theoretical perspective, different Ni/Mn distributions have been considered to compute the corresponding voltage curves using density functional theory (DFT) calculations and proving that disordered distributions are energetically more favorable than the ordered one.[88] Furthermore, for $Li_xNi_{0.5}Mn_{1.5}O_4$, the ordered distribution shows no stable arrangements of Li ions and Li vacancies (V_{Li}) over $0 < x < 1$, while the disordered phases exhibit several stable intermediate Li/V_{Li} configurations for $x \geq 0.5$[88]. However, the use of nickel has significant drawbacks, including toxicity, environmental impacts of its extraction, high and volatile market prices, and limited

availability. To address these challenges, manage cost instability, and assure long-term sustainability, it is necessary to investigate alternative materials and technologies.

$LiFe_{0.5}Mn_{1.5}O_4$ (LFMO)

$LiFe_{0.5}Mn_{1.5}O_4$ (LFMO) spinel has deserved much less attention than LNMO although it offers advantages in terms of cost and sustainability.[78,89,90]

Interestingly, in contrast to LNMO, no transition-metal ordering has been reported so far for LFMO, and thus the cubic structure of LFMO is described with the usual spinel *Fd*-3*m* structural model that corresponds to Figure 4-c, in which Mn and Fe occupy the octahedral sites and Li the tetrahedral sites in the structure.[74] However, antisite defects, in which Fe partially occupies the tetrahedral sites, are sometimes reported.[75,75,86,91,92] Li *et al.* studied the magnetic properties of LFMO concluding that it presents an antiferromagnetic ordering below a Neel temperature (T_N) of 34K.[91,93]

Aiming at improving cyclability and higher capacities, as well as, to understand better its structure, this material has been studied experimentally considering different synthetic methods such as sol-gel[73,74,89,92,94], solid-state[75,78,86,91,95,96], standard ceramic, auto-ignition[90], solvothermal, impregnation and template-hydrothermal methods[94]. Actually, Pico *et al.* was able to control the morphology of LFMO by using different synthetic methods.[94]

LFMO operates at high voltages presenting two distinct pseudo-plateaus, one in the 4 V region *vs.* Li^+/Li corresponding to the $Mn^{3+/4+}$ redox reaction and a second one in the 5 V region *vs.* Li^+/Li corresponding to the $Fe^{3+/4+}$ redox couple, as shown in Figure 6. Shigemura *et al.* studied the valence state of LFMO during cycling by in situ Mössbauer spectroscopy and x-ray absorption spectroscopy measurements corroborating these changes in the oxidation states but observing just a partial redox activity of Fe.[75,95] The theoretical capacity is indeed not reached, and the highest capacity obtained until now is $125mAhg^{-1}$ at $0.1mAcm^{-1}$ with a high capacity fading,[78] opening the path to further investigations to increase its capacity.

As described in Section 1.3, the electrolyte can suffer from degradation processes at high voltage. FMO has successfully been coupled with certain solid and liquid electrolytes ($Li_7La_3Zr_2O_{12}$[97], 1M $LiBF_4$ in in EC and DMC[78]), with enhanced stability at high voltage. However, additional investigation is needed in this field to enable long cycling at high voltage without electrolyte/cell degradation. Further research is thus still needed to improve the knowledge and properties of these kind of materials to address the urgent demand of new battery materials with superior performance in terms of energy density, lifespan, and safety. In this regard, the conventional trial-and-error traditional approach in materials discovery is time-consuming and expensive and new approaches and better tools to accelerate the discovery and understanding of new battery materials are necessary.

1.5. High-Throughput and automation needs

Computational materials screening and high-throughput experimental approaches, combined with artificial intelligence (AI) within so-called Materials Acceleration Platforms (MAPs), are expected to drastically accelerate the pace of discovery and development of new battery materials in the next few years.[63,98–100]

Theoretical approaches to identify new advanced materials are an appealing and promising option since they require fewer resources in terms of time, labor, materials, and infrastructure than traditional experimental approaches. One strategy recently explored consists in the systematic screening of materials databases to identify structures possessing desirable properties for high-performance battery materials. For example, one such crucial property is the existence of favorable migration pathways for alkali cations.[101] Yet, the high-throughput screening of thousands of entries is costly and time consuming, and, therefore, fast and efficient evaluation methods are required. In this regard, procrystal electron density analyses[102–104] and Bond-Valence Site Energy calculations[101,105–108] have shown to be good approximations for evaluating migration pathway and migration energies. The Materials Genome Initiative

(MGI)[109] was launched in the United States in 2011 and aims to expedite the discovery and deployment of new advanced materials with tailored properties across various applications, including energy, electronics, and healthcare, amongst others. This initiative employs an approach that combines computational modeling, and data-driven methodologies[110,111]. By leveraging these multidisciplinary tools, MGI strives to overcome the limitations of traditional methods and expedite the development of new battery materials.

After a first theoretical screening, the next crucial step involves experimental validation to assess the suitability of the selected candidate materials. Although theoretical screening is timesaving initially, it often generates a significant number of appealing candidate materials. Consequently, conducting thorough experimental validation becomes a laborious and resource-intensive undertaking. As a result, this experimental stage remains a bottleneck in the development of new battery materials, necessitating acceleration (Figure 7). In 2021, the first goal of the strategic plan of MGI passed to be the unification of Materials Innovation Infrastructures (MII) including experimental (synthesis, characterization, and processing) tools.[109]

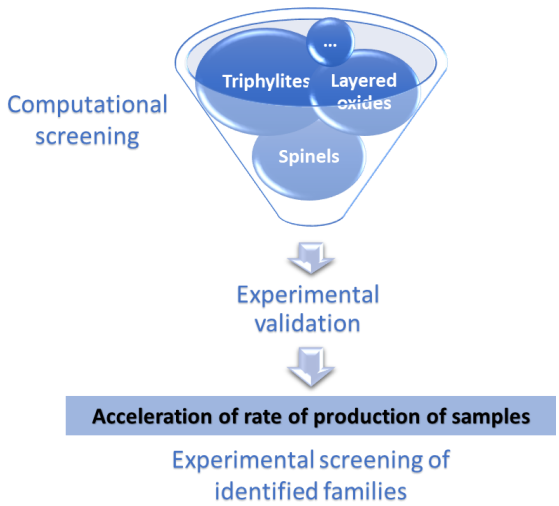

Figure 7: Scheme of the experimental bottleneck generated by the computational identification of materials indicating the need of accelarating the experimental validation step.

A crucial aspect of the MAPs is the implementation of efficient and effective automated high-throughput experiments, which should enable the rapid synthesis, testing, and screening of large libraries of materials. In the 1960s, pioneers Merrifeld and Stewart revolutionized the field of automated organic compound synthesis by developing the first automated system for synthesizing peptides. This groundbreaking development significantly reduced the time and materials required for each addition and purification steps.[112] Today, high-throughput synthesis (HTS) is a standard practice in fields such as pharmaceutical research.[113,114]

However, when it comes to electrochemical devices and systems, inorganic compounds are often preferred as electrode materials[115] due to their exceptional combination of electrical conductivity, stability, durability, and specific electrochemical properties, as it has been highlighted in Section 1.4 in the specific case of LIBs. Unfortunately, the development of HTS methods for inorganic compounds lags significantly behind that of organic compounds. This discrepancy arises from the fact that organic reactions often occur under mild conditions and are compatible with a broader range of solvents and reaction conditions, making them more amenable to automation and HTS. This flexibility facilitates the development of automated systems that can handle multiple reaction types efficiently while inorganic synthesis may require more rigorous control over parameters such as temperature, pressure, and atmosphere. Moreover, the reactants are often to be handled, mixed, and reacted in powder form, making automation more challenging. And, organic synthesis paths can be partitioned in a sequence of consecutive individual steps, whose reactions generally consist in modifying functional groups of hydrocarbon skeletons that are in general well understood and follow well-established reaction conditions and protocols (rationalized using, for example, concepts such as nucleophilic and electrophilic reactions as well as steric effects). Conversely, inorganic syntheses encompass a wide range of elements from the periodic table and are typically carried out through single or limited-step large-scale reactions. These inorganic reactions may involve more intricate reaction mechanisms than in organic synthesis due to the nature of

inorganic compounds and their diversity in terms of structures, geometries, and properties. Often, inorganic reaction mechanisms involve electrostatic interactions, changes in the coordination of metal atoms, electron transfer, and bond activation processes.[116,117]

Only a limited number of research groups have proposed automated tools to perform combinatorial or high-throughput inorganic syntheses of functional materials, specially focusing on oxides with different combination of metals such as Li-Mn-Ni,[118–120] Li-Ni-Co,[121] Li-Ni-Mn-Co,[122] Li−Al−Mn,[120] and Na-Fe-Mn,[123] as well as perovskites like Li–La–Ti–O[124] and metal halides.[125] These initiatives have enabled the efficient screening of new materials for various applications, including batteries, photovoltaic devices, and optoelectronics proposing different synthetic approaches such as sol-gel, solid state, electrostatic atomization, and other high-throughput strategies to increase the sample throughput. Methods such as the utilization of Cartesian Pixsys solution processing robots, and liquid handling robots like the Opentrons OT-2 robot have been employed, some examples of these robotic solutions are displayed in Figure 8. These strategies enable the simultaneous processing of a large number of samples and facilitate the screening of a wide range of compositions within a short timeframe. However, it is worth noting that despite these advantages, the resulting sample quantities typically range from 2 to 30 mg. This amount is frequently insufficient for comprehensive characterizations or further studies on the same batch, and it is imperative to develop methodologies that can generate larger sample sizes, facilitating more comprehensive analyses and investigations.

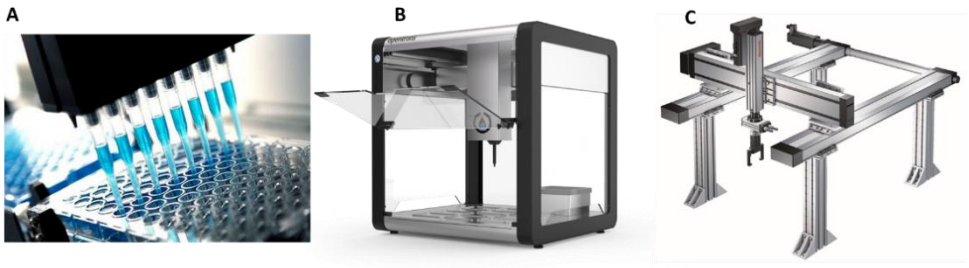

Figure 8: Examples of robotic solutions utilized in HT inorganic synthesis. A and B are examples of solution dispensing modules and C is an example of Cartesian processing robot.

The growing trend towards adopting a more comprehensive and globally integrated approach that incorporates AI to expedite experimental exploration has launched different initiatives in accelerating materials discovery including BIG-MAP in the European Union,[126] the Accelerated Consortium at the University of Toronto,[127] and the DIADEM project led by CNRS.[128] These initiatives have garnered significant interest from both the academic and industrial sectors. Within this context, HT synthetic approaches represent a unique opportunity to accelerate the rational development of improved electrode materials.

1.6. Scope and objectives of this thesis

Considering the aforementioned imperative to automatize the synthesis of inorganic materials and the increasing market demand for sustainable cathode material with increased voltage and capacity, it becomes crucial to address this need.

The aim of the present thesis is thus the development of a HT methodology to accelerate the study of the promising family of spinel compounds through the use of autonomous modules and computational tools. More specifically, the LFMO spinel has been selected for a deep structural study from both theoretical and experimental points of view to elucidate the impact of the metal ordering and structural defects on its electrochemical performance. This spinel material has been selected for their study due to its operation at high voltages, as well as for its environmentally friendliness and low cost.

In **chapter 2**, an automated module for the high-throughput synthesis of laboratory-scale samples (200-500mg) of inorganic materials is presented. This module is designed to automatically handle and mix solutions of precursors in appropriate stoichiometries, and to perform a wide range of synthesis routes such as solid-state, sol-gel, Pechini, and other hydro/solvothermal methods while prioritizing structural control and scalable approaches. Its suitability for battery materials is shown with two case studies: (i) sol-gel synthesis of the high-voltage spinels $LiFe_{0.5}Mn_{1.5}O_4$ (LFMO) and (ii) combinatorial sol-gel synthesis on the Li-Mn-Ni oxide system.

In **chapter 3**, a theoretical DFT-based study of LFMO's electrochemical behavior has been performed to better understand the impact of Fe/Mn disorder in the electrochemical performance to further elucidate the intrinsic mechanisms of this material. The $Li_xFe_{0.5}Mn_{1.5}O_4$ composition was selected to evaluate the electrochemical properties of various metal distributions, including the voltage composition curve, phase stability upon delithiation, and the redox activity of the elements using the Perdew-Burke-Ernzerhof (PBE) functional plus the empirical Hubbard U correction (PBE+U), and strongly constrained and appropriately normed (SCAN) functional.

In **chapter 4**, the automated module described in chapter 2 is used to perform a high-throughput screening of the synthetic parameters on the more than 150 synthesized LFMO spinel samples. The impact of these parameters in the LFMO structure, and more particularly, in the crystallization of antisite defects, and the impact of these defects on the electrochemical properties are thoroughly studied.

In **chapter 5**, a general discussion is followed by a summary of the thesis conclusions and an examination of the future perspectives.

In **chapter 6,** the theoretical and experimental methodologies followed during the present work are described.

CHAPTER 2: Development of an automated module for solid-state syntheses of inorganic compounds

2.1. Abstract

This chapter introduces the creation of an automated module referred to as Batteryino-I. This module has been designed for the laboratory-scale high-throughput synthesis of inorganic materials, enabling the exploration of both known and new battery materials while facilitating microstructure control and further scalability. Batteryino-I significantly minimizes manual handling, offers enhanced versatility, and allows for easy upgrades. The capabilities and performance of this module are demonstrated through two selected case studies: the sol-gel synthesis of $LiFe_{0.5}Mn_{1.5}O_4$ (LFMO) and the Li-Ni-Mn oxide system. The results demonstrate the significance of this module and its role as a crucial advancement towards the development of a self-driving MAP for inorganic materials.

2.2. Description of the module

Transitioning from conventional manual synthesis to automated synthesis requires furnishing the chemical laboratory with robotic equipment to accelerate sample production rates. Despite the availability of commercial solutions to automate laboratory procedures that can save researchers time and offer other benefits like being ready-to-use, technical support, warranty and maintenance, these solutions also come with drawbacks. They tend to be expensive, are designed for specific tasks, lack flexibility for modifications or upgrades, and involve reliance on the manufacturer to get supplies or replacements. Furthermore, commercial solutions are limited to produce very small or high amounts of final product

as they are designed for pharmaceutical research or industrial purposes, respectively. However, in some fields of material research, the production of quantities ranging from hundreds of milligrams to a few grams is often necessary. In such cases, opting for in-house hardware development offers advantages over purchasing commercial solutions. For example, it requires a significantly lower financial investment while providing the opportunity to tailor the equipment to meet the specific needs of the researcher. This customization allows for enhanced versatility and the ability to implement self-upgrades as needed.

Building in-house equipment comes however with its own set of challenges.[129] Firstly, it requires the development of both hardware and software, which demands time and expertise from the researchers involved. Secondly, ensuring the reliability and accuracy of the equipment requires addressing various issues such as determining valid calibration intervals, guaranteeing the inertness of system components to reactants, and verifying the precision of module components, among other considerations. Commercial solutions often offer guidance and support to overcome these challenges, nevertheless it is still advisable to independently verify the provided information to ensure its accuracy and suitability for specific research requirements.

Herein, we describe the development of a versatile automated station designed for the high-throughput preparation of reactant mixtures for a wide range of inorganic synthesis processes. It has been developed during this thesis and used to synthesize LFMO and LNMO materials through sol-gel synthesis. The station comprises one module, Batteryino-I, that is dedicated to wet-syntheses, including techniques like sol-gel and Pechini methods, and also to solid-state synthesis. In Figure 9, Batteryino-I is depicted and its components, that will be discussed in more detail later in this chapter, are highlighted.

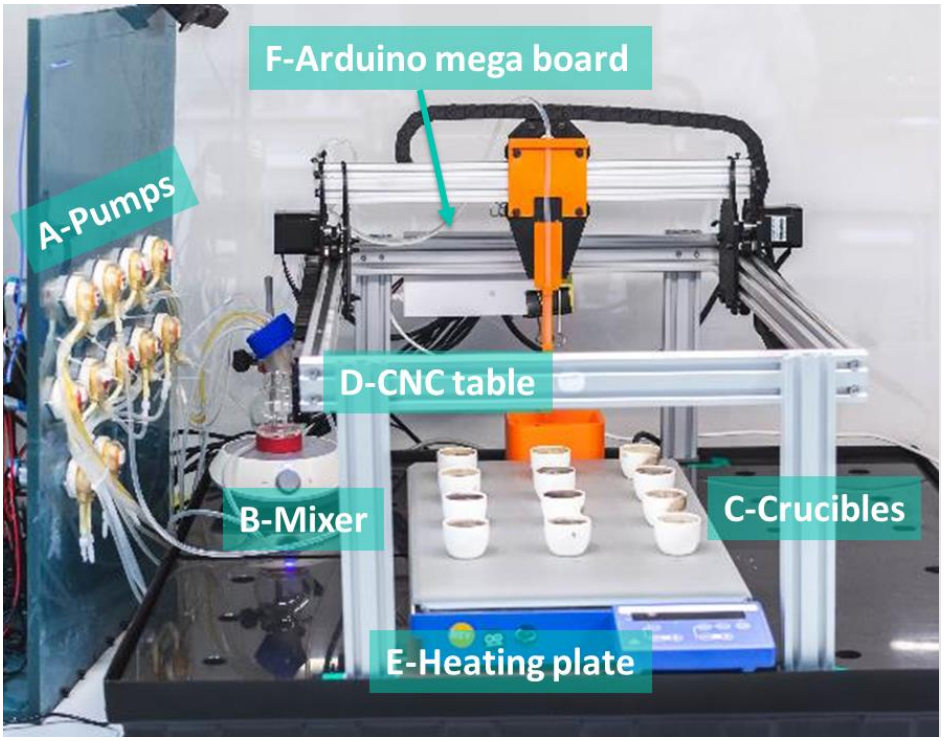

Figure 9: Automated liquid-handling module, Batteryino-I, designed to handle and mix precursor solutions at suitable stoichiometries for the mixing of inorganic solids in solution (i.e., sol-gel synthesis). Its main components (A-F) are highlighted.

This in-house designed module is based on a robotic set-up that automates liquid handling, dispensing, and mixing. This approach minimizes manual intervention, reduces human error, and contributes to overall process optimization. This choice was made (as opposed to working directly with solid reactants) to prioritize the streamline of these tasks and to ensure cost-effectiveness. Liquid handling automation offers enhanced ease of operation, allowing for efficient and precise handling of the materials involved. Moreover, the operation of the liquid handling robot requires the dispensing of reactants as uniform solutions, wherein the solubilities of reactive components determine the maximum chemical concentration range suitable for reactions. A series of pumps are used to dispense the reactant solutions (Figure 9-A). Atlas scientific

programable pumps were selected as they enable accurate dispensing of quantities that are compatible with our systems, and they are also easy to calibrate (see Section 2.4.1). The reactant solutions are combined and stirred in a round flask mixer (Figure 9-B) before being introduced into the crucibles (Figure 9-C). This approach offers the advantage of being able to add one reactant mixture into another that has already been pumped into the crucibles, which allows for achieving precise control over the mixing process and ensuring thorough homogenization of the reactants to promote efficient reaction kinetics as well as pH control. Moreover, this sequential addition capability enables the creation of complex reaction schemes by gradually introducing different reactant mixtures, facilitating the synthesis of a wide range of desired materials. In Figure 10, an example of the process for the synthesis of LFMO/LNMO can be seen. In this example there are 5 operating pumps for reagents that can be added in the desired order into the mixer before being pumped into the crucibles.

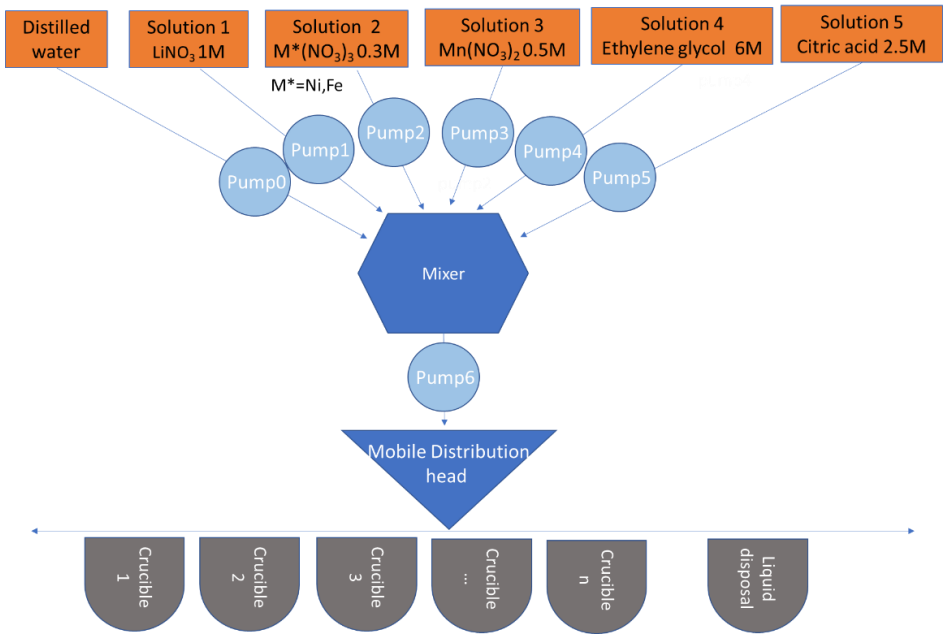

Figure 10: Map of solutions, pumps and crucibles for the developed module, Batteryino-I. The reactants shown in the figure correspond to the synthesis of LFMO/LNMO.

To dispense the solutions into the crucibles, two options were again considered: (i) a multi-axis robotic arm and (ii) a two-axes (x-y) Computer Numerical Control (CNC) table. While a robotic arm provides greater movement flexibility, it also entails more complexity in terms of programming, calibration, and maintenance. In contrast, the CNC table (Figure 9-D) proved to be a more accessible alternative, less costly and technically demanding, that offered the advantage of adaptability to the available space dimensions and proved to be more precise and reliable over time (design schemes can be seen in Annex I). Lastly, the module includes a multi-position heating and mixing plate (Figure 9-E), placed below the CNC table, which allows stirring and heating the solutions for conducting reactions and/or concentrating the resultant mixtures. Mixing of the solution is done with classical magnetic stirring.

For solid-state syntheses, the reagents are first dissolved and mixed in solution and later the solvent fraction is entirely evaporated prior to the annealing step, for which the crucibles containing the mixture of reactants are transferred to the ovens using quartz trays (Figure 11). These customized trays also ensure consistent placement of the crucibles inside the oven, which allows correlating the crucible position in the oven with the final material's features (see Section 2.4.3). The muffle and tubular furnaces used to perform syntheses under air and controlled atmospheres, respectively, are equipped with programmable temperature controllers. These controllers play a role in maintaining precise control over the heating and cooling ramps during the synthesis processes, ensuring optimal reproducibility of the experiments by facilitating comparison and validation of results.

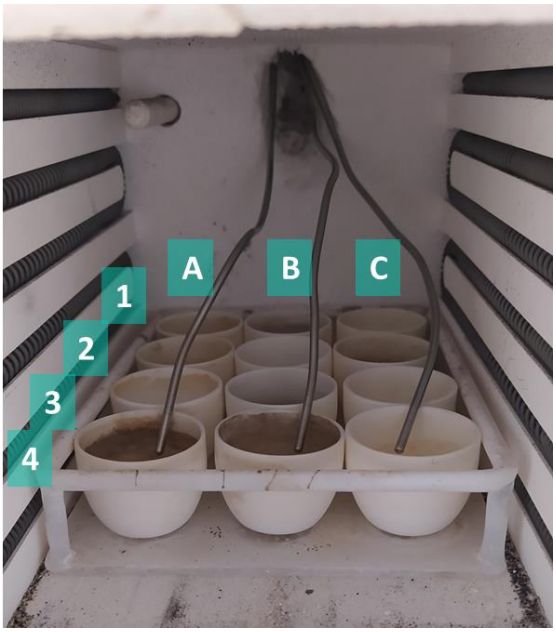

Figure 11: Photography of the 12 crucibles placed in the quartz tray inside of the oven. The thermocouples used for the oven calibrations can be observed inside of three of the positions. The labelling of the crucibles is also indicated by a combination of columns (A, B and C) and lines (1, 2, 3, 4).

2.3. Workflow

For the control and coordination of the entire hardware system described earlier, an Arduino Mega board was chosen as the microcontroller (Figure 9-F). Arduino is an open-source electronics creation platform based on free hardware and software. It has played a pivotal role in simplifying the process of building and programming hardware, creating a pathway for individuals to develop their own electronic devices and projects.[131,132] The Arduino Mega is based on the ATmega2560 microcontroller, which is a high-performance 8-bit AVR microcontroller. It operates at a clock speed of 16 MHz and has 256 KB of flash memory for storing program code. Compared to other Arduino boards or microcontrollers, the Arduino Mega boasts a significantly higher number of I/O pins and extra memory. This makes it suitable for projects that require simultaneous connections to numerous sensors, actuators, or

external devices. It provides flexibility in handling multiple inputs and outputs, enabling the integration of complex systems.

The experimental parameters are first written in the Arduino code for each set of experiments (an example can be found in Annex I). This code is subsequently uploaded onto the Arduino microcontroller and, once the code is read, it takes charge of orchestrating the experimental workflow according to the predefined parameters. The experimental workflow for sol-gel syntheses is illustrated in Figure 12 where the sequence of steps and actions necessary to carry out successful synthesis processes within the system is outlined.

At the beginning of the experimental process, the reactant solutions are prepared in large quantities at the desired concentrations. The reactant solutions are stored for a certain set of syntheses depending on the amount required. Final concentrations of the solutions are diligently examined prior to each set of syntheses using chemical titration or ICP analysis. Solutions containing reactants prone to oxidation (such as Fe^{2+}-based solutions) are continuously degassed with N_2 bubbling.

Batteryino-I module is designed to simultaneously prepare 12 samples. The reactants for the first sample are pumped into the mixer from the different solutions. Then, they are stirred in the mixer for a specific duration. Subsequently, the CNC table moves to align with the first crucible, into which the reactants mixture is transferred. Following this, the dispensing system undergoes a series of washing steps with distilled water (DW). Afterwards, the system is ready to start the process again for the second sample. In a typical series of sample preparation, this process is repeated 12 times for 12 crucibles that are continuously stirred. Once all samples are prepared, they are left to stir overnight. Then, the solutions are evaporated by heating at 80°C until a solid mixture is obtained. Once the evaporation stage is complete, the crucibles are transferred into the quartz tray, which is directly placed in a muffle or tubular furnace to carry out the annealing step. After the thermal treatment, 300-400 mg of each sample are typically recovered. This amount of sample allows for the execution of all the required

characterization techniques on a single sample, ensuring consistency and representativeness in the analysis.

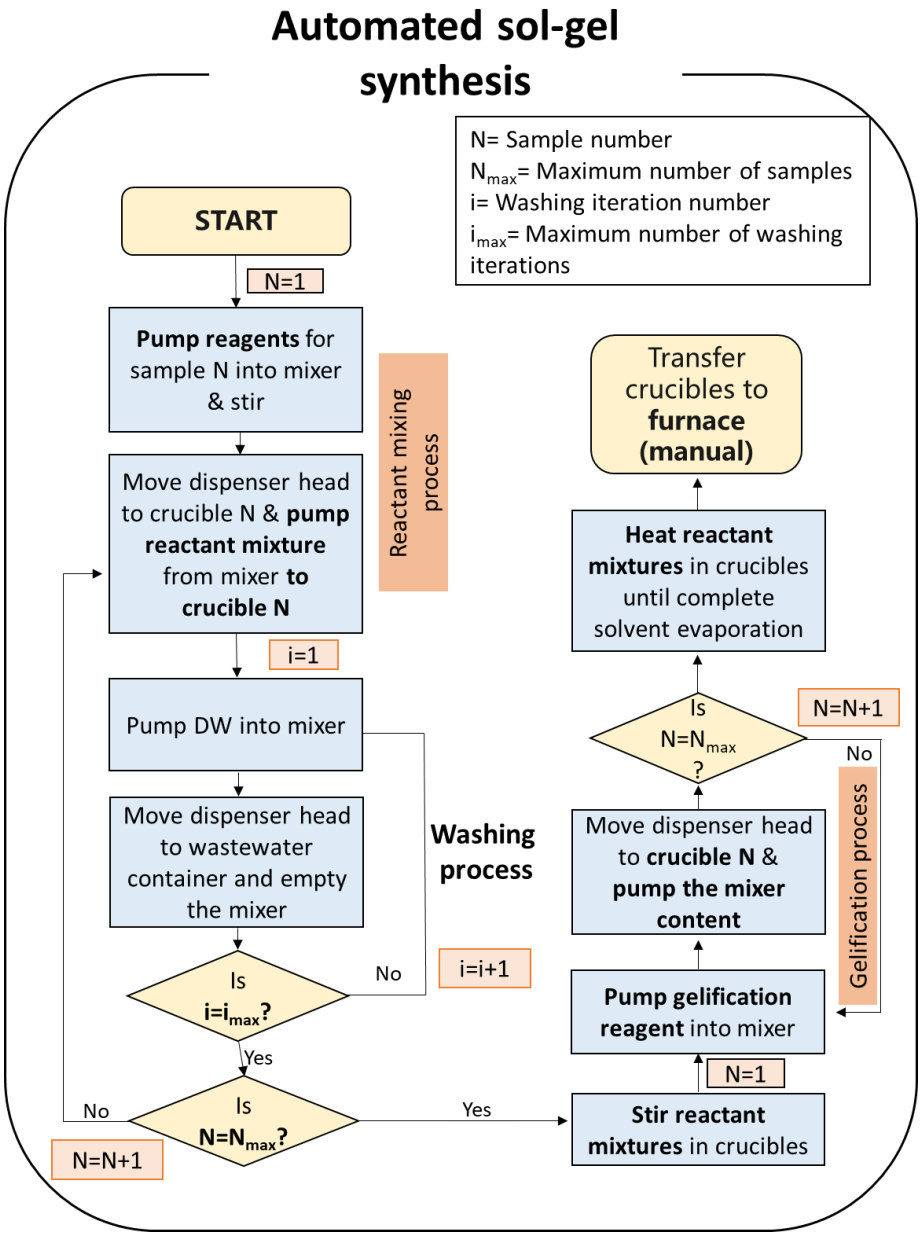

Figure 12: Program workflow for sol-gel synthesis followed by Batteryino-I. The volume of pumped reactant solutions is specific for each sample, N, and is indicated in the code.

2.4. Reproducibility considerations

Calibrations, optimization, and reproducibility validation are essential for maintaining accuracy, reliability, and transparency in scientific research, engineering, and data analysis. Achieving full reproducibility of the system was a challenging endeavor, given the multitude of variables that necessitated thorough consideration (calibrations; thermal distribution in the heating plate, ovens, and crucibles; evaporation homogeneity, ventilation of the environment, etc.). For example, a study on the thermal distribution in the heating plate was undertaken to improve the evaporation conditions and provide uniform behavior across all positions to enable accurate and optimal operation of the module and ensure the quality of the results. Furthermore, both the pumps and the ovens are calibrated on a regular basis to ensure precision and reliability. The most relevant actions undertaken to attain reproducible results are described below.

2.4.1. Pumps

For the pump calibration, a specified volume is chosen, then the amount of distilled water pumped is weighed manually and this number is returned to the software, which corrects the value. The calibration for that volume is then completed.

The tolerance limit for the solution delivery has been established at 0.1 mL since the amount of metal moles in solution at this volume is insufficient to produce a measurable difference in our samples. Furthermore, the molarities of the solutions have been chosen to be sufficiently low to prevent exceeding this limit. To ensure that the quantities pumped remain within the tolerance limit throughout time, two tests were performed. On the one hand, the calibration was done using the same volume used by that specific pump during the synthesis and then the same amount of distilled water was pumped 50 times and weighed each time to detect any fluctuations over time. On the other hand, the pump was calibrated at 5 mL and then configured to pump distilled water 5 times 3 mL, 5 times 5 mL, and 5 times 8 mL. The pumped volume is then weighted to monitor pump stability. Figure 13 shows how all pumps produced similar

results upon the number of orders within a tolerance value of 0.1mL.

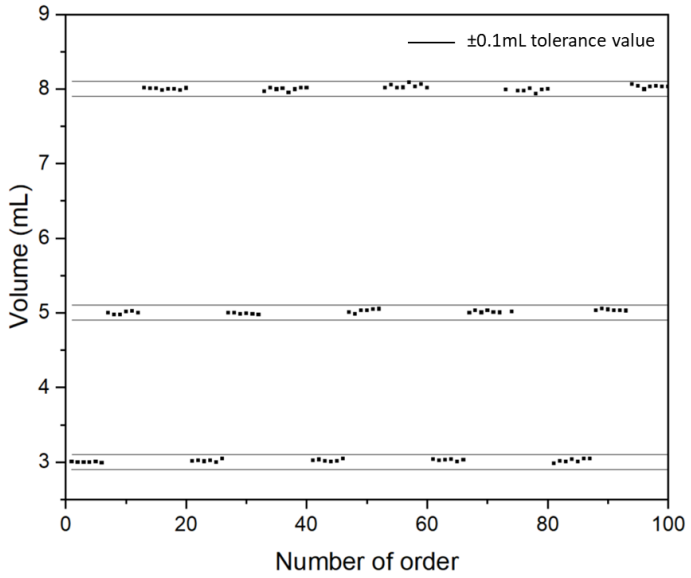

Figure 13: Calibration of one pump dosing different volumes (3, 5 and 8 mL) versus the number of orders. The lines indicate an error tolerance of 0.1 mL.

2.4.2. Study of the thermal distribution of the heating plate

The thermal uniformity of the heating plate was checked to assure reproducibility during the sol-gel synthesis. This was accomplished by employing an infrared camera (See Chapter 6, Section 6.2.2).

Figure 14-a shows the temperature evolution of the reactants in the crucibles when these were in direct contact with the heating plates. The data obtained shows that the temperature distribution across the 12 positions was not uniform. Variances as high as 10°C were observed between different positions, highlighting the need for temperature control optimization in the system. This was solved by placing silicone oil or silicon grease at the bottom of the crucibles to improve contact between the two surfaces. Following this approach, the appropriate temperature was obtained faster and

remained consistent during the evaporation, as shown in Figure 14-b for one of the crucibles.

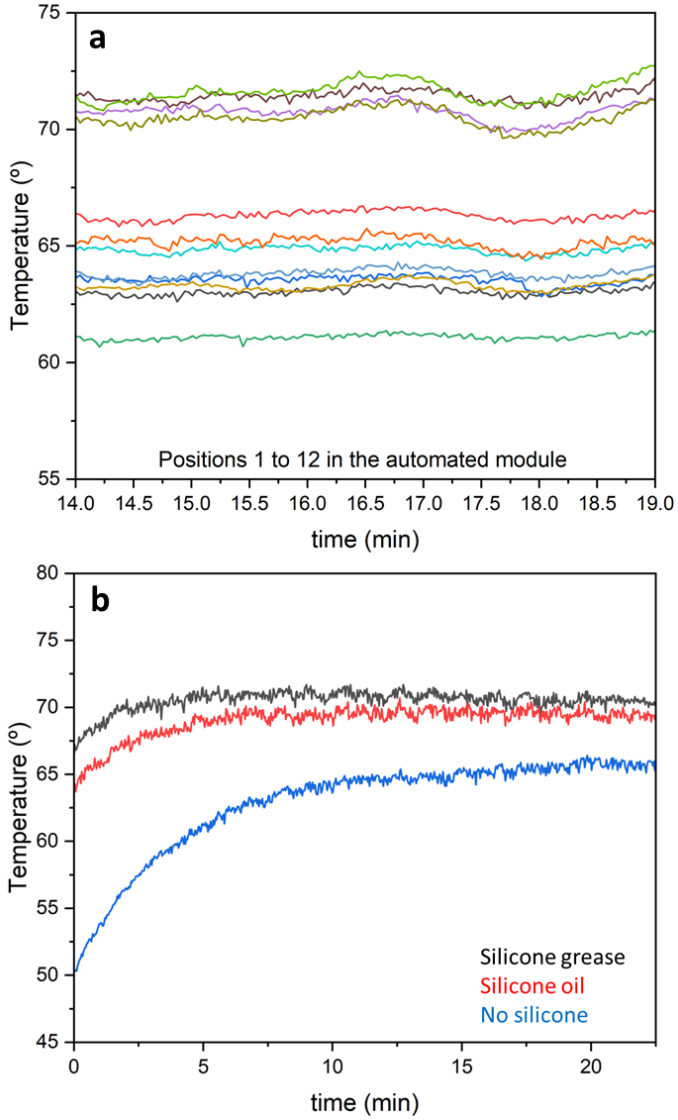

Figure 14: Temperature evolution of the reactant solutions in the crucibles. (a) Temperature corresponding to different positions measured under identical conditions and with direct contact between the crucibles and the plate; each position is represented by a different color. (b) Temperature corresponding to a single alumina crucible positioned in the heating plate under different conditions: direct contact (blue), adding silicone grease (black) and silicone oil (red) at the bottom of the alumina crucible.

2.4.3. Muffle and tubular furnace

The platform includes two types of heating systems: a muffle, to perform annealing processes under air, and a tubular furnace to be able to work under controlled atmosphere (i.e., Ar/H_2, Ar, O_2). Both the muffle and the tubular furnaces have been calibrated. To ensure sample traceability, a specific tray has been designed for each. The tray designed for the muffle includes 12 positions (Figure 11), while the tray for the tubular furnace has 8 positions. For the muffle furnace, the labelling of the positions corresponds to a combination of columns (A, B and C) and lines (1, 2, 3, 4). For the tubular furnace, the labels correspond to the right (E) and left (D) parts of the tube and, for each side, positions are numbered (1, 2, 3, 4).

Thermocouples were employed for the furnaces calibrations, placing them in each crucible position. For the muffle furnace, the temperature was screened from 700°C to 950°C, measuring each 50°C. For the tubular furnace, a screening of five temperatures from 200°C to 950°C weas done. The measurements were done after 1h of stabilization of the temperature.

Figure 15 illustrates the temperature gradient in each of the 12 positions of the muffle furnace for four different sets of temperatures. In the Figure, each calibrated temperature is accompanied by the average value (A) and the standard deviation (SD) of the measurements. The data indicates that the temperature inside the muffle is not uniform, leading to fluctuations of approximately ±10°C across different sample positions. The tubular furnace faces a similar issue but with a more significant variance (Figure 16), reaching up to -38°C in locations closer to the open parts of the tube. These positions were therefore discarded for the synthesis. In the rest of the positions, the variation fluctuates from -7°C to 28°C with respect to the targeted temperature. Since it was not possible to solve these differences, the average temperature, and the standard deviation (corresponding to 3 measurements) with respect to the selected temperature for each position is used as metadata for each sample.

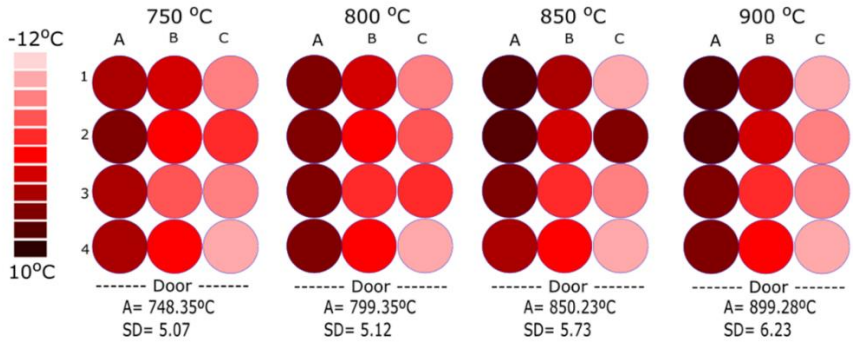

Figure 15: Results of the muffle furnace calibration conducted at different temperatures for the 12 crucible positions in the muffle furnace. Variations with respect to the selected temperatures are given in different tonalities.

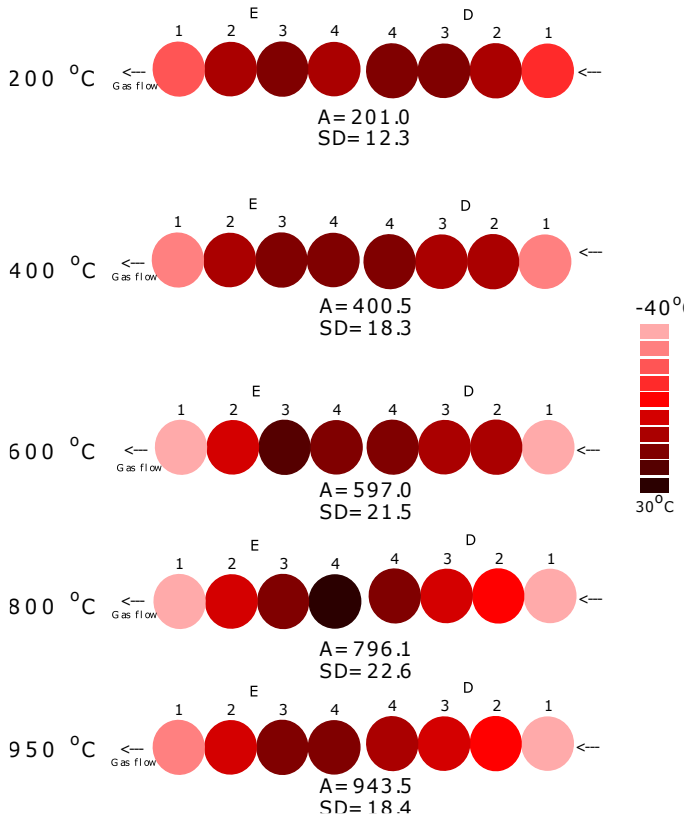

Figure 16: Results of the tubular furnace calibration conducted at different temperatures for the 8 crucible positions in the tubular furnace. Variations with respect to the selected temperatures are given in different tonalities.

2.5. Experimental validation of the module – Case studies

Once the module was optimized, two Li-ion electrode systems were selected as case studies to validate the efficiency of the automated module: $LiFe_{0.5}Mn_{1.5}O_4$ (LFMO) and Li-Ni-Mn oxides. For the first, 12 samples were synthetized under identical conditions in all 12 crucible positions in order to assess the reliability and reproducibility of the module. Next, a combinatorial synthesis of 48 samples of the Li-Ni-Mn-O pseudo-ternary phase diagram. This screening process aimed to demonstrate the capability of the module to facilitate high-throughput synthesis and enable the exploration of several compositions of the phase diagram. The results obtained in these validation processes are described below.

2.5.1. Case study 1: Reproducibility validation of the sol-gel synthesis of $LiFe_{0.5}Mn_{1.5}O_4$

Twelve LFMO samples were prepared using the sol-gel method with Batteryino-I under identical conditions. The detailed synthetic procedure is described in Chapter 6. X-ray diffraction (XRD) was employed to characterize the samples after they were synthesized. Figure 17 compares the XRD patterns of the 12 synthesized materials. It demonstrates that, in all the 12 positions of the module, a pure spinel phase of LFMO is achieved. No significative change in relative intensity, nor in peak broadening is observed.

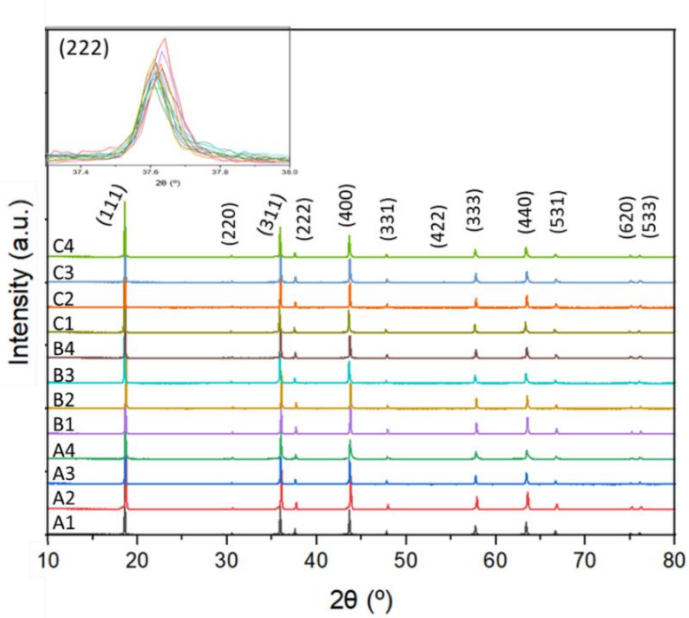

Figure 17: Comparison of the XRD patterns of the $LiMn_{1.5}Fe_{0.5}O_4$ spinel samples synthesized in the 12 positions of the automated module (labeled from A1 to C4). An enlargement around the diffraction peak (222) is shown on the upper left part of the figure.

The pseudo-Rietveld refinements of the 12 patterns against the cubic spinel structure of $LiMn_{1.5}Fe_{0.5}O_4$ were performed using the FullProf Suite[133,134]. Full Rietveld refinements were not performed as atomic parameters were fixed for simplicity, but cell parameters and profile parameters were refined for all samples, and the background was introduced using the automatic background tool of WinPLOTR[135] (see Section 6.2.2. in the Methods chapter for more details). The obtained results are shown in Figure 18, Table 4 and Table 5. The refined unit cell parameters of the twelve samples were found to be comprised between 8.297(2) and 8.307(2) Å, with an average cell parameter of 8.301 Å (Table 4). Although there are slight variations in the effective annealing temperature of the 12 samples resulting from the use of different positions in the muffle furnace (as explained in section 2.4.3), the obtained structural parameters are comparable. This demonstrates the reproducibility of the synthesis approach, indicating that the method consistently yields similar outcomes despite minor temperature discrepancies. Furthermore, the same synthesis has been carried out in the same

crucible position on different days, obtaining reproducible results with differences in the fourth decimal of the cell parameter (not shown). The LFMO system synthesized using Batteryino-I will be further studied in Chapter 4.

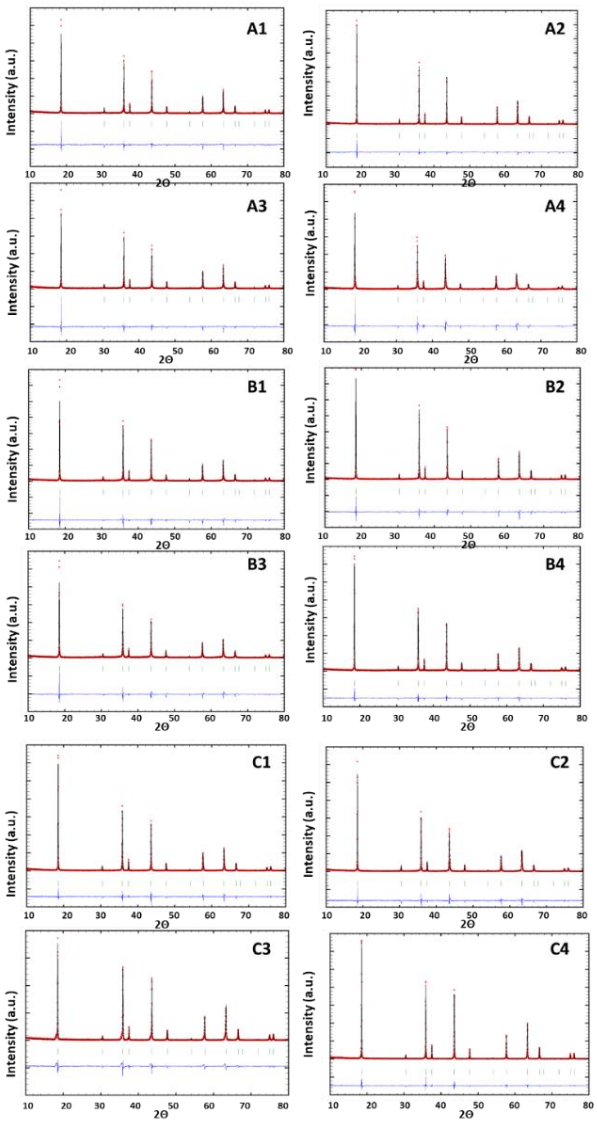

Figure 18: Pseudo-Rietveld refinements of the LFMO synthesized in the 12 crucible positions of the automated platform. In green the Bragg positions, in black the calculated XRD pattern, in red the observed patterns are represented and, in blue the difference between observed and calculated is shown.

Unit cell	$LiFe_{0.5}Mn_{1.5}O_4$					
Sample	**A1**	**A2**	**A3**	**A4**	**B1**	**B2**
Cell par. *a/b/c* (Å)	8.304(2)	8.298(18)	8.304(2)	8.300(4)	8.305(2)	8.306(2)
Volume (Å³)	572.7(3)	571.4(2)	572.6(3)	571.8(4)	572.9(3)	573.1(2)
Sample	**B3**	**B4**	**C1**	**C2**	**C3**	**C4**
Cell par. *a/b/c* (Å)	8.302(3)	8.297(2)	8.299(2)	8.301(2)	8.299(3)	8.296(15)
Volume (Å³)	572.3(3)	571.2(2)	571.7(3)	572.0(3)	571.7(3)	571.1(18)

Table 4: Unit cell parameters obtained from the pseudo-Rietveld refinements of the XRD patterns of the 12 LFMO samples synthesized in the same conditions using the automated module Batteryino-I.

Conventional Rietveld R-factors	$LiFe_{0.5}Mn_{1.5}O_4$					
Sample	**A1**	**A2**	**A3**	**A4**	**B1**	**B2**
Rp	28.5	18.8	30	36.2	31.8	24.1
Rwp	35.3	26	34.7	39.5	36.9	31.2
Rexp	15.49	13.6	15.68	15.98	14.98	13.13
RBragg	2.55E-03	0.00576	9.99E-03	1.97E-03	6.18E-03	1.53E-03
Rf	2.45E-03	0.00577	2.05E-01	5.65E-03	8.68E-03	8.57E-04
χ^2 (Bragg)	5.18	3.65	4.91	6.1	6.06	5.64
Sample	**B3**	**B4**	**C1**	**C2**	**C3**	**C4**
Rp	34	21.1	22.4	25.6	26.5	13.8
Rwp	36.8	25.4	27.1	30	35.4	20.9
Rexp	16.13	14.65	14.45	15.05	15.36	12.72
RBragg	2.07E-02	2.21E-03	1.22E-02	5.06E-02	2.59E-03	6.18E-03
Rf	2.69E-02	3.21E-03	1.73E-02	4.08E-02	1.51E-02	2.84E-02
χ^2 (Bragg)	5.19	3	3.53	3.98	5.31	2.7

Table 5: Conventional Rietveld factors for the Pseudo-Rietveld refinements of the 12 LFMO samples synthesized in the same conditions using the automated module Batteryino-I

2.5.2. Case study 2: screening of Li-Ni-Mn oxide ternary phase diagram by sol-gel synthesis

In this case, 48 Li-Ni-Mn oxide samples were synthesized via sol-gel process under the same conditions, but with different stoichiometries for each sample to illustrate the capabilities of the platform to perform combinatorial synthesis. The synthetic procedure is described in Chapter 6 (Section 6.2.1.). The module enabled to successfully explore a subset of compositions of the Li-Ni-Mn ternary phase diagram by varying the Li:Ni:Mn ratio. Figure 19 illustrates the Li-Ni-Mn ternary phase diagram, highlighting the specific phase domains that were identified during the study. Synchrotron XRD was used to characterize the samples after they were synthesized. The XRD patterns of the 48 synthesized materials are compared in Figure 20 following the same color code as in Figure 19. These patterns were subjected to pseudo-Rietveld refinements using our in-house developed program called FullProfAPP. The results of the refinements for 4 selected samples are shown in Annex I.

According to the results obtained, the samples can be categorized into three distinct regions that are highlighted in Figure 19 and Figure 20 in different colors:

1) **Region 1**, with nominal composition $LiNi_{0.5+x}Mn_{1.5-x}O_4$ ($0 \leq x < 1$), in yellow: For x=0, spinel $LiNi_{0.5}Mn_{1.5}O_4$ is obtained. As the value of x increases, a second phase, identified as a rock-salt appears. This rock salt phase has ubiquitously been reported as secondary phase in samples that deviate from the theoretical stoichiometry.[87] As proposed by our group, this rock-salt phase contains both Mn and Ni in a lower ratio than in the spinel phase (ca. 2 to 1 vs 3 to 1) and is indexed with a cell parameter of 8.28 Å corresponding to a 2a2b2c supercell (only the doubling of the cell parameter allows indexing the reflections shown in Figure 21 at 10-25º).[136] Our results thus suggest that the spinel phase cannot accommodate additional nickel, and as Ni increases, the amount of rock salt phase increases. The two phases coexist throughout the whole

compositional range, although little spinel is left at the composition with the highest Ni amount.

2) **Region 2**, with nominal composition $Li_yNi_{0.5+x}Mn_{1.5-x}O_4$ ($0<x<0.5$; $1<y<2$), in blue: For $x=0$, $LiNi_{0.5}Mn_{1.5}O_4$ spinel is obtained. As the values of x and y increase, and thus, the Ni and Li content, firstly a phase identified as Li_2MnO_3 (*C*12/*m*1) layered oxide appears to compensate the Li excess and, secondly the same rock salt found in Region 1 appears in this region to compensate the Ni excess. Furthermore, with the increase of these phases, the $LiNi_{0.5}Mn_{1.5}O_4$ spinel content decreases. No changes in the cell parameters of these phases are observed in this range, which indicates that no solid solution domains are identified for none of the phases. At the end of this region a layered oxide (*R*-3*m*) seems to appear at the expense of the Li-rich phase, however the different phases are hard to identify due to the structural similarity and the quality of the data.
3) **Region 3**, with nominal composition $Li_yNi_{0.5+x}Mn_{1.5-x}O_4$ ($0.5<x<1$; $2<y<3$), in green: A single-phase solid-solution domain of a layered oxide $Li_aNi_{0.5+b}Mn_{0.5-b}O_2$ (*R*-3*m*) is identified. It can also be highlighted that, in contrast to Regions 1 and 2, no rock salt phase was found in this region.

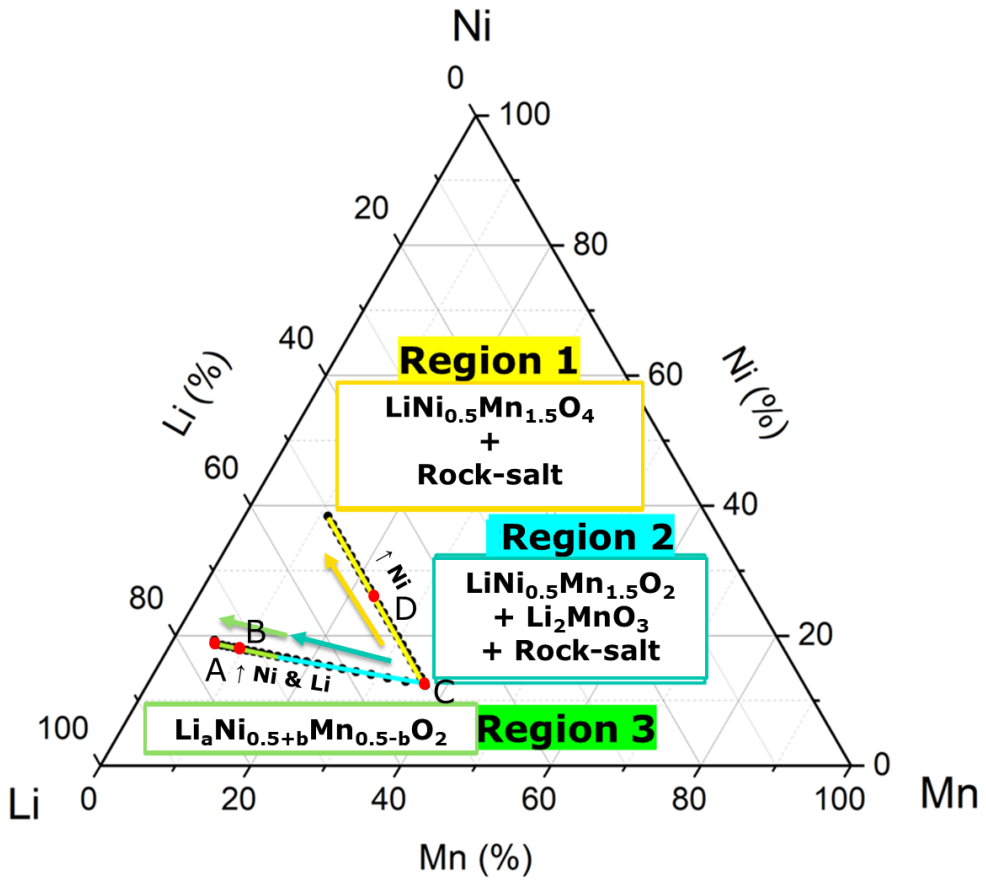

Figure 19: Pseudo-ternary phase diagram obtained for the Li-Ni-Mn oxide system. Black points represent the targeted compositions, and the colored lines represent the single/two-phase regions obtained for the different areas. The obtained phases are indicated as headings for each Region. A, B, C and D points correspond to the refinements shown in Annex 1.

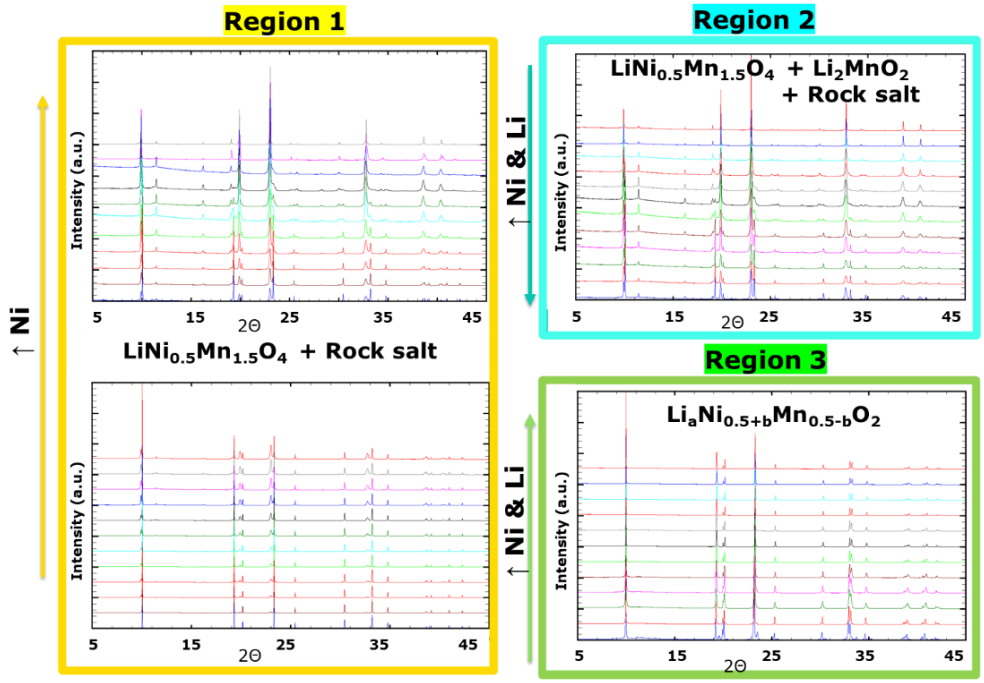

Figure 20: The diffractograms obtained for the 48 synthesized samples. The colored arrows indicate the increasing amount of Ni and Li in the targeted composition, according to the arrows showed in Figure 19, and the obtained phases are indicated as headings for each Region.

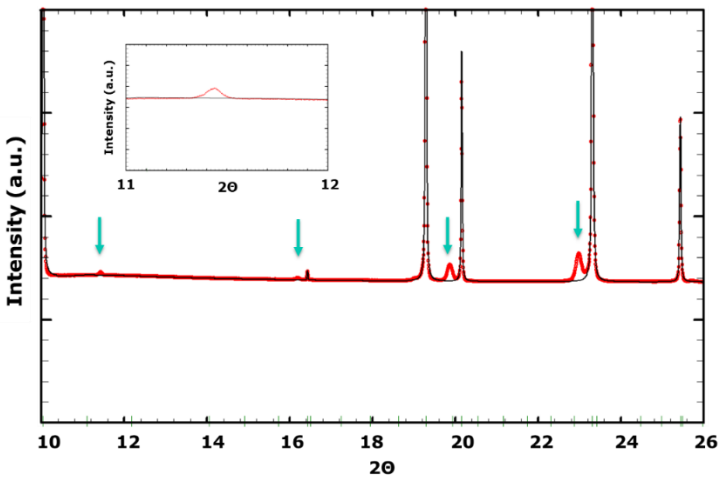

Figure 21: Zoom of the refinement of point C (see Figure 19) indexed with LNMO and a rock-salt with a cell parameter of 4.14 Å. The arrows indicate the non-indexed peaks.

2.6. Conclusions

An advanced automated platform for inorganic synthesis has been successfully developed and validated for sol-gel synthesis during this thesis. This module paves the way for faster material development and improved repeatability, reducing R&D costs and time. To validate the effectiveness of this platform, different experiments using two electroactive compounds (LFMO and LNMO) have been conducted. Remarkably, by employing Batteryino-I, the capability to perform sol-gel synthesis on 12 LFMO samples simultaneously using the same equipment has been demonstrated. Despite minor temperature variations among different oven positions, the results obtained were comparable. This enables rapid and precise combinatorial synthesis, as exemplified by the successful creation of 48 Li-Ni-Mn oxide samples within the ternary phase diagram.

Overall, it has been put forward that the presented automated platform might contribute to enable the implementation of self-driving MAPs for inorganic materials, which have the potential to revolutionize the field by enabling continuous autonomous exploration and optimization of materials, leading to accelerated innovation and breakthroughs in energy storage and beyond.

CHAPTER 3: Theoretical study of the electrochemical properties of $LiFe_{0.5}Mn_{1.5}O_4$ using SCAN and PBE+U functionals

3.1. Abstract

This chapter presents an investigation of $LiFe_{0.5}Mn_{1.5}O_4$ electrochemical properties performed by first principles calculations. We examine the phase stability and voltage evolution of LFMO during delithiation using density functional theory calculations with two different approaches: PBE+U and SCAN functionals. The findings indicate that the transition metal distribution within LFMO has minimal impact on its phase stability or voltage behaviour, and that the electrochemical process is suggested to take place through a solid solution mechanism. The redox activity of $Li_xFe_{0.5}Mn_{1.5}O_4$ is primarily governed by the $Mn^{3+/4+}$ redox couple in the range of $1 \geq x \geq 0.5$ whereas the $Fe^{3+/4+}$ couple operates in the region of $0.5 \geq x \geq 0$. A further investigation of the redox process reveals an anionic contribution that is shown to be reversible in the case of SCAN functional. With its exceptional stability, improved performance, and low cost, these results encourage further investigation of LFMO as an interesting option for the next generation of high-voltage, environmentally friendly lithium-ion batteries.

3.2. Computational approach

In the computational model of LFMO we have started from an ideal structure, ignoring the possibility of having defects although in chapter 4 the impact of the antisite defects in the electrochemical performance will be further studied from an experimental point of view. The present chapter specially addresses the configurational disorder in terms of Fe/Mn and Li vacancies (Li/V_{Li}). To generate these configurations the clusters approach to statistical mechanics (CASM) code[137], described in Chapter 6, have been used. The Fe/Mn distinct distributions within the $LiFe_{0.5}Mn_{1.5}O_4$ composition have been generated using a supercell containing 8 $LiFe_{0.5}Mn_{1.5}O_4$ formula units (f.u.). The energies of the 22 resulting possible structures have been computed using the common used PBE+U functional[138] and they are shown in Table 6. From these structures, the most stable Fe/Mn distributions with energies in the range of the thermal energy at room temperature (<19 meV/f.u. from the absolute energy minimum, depicted in green in Table 6) were considered for a deeper analysis. In total, six distinct Fe/Mn distributions, plotted in Figure 22, have been taken into consideration for a deeper study.

Structure	Total energy (meV/cell)	Difference with respect to the most stable structure (meV/cell)
1	**-376.2**	**0.0**
2	**-376.1**	**16.3**
3	**-376.1**	**16.0**
4	**-376.2**	**3.1**
5	**-376.1**	**16.1**
6	**-376.1**	**17.6**
7	-376.0	19.5
8	-376.0	20.0
9	-376.0	25.0
10	-376.0	28.2
11	-376.0	28.7
12	-376.0	29.1
13	-375.9	38.8
14	-375.8	46.3
15	-375.8	48.4
16	-375.8	52.5
17	-375.5	87.8
18	-375.3	107.5
19	-375.2	122.6
20	-375.2	130.0
21	-375.0	151.3
22	-375.3	118.7

Table 6: Energies of the lithiated structures calculated via PBE+U and difference with respect to the most stable one. In green the structures selected for this study are remark.

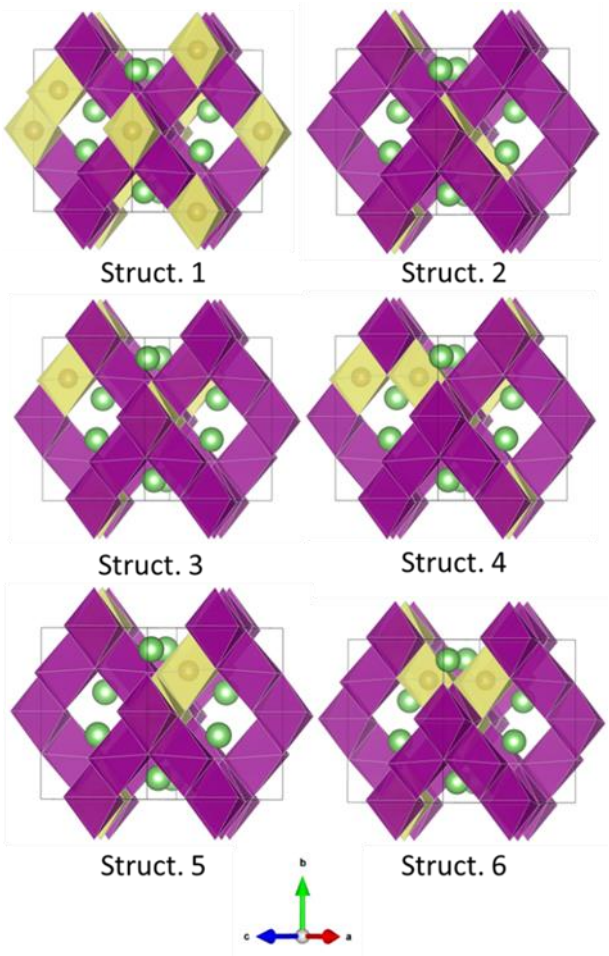

Figure 22: Structures of the six most stable Fe/Mn distributions considered for this study. The Mn polyhedral are shown in purple, Fe polyhedral in yellow, and Li atoms in green.

PBE+U method is extensively utilized in the energy storage field for its accurate calculation of electrochemical curves and intercalation voltages. However, it fixes the U parameter that is dependent on the transition metal, the structure, and the experimental voltage. Particularly, when dealing with mixed transition metals, more recent approaches are recommended, such as SCAN method that does not require fitted correction. SCAN have been shown to be more accurate in predicting the total energies and relative stabilities of solid compounds,[139–142] formation energies of Mn-based oxide polymorphs[143] and electrochemical properties of some prototype

cathode materials (such as $LiNiO_2$, $LiCoO_2$, and $LiMnO_2$)[144]. However, is currently unknown whether this method is capable of accurately reproducing the electronic structure of spinel-type materials. For this reason, SCAN functional has been selected to perform a comparative study respect to PBE+U functional of the six most stable structures identified by PBE+U (Table 6) in terms of cell volume, voltage composition curve, phase stability upon delithiation, and redox activity of the involved transition metals. All the DFT energies calculated using both functionals were performed by VASP[145,146],described in Chapter 6, and considering the LFMO spinel ferromagnetic as first approximation as it is usually done in DFT.

As described in Section 1.2, the voltage at 0K was calculated by taking Li metal as the reference anode and approximating the chemical potentials by DFT computed energies according to the following formula:

(10) $V = (E_{Li_{x2}Fe_{0.5}Mn_{1.5}O_4} - E_{Li_{x1}Fe_{0.5}Mn_{1.5}O_4} - E_{Li} \cdot (\mathrm{x2} - \mathrm{x1}))/(\mathrm{x2} - \mathrm{x1})$ [V]

where $E_{Li_{x1}Fe_{0.5}Mn_{1.5}O_4}$ is the total energy per formula unit of the least lithiated phase, $E_{Li_{x2}Fe_{0.5}Mn_{1.5}O_4}$is the total energy per formula unit of the most lithiated one, E_{Li} is the total energy per Li atom of bulk *bcc metallic Li,* and x_2 and x_1 are the lithium contents of both phases.

To understand the phase stability upon (de)lithiation the configurational disorder in terms of Li/V_{Li} was constructed using CASM, including supercells of volumes up to 3. It can be noted that the six Fe/Mn distributions considered have different symmetry, and thus, their primitive cells are different. Volume 1 is the volume of the smallest supercell (primitive cell of Structure 1), containing 4 $LiFe_{0.5}Mn_{1.5}O_4$ formula units, and Volume 2 is the volume of the supercell of structures 2 to 6, which contains 8 $LiFe_{0.5}Mn_{1.5}O_4$ formula units. Likewise, volumes 2 and 3 of the supercells contain 8 and 12 formula units, respectively, and they can be obtained expanding the smallest supercell. This allowed to thoroughly explore the Li/V_{Li} configurational space, within our available computational resources. In the case of volume 1 and 2 systems, the total energy of all symmetrically inequivalent Li/V_{Li}

arrangements were calculated. However, the number of Li/V_{Li} configurations exponentially increases for volume 3 supercells, making unfeasible the computation of all possible combinations; therefore, randomly the 15% of the total number of possible Li/V_{Li} configurations were considered (971 in total). Also, the total number of configurations of volume 2 calculated for Structure 1 (449) is higher than for Structures 2 to 6 (256, 140, 140, 160 and 160, respectively). In summary, a total of 1305 Li/V_{Li} different arrangements for volume 1 and 2 models, and 971 additional ones of volume 3 were computed (the latter only with PBE+U).

The formation energies (ΔfE) of partially lithiated $Li_xFe_{0.5}Mn_{1.5}O_4$ phases at 0K were calculated considering the following reaction and formula:

$$xLiFe_{0.5}Mn_{1.5}O_4 + (1-x)Fe_{0.5}Mn_{1.5}O_4 \rightarrow Li_xFe_{0.5}Mn_{1.5}O_4,$$

$$(\Delta fE = E_{Li_xFe_{0.5}Mn_{1.5}O_4} - (1-x)E_{Fe_{0.5}Mn_{1.5}O_4} - xE_{LiFe_{0.5}Mn_{1.5}O_4}, \quad (11)$$

where $E_{LiFe_{0.5}Mn_{1.5}O_4}$ is the energy of the totally lithiated phase, $E_{Fe_{0.5}Mn_{1.5}O_4}$ is the energy of the totally delithiated phase and x is the lithium content of the formula unit (x= 0.125, 0.25, 0.375, 0.5, 0.625, 0.75, 0.875, 1).

The Li/V_{Li} arrangements with lower negative formation energy at each lithium content and, thus, the stable phases of minimum energy, are called ground states. The energies of these ground states, for each of the six selected Fe/Mn configurations, were used to construct the respective convex hulls. The convex hull itself consists in a plot of formation energy with respect to the composition which connects the phases with lower negative energy. It helps to determine the stability of the studied compositions and whether they have a solid solution or a multiphasic behavior upon (de)lithiation depending on the situation of the ground states. If the majority of ground states lie on the convex hull line, then a preferred solid solution mechanism is obtained.

To describe the redox processes, related to both transition metals in the spinel structure, an analysis of electronic structure aspects of $Li_xFe_{0.5}Mn_{0.5}O_4$ have been performed using the Bader approach

implemented in the Bader code.[147] A Bader charge is an estimation of the distribution of electric charge on the atoms of a molecule and it helps to understand how electrons are distributed around atomic nuclei and how electronic density is linked between atoms in a molecule. The charge enclosed within the Bader volume is a good approximation to the total electronic charge of an atom and, although the Bader charge does not correspond directly to the oxidation state of a particular atom, it can be related to it. To further understand these redox processes, the projected density of states was also computed. The projected density of states (PDOS) gives the projection of a particular orbital of an atom on the density of states and by the sum over all the projections gives the total density of state (DOS) that can be related to the oxidation state of the studied atoms.

3.3. Structural parameters

By relaxing the six most stable Fe/Mn distribution structures (shown in Figure 22), using both PBE+U and SCAN functionals, the cell parameters were obtained, as depicted in Table 7. In agreement with *Cs*onka *et al.*[148], it was found that PBE+U systematically yields larger cell parameters and volumes than SCAN, with SCAN being in overall better agreement with experimental values, as generally reported in literature[149,150]. The average difference with respect to the experimental value obtained for LFMO sample (8.244(2) Å, sample Lcp-358, see Chapter 4) is 1.647% for PBE+U and -0.144% for SCAN functionals. It is important to note that the computed supercell structures deviate from the expected cubic structure. These deviations have been analyzed to understand if the affected cell parameters were deviated due to the elongation of the Mn-O bonds caused by the Jahn-Teller effect. And, in fact, as depicted in Figure 23, a clear correlation has been observed between the cell parameter distortion and the distortion caused by the Jahn-Teller effect across all structures. Although the Jahn-Teller effect is depicted just for the six selected structures calculated via PBE+U, since elongated axis coincides for both functionals, the same correlation is expected for the structures calculated via SCAN.

		a (Å)	b (Å)	c (Å)	α (°)	β (°)	γ (°)	Average cell parameter (Å)	Difference from experimental value (%)	Volume (Å^3)
Experimental (sample Lcp-357)		8.244	8.244	8.244	90.00	90.00	90.00	8.244	-	560.29
SCAN	**1**	8.091	8.432	8.178	90.00	90.00	90.36	8.234	-0.122	557.99
	2	8.146	8.455	8.097	89.99	89.44	89.74	8.233	-0.136	557.70
	3	8.090	8.431	8.180	90.00	90.00	90.37	8.234	-0.125	557.94
	4	8.128	8.128	8.443	89.99	90.01	89.69	8.233	-0.138	557.71
	5	8.175	8.175	8.337	89.40	90.60	90.00	8.229	-0.177	557.25
	6	8.264	8.264	8.162	90.19	89.82	90.20	8.230	-0.170	557.42
PBE+U	**1**	8.261	8.558	8.327	90.00	90.00	90.41	8.382	1.677	588.75
	2	8.377	8.317	8.432	89.82	90.18	89.93	8.376	1.596	587.51
	3	8.459	8.459	8.228	89.81	90.19	90.06	8.382	1.677	588.80
	4	8.308	8.308	8.512	90.01	89.99	89.99	8.376	1.607	587.62
	5	8.412	8.412	8.320	89.87	90.13	90.15	8.381	1.667	588.75
	6	8.432	8.432	8.278	89.55	90.45	90.21	8.381	1.661	588.61

Table 7: Structural parameters for the different Fe/Mn distributions calculated via SCAN and PBE+U compared with the experimental value. The deviation in the average cell parameter value with respect to the experimental value is also reported for each calculation.

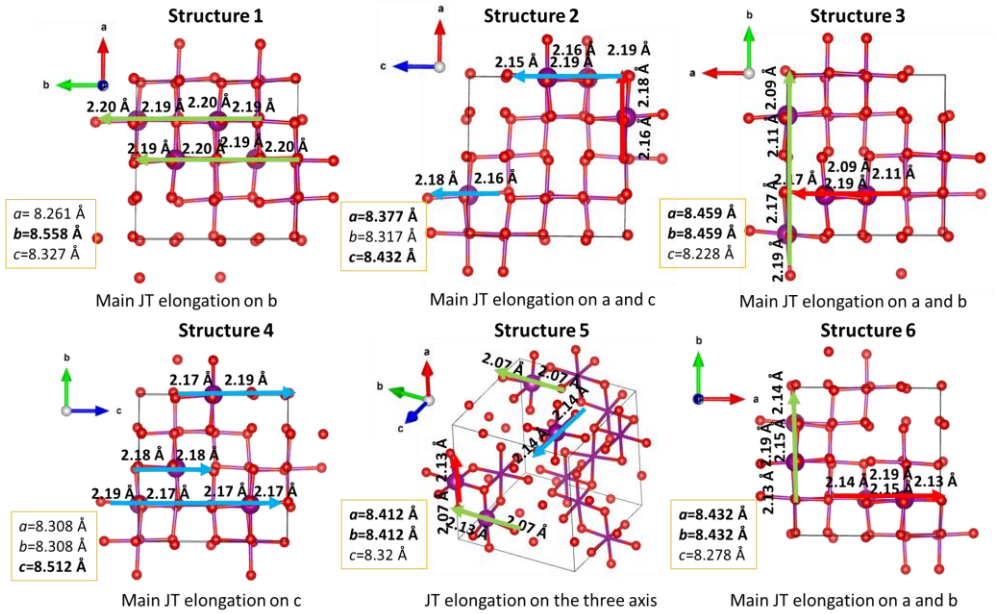

Figure 23: Representation of Mn-O bonds and Oxygen and Mn^{3+} atoms for each of the 6 fully lithiated metallic distributions calculated via PBE+U. In the yellow squares the cell parameters of each cell are indicated, in bold the longest axis. The Mn-O JT related bonds distances are indicated, and the arrows indicate the direction of the JT elongation (red for a, green for b and blue for c axis).

3.4. Electrochemical behavior

The average voltages calculated for each of the six Fe/Mn configurations are displayed in Figure 24. The voltage between $LiFe_{0.5}Mn_{1.5}O_4$ and $Fe_{0.5}Mn_{1.5}O_4$ was calculated according to formula (10). Our results reveal that the average computed voltage is not significantly affected by the Fe/Mn distribution either using PBE+U (4.390±0.018 V) or SCAN (4.096±0.025 V). Yet, the PBE+U calculations seem to be more accurate than SCAN results in reproducing the experimental average voltage of the LFMO spinel structures (4.4 V, obtained by measuring the area below the experimental curve of sample Lcp-358 shown in Figure 26 and plotted in a dash green line in Figure 24).

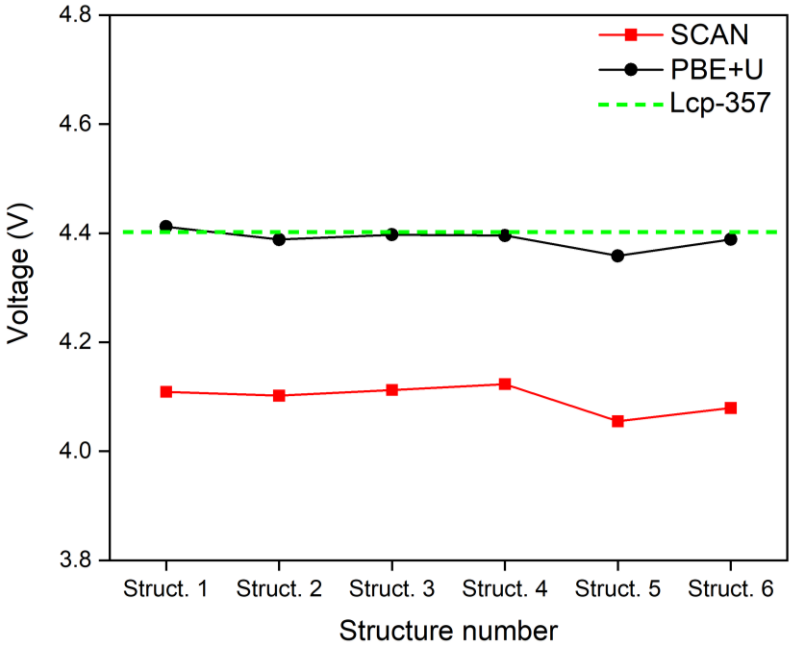

Figure 24: Comparison of the averaged lithium extraction voltages calculated using SCAN (red) and PBE+U (black) for the most stable Fe/Mn structures shown in Figure 22. The green dashed line indicates the average experimental voltage for samples Lcp-357.

The formation energies of partially lithiated $Li_xFe_{0.5}Mn_{1.5}O_4$ phases for the Li/Va_{Li} configurations at each x are depicted in Figure 25. These energies were calculated, from both PBE+U and SCAN results, according to formula (11) to further study the phase stability of LFMO during (de)lithiation. Independently of the method used, all the Fe/Mn distributions that were taken into consideration display a consistent behavior upon (de)lithiation (Figure 25): i) The majority of them exhibit negative formation energies, ii) they all yield the minimum formation energy at x = 0.5, and iii) for a given amount of lithium, the difference in formation energies between the most stable Li/V_{Li} configuration and next alternative metastable structures forms a continuous and increasing range. Moreover, when analyzing the full range of computed Li/V_{Li} configurations, a representative convex hull is observed, wherein the majority of the lowest energy configurations for each value of x lie along the hull line. In Figure 25, the squares placed in each ground state represent the relative affection of temperature and it can be highlighted that

even including a temperature of 298K (E= *K*T= 25meV) few Li/Va_{Li} configurations lie into the same energy range. This result suggests that the (de)lithiation mechanism of $Li_xFe_{0.5}Mn_{0.5}O_4$ proceeds through the formation of a solid solution.

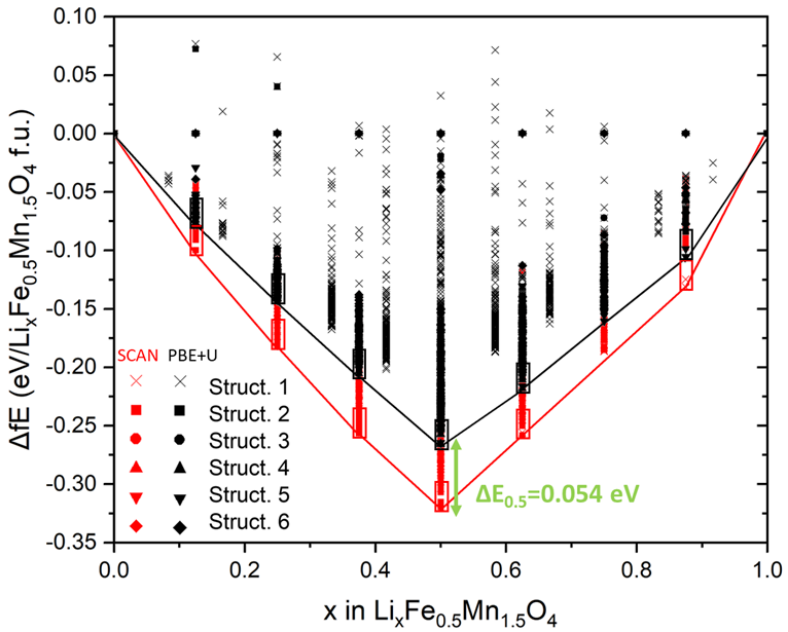

Figure 25: Formation energy (in eV/$Li_xFe_{0.5}$ $Mn_{1.5}O_4$ per formula unit) as a function of Li content for the 6 selected Fe/Mn distributions calculated using PBE+U (black) and SCAN (red). The difference in energy at x=0.5 between the ground states of both functionals is indicated in green. The squares represent the 25 meV/f.u. related to TK at T=298K to examine the effect of temperature in the system. In Annex II (Figure 57) the formation energies calculated via SCAN and PBE+U can be seen separately indicating the difference in between the different Fe/Mn distributions.

The voltage-composition curves have been computed using the resulting energies of the convex hull ground states for both functionals according to formula (10) (described in Section 3.2.). The comparison of the resulting voltages with the experimental curve is displayed in Figure 26. The formation energies of the ground states are higher for PBE+U functional compared to SCAN, using PBE+U exhibits a voltage window that is 0.4 V higher for Mn and 0.25 V higher for Fe related plateaus. We predict an almost 1 V

voltage jump at x = 0.5 from the 0K voltage composition curve of each Fe/Mn distribution for both PBE+U and SCAN functionals. This behavior is shared by all the considered Fe/Mn distributions within a voltage range of 3.5-5.0 V for PBE+U and 3.0-5.0 V for SCAN calculations, wherein PBE+U proves to be more accurate in predicting the experimental voltage plateaus and reproduces the experimental curve remarkably well. It should be considered that the experimental curve has the voltage jump at x=0.4 which may be due to the unfinalized Fe redox process and, thus, the 5V *vs.* Li/Li^+ plateau is shortened.

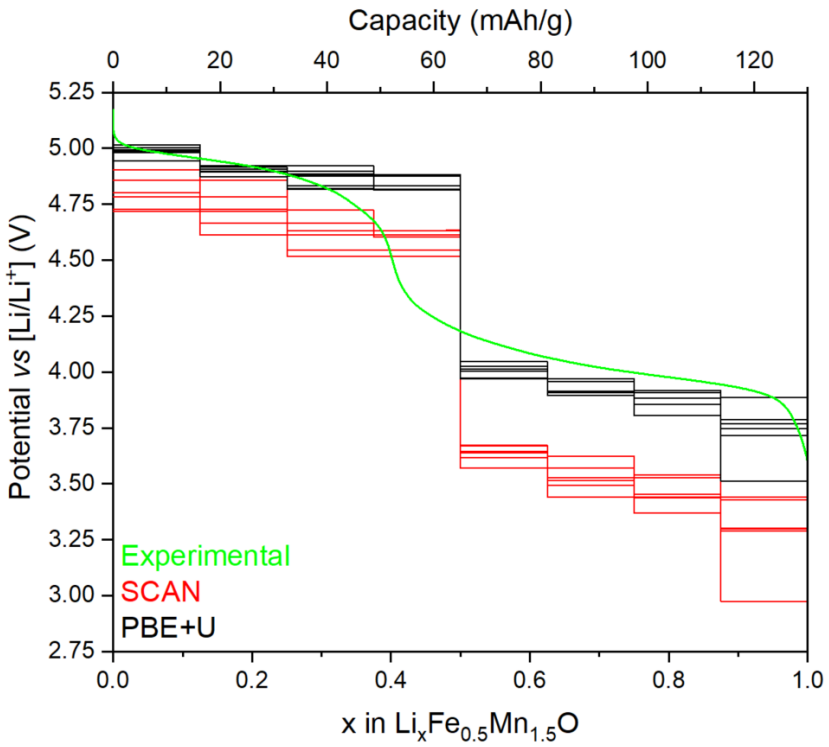

Figure 26: Voltage-composition profiles for the 6 selected Fe/Mn distributions calculated using PBE+U (black) and SCAN (red) functionals, as compared with the experimental voltage curve (green) corresponding to the discharge curve of sample Hcp-357.

The effect of the metal mixing on the voltage profile in layered oxides ($LiMO_2$; M= Cr, Mn, Fe, Co, Ti, V, and Ni) was studied by Ceder and co-workers,[151,152] who observed an increase in both the average voltage and slope of the voltage plateaus with metal

ordering. However, in our case study, the ionic radii of Fe and Mn are similar, making metal ordering unlikely. Therefore, we expect the experimental voltage curve to be an average of various Fe/Mn pseudo-ordered distributions, where periodic boundary conditions are employed. Essentially, taking the average of the voltage profiles of the different Fe/Mn distributions would bring minor voltage jumps and result in a smoother plateau.

3.5. Electronic structure analysis

Herein the focus is on the analysis of electronic structural aspects to further understand the redox processes along the (de)lithiation of $Li_xFe_{0.5}Mn_{0.5}O_4$. Firstly, Bader charges were computed to study electron transfer processes. To this end, the structures of the lowest-energy Li/V_{Li} configurations was at each investigated Li content were considered, as reported in Figure 25, for each metallic distribution. The Bader charge of all Fe, Mn, and O atoms within each supercell was calculated using both PBE+U and SCAN functionals. Table 8 shows a comparison between the obtained Bader charges of the different atoms in the LFMO and their oxidation state with respect to various cathode materials in bibliography. It should be noted that the Bader charges of atoms with the same oxidation state can slightly change between materials as they can also be affected by the polarization nature of the surrounding environment.

		Bader charges					
	System	**Li^+**	**Mn^{3+}**	**Mn^{4+}**	**Fe^{3+}**	**Fe^{4+}**	**O^{2-}**
This work	$LiFe_{0.5}Mn_{1.5}O_4$	0.89	1.71	1.84	1.78	-	-1.13
	$Fe_{0.5}Mn_{1.5}O_4$	-	-	1.82	-	1.83	-0.91
Li *et al.* 2021[153]	$LiMn_2O_4$	0.89	1.71	1.84	-	-	-1.09 (O_{Mn3+}) -1.13 (O_{Mn4+})
Xiao *et al.* 2012[154]	Li_2MnO_3	0.89	-	1.72	-	-	-1.17
	$LiMnO_3$	0.90	-	1.75	-	-	-0.88
Kubota *et al.* 2016[155]	$NaFe_{0.5}Co_{0.5}O_2$	-	-	-	1.85	-	-1.3
	$Fe_{0.5}Co_{0.5}O_2$	-	-	-	-	1.97	-0.89

Table 8: Comparison of the Bader charges associated to the different oxidation states in bibliography. O_{Mn3+} and O_{Mn4+} refers to the oxygen atoms surrounded by Mn^{3+} or Mn^{4+} ions, respectively.

The fully lithiated structure should contain 33% of Mn^{3+} and 66% of Mn^{4+} according to charge valence, considering all Fe^{3+}.[78,147] Taking this into account, the oxidation states for each Bader charge are considered in bases of the resulted Bader charges of the fully lithiated and fully delithiated structures, and, thus, it is not exact, when $Mn^{3+/4+}$ and $Fe^{3+/4+}$ are referred, it is an approximation, and thus the real value could vary (i.e. when Mn^{4+} is considered it could be $Mn^{3.8+}$). The oxidation of the transition metals occurs sequentially, with manganese oxidizing first, followed by iron, as expected. Table 9 represents the example of the Bader charges calculated via PBE+U for structure 1 in which the percentages of Mn^{3+} in each x value, calculated according to the type of Mn atom identified from their Bader charges (i.e., highest charge corresponds to Mn^{4+} and lower charge to Mn^{3+}), is indicated. A good correlation is obtained with the % of Mn^{3+} and Mn^{4+} expected from the lithium content. As the lithium content decreases, the proportion of Mn^{3+} also decreases, and at x = 0.875, the percentage of Mn^{3+} drops to 25%; at x = 0.75, it decreases to 11%; and finally, at x = 0.5, only Mn^{4+} is present. In Table 10, the example for structure 1 calculated via SCAN is shown. In this case the average Bader charge indicates the same Mn oxidation trend, but the charge localization of the individual atoms is not as clear as for PBE+U.

x in LixMn1.5Fe0.5O4														
0		0.125		0.25		0.5		0.75		0.875		1		
Atom	Bader charge	Atom	Bader charge	Atom	Bader charge	Atom	Bader charge	Atom	Bader charge	Atom	Bader charge	Atom	Bader charge	
Fe	1.81	Fe	1.82	Fe	1.81	Fe	1.81	Fe	1.82	Fe	1.82	Fe	1.80	
Fe	1.81	Fe	1.83	Fe	1.81	Fe	1.81	Fe	1.81	Fe	1.82	Fe	1.80	
Mn	1.82	Fe	1.82	Fe	1.82	Li	0.90	Fe	1.81	Fe	1.82	Li	0.89	
Mn	1.82	Fe	1.82	Fe	1.81	Li	0.90	Fe	1.81	Fe	1.81	Li	0.89	
Mn	1.80	Li	0.89	Li	0.89	Mn	1.81	Fe	1.81	Li	0.89	Li	0.89	
Mn	1.82	Mn	1.83	Li	0.89	Mn	1.81	Fe	1.82	Li	0.89	Li	0.89	
Mn	1.82	Mn	1.83	Mn	1.82	Mn	1.80	Li	0.89	Li	0.89	Mn	1.82	
Mn	1.82	Mn	1.83	Mn	1.81	Mn	1.84	Li	0.90	Li	0.89	Mn	1.86	
		Mn	1.84	Mn	1.83	Mn	1.83	Li	0.90	Li	0.89	Mn	1.82	
		Mn	1.83	Mn	1.82	Mn	1.82	Li	0.89	Li	0.89	Mn	1.84	
		Mn	1.83	Mn	1.81			Li	0.90	Li	0.89	Mn	**1.71**	
		Mn	1.84	Mn	1.79			Li	0.89	Mn	1.83	Mn	**1.72**	
		Mn	1.83	Mn	1.82			Li	0.90	Mn	1.84	**33% Mn3+ (1.7)**		
		Mn	1.84	Mn	1.83			Li	0.89	Mn	1.82			
		Mn	1.84	Mn	1.83			Li	0.90	Mn	1.84			
		Mn	1.83	Mn	1.83			Mn	1.83	Mn	1.82			
		Mn	1.83	Mn	1.81			Mn	1.83	Mn	1.84			
				Mn	1.82			Mn	1.83	Mn	1.82			
								Mn	1.83	Mn	1.84			
								Mn	1.83	Mn	**1.71**			
								Mn	1.83	Mn	**1.71**			
								Mn	1.84	Mn	1.83			
								Mn	1.84	Mn	**1.71**			
								Mn	1.84	**25% Mn3+ (1.7)**				
								Mn	1.84					
								Mn	1.84					
								Mn	1.82					
								Mn	**1.70**					
								Mn	1.83					
								Mn	1.84					
								Mn	**1.72**					
								Mn	1.83					
								Mn	**1.71**					
								11% Mn3+ (1.7)						

Table 9: Bader charges (Li, Fe, Mn,) calculated via PBE+U for structure 1. The percentage of Mn3+ is indicated below for the x in which it can be found. The Bader charges of O can be seen in Annex II.

x in LixFe0.5Mn1.5O4														
0		0.125		0.25		0.5		0.75		0.875		1		
Atom	Bader charge	Atom	Bader charge	Atom	Bader charge	Atom	Bader charge	Atom	Bader charge	Atom	Bader charge	Atom	Bader charge	
Fe	1.81	Fe	1.81	Fe	1.81	Fe	1.81	Fe	1.80	Fe	1.81	Fe	1.76	
Fe	1.83	Fe	1.84	Fe	1.83	Fe	1.79	Fe	1.81	Fe	1.81	Fe	1.80	
Mn	1.90	Fe	1.85	Fe	1.84	Li	0.90	Fe	1.80	Fe	1.80	Li	0.90	
Mn	1.89	Fe	1.81	Fe	1.82	Li	0.90	Fe	1.81	Fe	1.81	Li	0.90	
Mn	1.88	Li	0.90	Li	0.90	Mn	1.87	Fe	1.81	Li	0.90	Li	0.90	
Mn	1.90	Mn	1.91	Li	0.90	Mn	1.86	Fe	1.81	Li	0.90	Li	0.90	
Mn	1.90	Mn	1.90	Mn	1.88	Mn	1.86	Li	0.90	Li	0.90	Mn	1.87	
Mn	1.90	Mn	1.88	Mn	1.88	Mn	1.89	Li	0.90	Li	0.90	Mn	1.83	
		Mn	1.90	Mn	1.87	Mn	1.89	Li	0.90	Li	0.90	Mn	1.53	
		Mn	1.89	Mn	1.87	Mn	1.88	Li	0.90	Li	0.90	Mn	1.85	
		Mn	1.91	Mn	1.87			Li	0.90	Li	0.90	Mn	1.85	
		Mn	1.90	Mn	1.87			Li	0.90	Mn	1.91	Mn	1.87	
		Mn	1.91	Mn	1.88			Li	0.91	Mn	1.92			
		Mn	1.91	Mn	1.88			Li	0.91	Mn	1.91			
		Mn	1.91	Mn	1.88			Li	0.90	Mn	1.91			
		Mn	1.90	Mn	1.89			Mn	1.91	Mn	1.94			
		Mn	1.91	Mn	1.87			Mn	1.91	Mn	1.91			
				Mn	1.88			Mn	1.91	Mn	1.91			
								Mn	1.90	Mn	1.91			
								Mn	1.91	Mn	1.76			
								Mn	1.91	Mn	1.75			
								Mn	1.91	Mn	1.91			
								Mn	1.91	Mn	1.75			
								Mn	1.91					
								Mn	1.75					
								Mn	1.91					
								Mn	1.90					
								Mn	1.91					
								Mn	1.75					
								Mn	1.91					
								Mn	1.76					
								Mn	1.92					
								Mn	1.91					

Table 10: Bader charges (Fe, Mn, O) calculated via SCAN for the structure 1. The Bader charges of O can be seen in Annex II.

The average Bader charges of the Fe, Mn, and O ions during the (de)lithiation process for the six Fe/Mn distributions studied are shown in Figure 27. The general trend observed for Mn in the tables is well reproduced by both SCAN and PBE+U functionals (Figure 27-A). Considering the range $1 \geq x \geq 0.5$ in $Li_xFe_{0.5}Mn_{1.5}O_4$, no significant changes have been seen in Fe Bader charges and, thus, it has been considered to be in the oxidation state 3+ in this range. From x=0.5 the oxidation of iron begins. However, for $Li_xFe_{0.5}Mn_{1.5}O_4$ in the range $0.5 \geq x \geq 0$, the PBE+U approach fails to provide an accurate charge localization for Fe ions, whereas SCAN calculations consistently yield an increase in Bader charge from $Li_{0.5}Fe_{0.5}Mn_{1.5}O_4$ to $Fe_{0.5}Mn_{1.5}O_4$, indicating the redox conversion of Fe^{3+} to Fe^{4+} [78,147] (Figure 27-B). Furthermore, the large differences between configurations for both manganese and iron atoms (observed in the error bars of Figure 27-A,B) indicate that the cationic redox activity depends on the Fe/Mn distribution represented in the model and such dependance becomes more significant during the redox activity of each transition metals.

The average Bader charges of oxygen, calculated using PBE+U and SCAN functionals, are depicted in Figure 27-C. This average, and thus the oxidation state, gradually changes throughout the (de)lithiation process, from -0.90 to -1.13. Xiao *et al.* reported changes in the Bader charges from -0.88 to -1.17 attributed to the redox activity of oxygen during the lithiation process of Li_2MnO_3.[154] According to this, also LFMO could present oxygen's redox activity for the calculations performed by both functionals. Oxygen changes oxidation state to balance the charges in the delithiated structures due to the non-complete redox processes of Fe and Mn. Moreover, Figure 27-C demonstrates that the influence of the Fe/Mn distribution on the anionic redox processes is negligible throughout the (de)lithiation process, as reflected by the narrow error bars. The Bader charges upon (de)lithiation for structure 1, calculated with PBE+U and SCAN, are shown as example in Annex II.

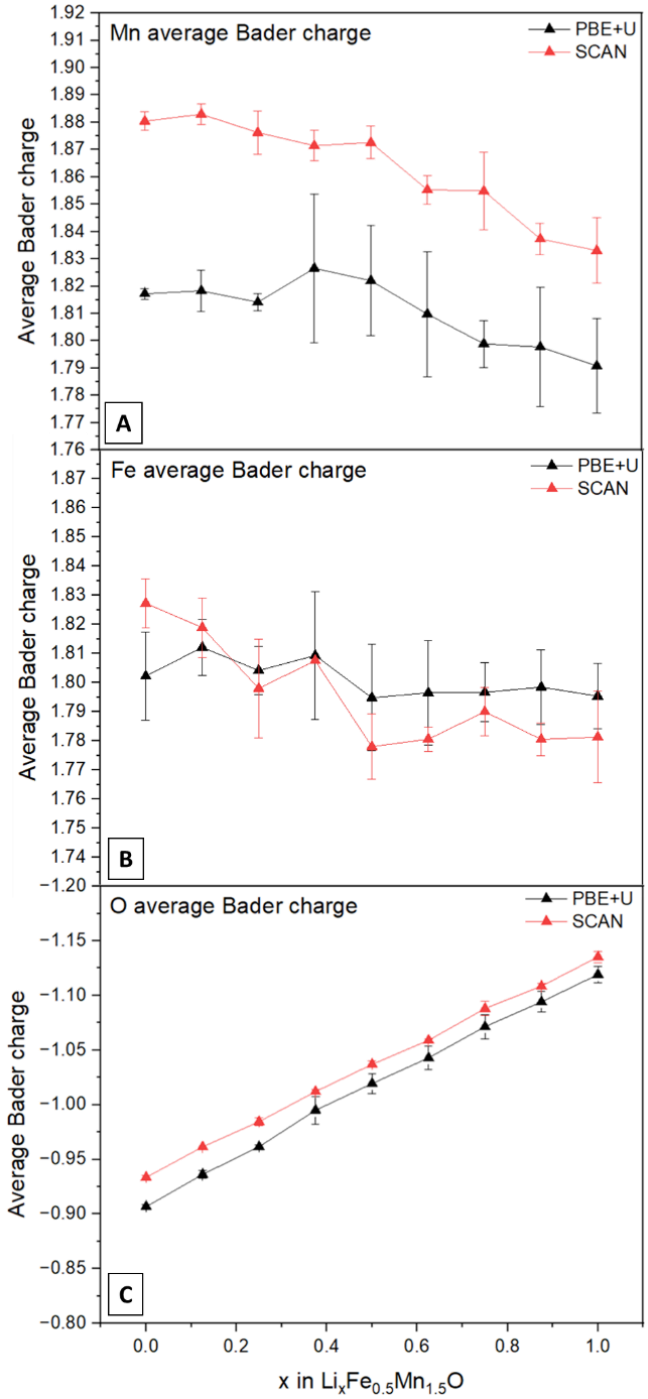

Figure 27: Representation of the average Bader charge of Fe (A), Mn (B) and O (C) ions for the 6 Fe/Mn distributions calculated using PBE+U and SCAN.

To further support the conclusions extracted from the Bader charge analysis, we also computed the projected density of states of Fe, Mn and O atoms at various degrees of delithiation using both PBE+U and SCAN functionals. In terms of occupation state, it is expected that for Fe^{3+} species, the five available *d* states (three t_g- and two e_g-like states) were occupied by one electron each, whereas in the case of Fe^{4+} one of the e_g states should be unoccupied. This scenario is indeed consistent with the electronic structure computed with SCAN for a representative partially delithiated LFMO system as shown in Figure 28, where spin-up unoccupied states are observed indicating the presence of well-localized electrons within the *d* states of Fe^{4+}. Yet, as previously evidenced by the Bader charge results (Figure 27-B), it can be seen from Figure 28 how PBE+U struggles to yield an adequate electronic structure representation of Fe ions. Specifically, spin-up unoccupied states are essentially not present in the DOS computed with PBE+U, suggesting that all iron ions are in $Fe^{3+/3.5+}$ mixed states and no Fe^{4+} species are present.

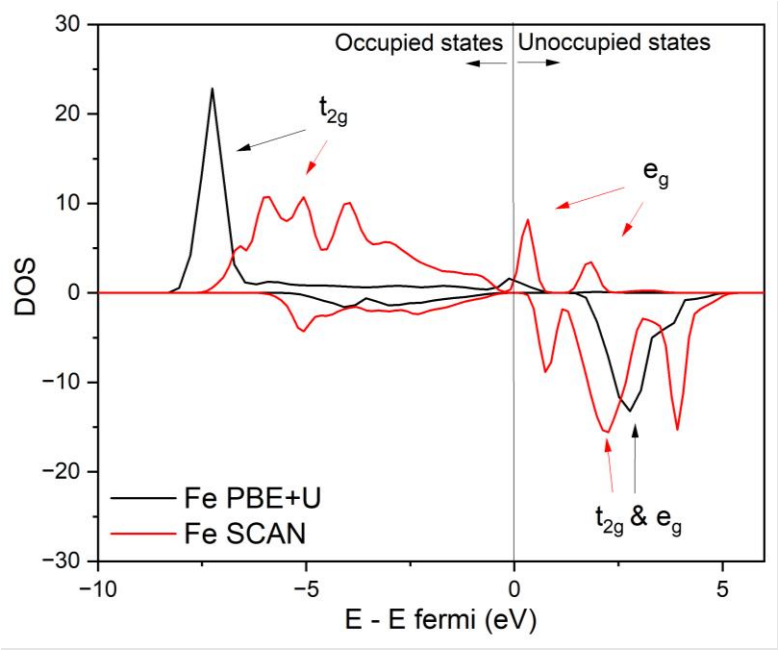

Figure 28: Computed Fe-projected DOS of the partially lithiated $Li_{0.25}Fe_{0.5}Mn_{0.5}O_4$ ground state considering Structure 4 (see Figure 22) using PBE (black) and SCAN (red).

Focusing now on oxygen redox activity, it is important to acknowledge the growing significance of accurately characterizing anionic redox processes, as they have the potential to enhance battery capacity, as explained in Chapter 1 (Section 1.4.2). In conjunction with Bader charge analysis, the computed projected DOS also offers interesting insights into the oxygen redox mechanisms in LFMO. Figure 29 highlights an essential observation: when employing the SCAN functional, the occupied states of O overlap with those of the transition metals within the -1.0 to 0.0 eV range, in particular with the spin-up Mn states. This suggests a reversible anionic redox process facilitated by the electronic interaction between the oxygen and the transition metal. This interaction should allow the efficient transfer of electrons between them, avoiding structural destabilization or oxygen loss through O_2 (gas) release. Essentially, the overlaping states can effectively facilitate the removal and insertion of oxygen electrons during the redox process, enabling the reversible interconversion of different oxidation states and providing additional capacity. Conversely, when using the PBE+U functional, the overlap between oxygen states and the metals just below the Fermi level, in the same energy range, appears to be less pronounced. This would suggest a weaker or less favorable electronic interaction between oxygen and the transition metal, rendering the anionic redox mechanism more irreversible[54,156]. It can be concluded that using different functionals for DOS calculations results in a different description of the anionic redox reversibility of the LFMO behavior. Thus, further experimental studies are needed to elucidate the anionic redox processes for oxygen in LFMO which falls beyond the scope of this work.

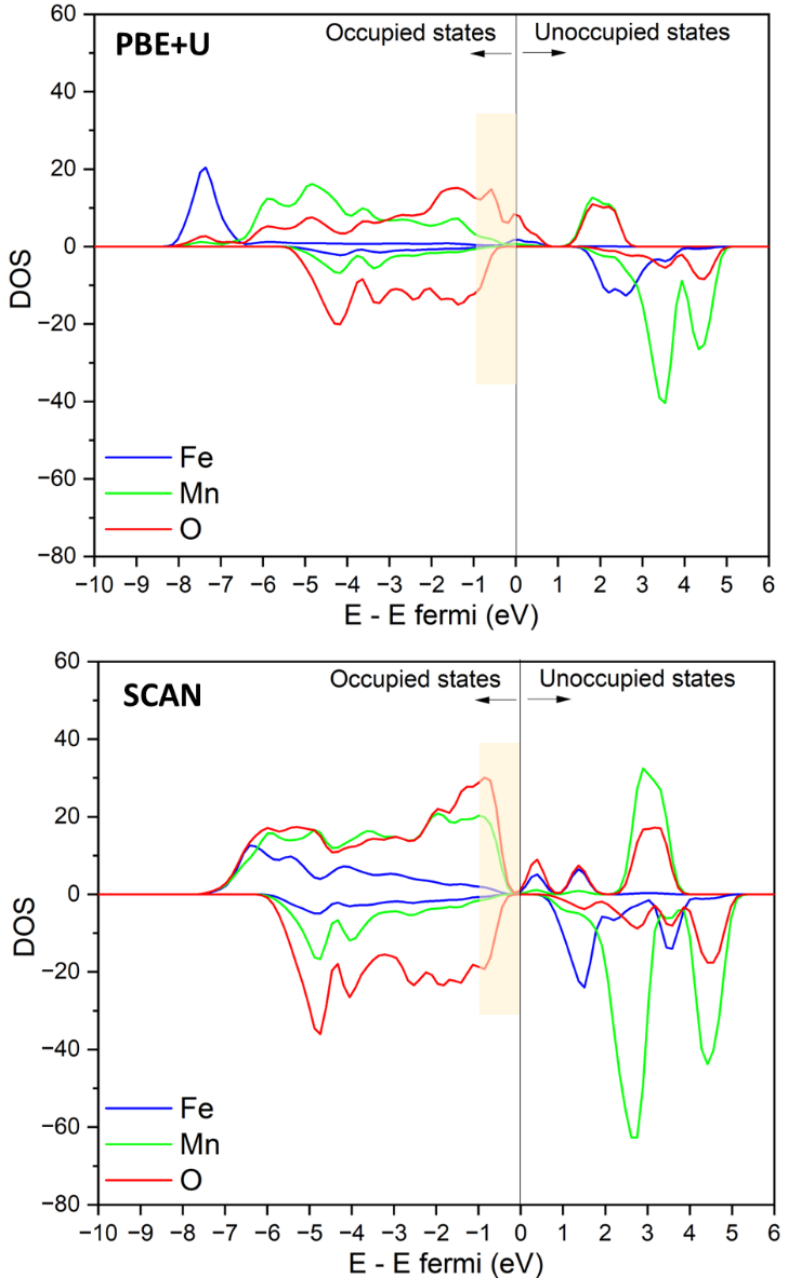

Figure 29: Projected DOS of the Fe0.5Mn0.5O4 for Fe, Mn and O calculated via PBE+U (up) and SCAN (down) for the Structure 4 model. The region of interest to understand the anionic redox interactions is highlighted in light yellow.

3.6. Conclusions

In this chapter a thorough examination of the electrochemical properties of the six most stable Fe/Mn distributions in the $LiFe_{0.5}Mn_{1.5}O_4$ composition has been conducted using DFT calculations with both PBE+U and SCAN functionals. Comparison of cell parameters and volumes showed that the SCAN functional exhibited better agreement with experimental data, with an average error of 0.15% compared to the experimental values. However, the PBE+U functional provided more accurate descriptions of the average voltages, yielding a value of 4.390±0.018V compared to the experimental 4.4V *vs* Li/Li^+. To examine the electrochemical features, the convex hulls for the six Fe/Mn distributions were computed using both PBE+U and SCAN. The phase stability upon (de)lithiation and the voltage behavior were found to be unaffected by the Fe/Mn distribution and the large amounts of ground states bear the convex hull suggested a preferred solid solution mechanism in this material. The voltage-composition curves obtained with PBE+U and SCAN functionals displayed a voltage window of 3.5-5.0V for PBE+U and 3.0-5.0V for SCAN, both showing two plateaus with a voltage jump at x = 0.5. Notably, the PBE+U functional demonstrated a better agreement with the experimental data.

The redox processes during (de)lithiation were studied through Bader charge calculations for various $Li_xFe_{0.5}Mn_{0.5}O_4$ compositions along the ground states of the convex hull. Both SCAN and PBE+U calculations revealed a transition from $Mn^{3+/4+}$ to Mn^{4+} as the proportion of Mn^{3+} gradually decreases from 33% in $Li_1Fe_{0.5}Mn_{0.5}O_4$ to around 0% in $Li_{0.5}Fe_{0.5}Mn_{0.5}O_4$. Additionally, the SCAN functional provided clearer identification of Fe Bader charges, indicating a redox transition from Fe^{3+} in $Li_{0.5}Fe_{0.5}Mn_{0.5}O_4$ to Fe^{4+} in $Fe_{0.5}Mn_{0.5}O_4$. These results are consistent with the experimental voltage curve, which displays a plateau associated with Fe redox at voltages around 5V *vs* Li/Li^+ and a plateau associated with Mn redox activity at voltages around 4V *vs* Li/Li^+. Moreover, both functionals also predicted an oxygen redox contribution to the electrochemical mechanism. DOS calculations were performed for different stages

of dethitiation, confirming that the SCAN functional more accurately captured Fe redox activity by revealing the coexistence of both Fe^{3+} and Fe^{4+} distinct species, while PBE+U only identified $Fe^{3+/3.5+}$ mixed states. Finally, the DOS analysis using the SCAN functional suggested that the anionic redox in LMFO to be reversible.

CHAPTER 4: Experimental study of LFMO. Interplay between synthesis parameters, microstructure, and electrochemistry

4.1. Abstract

In this chapter, the impact of synthetic parameters on the structural and electrochemical properties of $LiFe_{0.5}Mn_{1.5}O_4$ is investigated following a high throughput approach using the Batteryino-I module described in Chapter 2. Over 150 LFMO samples were synthesized under varying conditions, and structural characterization revealed distinct percentages of iron in tetrahedral positions, conforming antisite defects, whose amount was correlated with the synthetic parameters. The presence of antisite defects was associated with a structural expansion. Electrochemical studies demonstrated that samples with fewer antisite defects exhibited superior performance, with a longer Fe redox plateau, higher discharge capacity and capacity retention. This research highlights the significance of controlling defects to optimize LFMO's electrochemical behavior, providing valuable insights for developing high-performance battery materials and advancing energy storage technologies. The presented LFMO operates at voltages up to 5.1 V *vs.* Li/Li^+ delivering capacities up to $130 mAhg^{-1}$ at a 1D discharge rate with an average voltage of 4.4V. This represents an energy density up to 572 Wh/kg (and potentially able to deliver >660 Wh/kg). Such value would be superior to that of the commercial $LiNi_{0.6}Mn_{0.2}Co_{0.2}O_2$ (622NMC) (170 $mAh.g^{-1}$ discharge capacity at 4.3 V cut-off voltage and with

an average voltage of 3.8 V), in addition, LFMO results in a reduction of 66% of critical elements (Li, Ni, Co).

4.2. High throughput screening of synthetic parameters

The use of the Batteryino-I autonomous module, described in Chapter 2, allowed the screening of different synthesis conditions to better understand the synthetic process and the impact of the different parameters to the final material. The selected synthetic parameters that were screened are: annealing temperature, annealing time, cooling ramp, heating ramp, gel formation time, position in the automated module, position in the furnace and Li excess added at the beginning of the synthesis. The values sampled for each variable are described in Table 11 and a table, indicating the synthetic parameters for each sample, can be found in Annex III. Overall c.a. 150 samples have been synthesized. The synthesis of part of these samples also contributed to the optimization of the Batteryino-I module, and therefore many of the samples that were initially prepared shared the same synthetic conditions until reproducibility was achieved. Finally, c.a. 70 samples have been used to establish composition-structure-synthesis correlations.

Once the reproducibility of the set-up was ensured, the set of synthetic parameters selected for each batch of new samples was generated by the random.uniform module of python[157], which generates pseudo-random sets of conditions taking into account the given values described in Table 11.

Synthetic parameters	Tested values
Position	A1-4, B1-4, C1-4
Li excess per f.u.	0.02, 0.04, 0.06, 0.08
Gel formation time (h)	3, 3.5, 4, 4.5, 5, 5.5
Temperature heating ramp (°C/min)	1, 2.5, 5
Annealing Temperature (°C)	750, 800, 850, 900
Annealing time (h)	5, 7.5, 10
Temperature cooling ramp (°C/min)	2, 5 or quenching

Table 11: Synthetic parameters screened for the LFMO system.

After the synthesis, the samples were measured by X-ray diffraction to analyze the structures of the synthesized materials. The XRD measurements were followed by pseudo-Rietveld refinements against the *Fd*-3*m* space group starting from the lattice parameters of the corresponding LFMO phase ICSD 187271. Pseudo-Rietveld refinements (*i.e.,* Rietveld refinements with fixed atomic parameters) were found to be a good compromise between invested time and accuracy of the data for a preliminary evaluation of the large amount of patterns. The background was introduced in the refinements using the automatic background tool of WinPLOTR.[135] Selected samples were later Rietveld-refined (see section 4.3.2).

From this analysis it was concluded that the $LiMn_{1.5}Fe_{0.5}O_4$ spinel was obtained in all cases, although with different structural properties and amounts of impurities. Quenched samples, and samples synthesized at the maximum selected temperature (900°C) with no Li excess were impure, which is indicative of lithium evaporation at high temperatures.

On the other hand, the pure samples exhibited a large variability in the value of the cell parameter, ranging between 8.24 and 8.31 Å, which indicates compositional or structural differences. The samples also differed in the intensity of certain reflections, in particular (220) reflection, as will be discussed in section 4.3.2. However, the XRD patterns of these samples were similar in terms of peak broadening, indicating similar crystallinity and probably similar crystallite morphology. In the following section the detailed characterization of selected samples is presented.

4.3. Structural and morphological characterization of selected samples

Three samples were selected according to their cell parameter for a thorough structural and morphological characterization. These samples are labeled as Lcp-357 (a=8.244(2)Å), Mcp-134 (a=8.266(15)Å) and Hcp-158 (a=8.294(12)Å) where Lcp means low cell parameter, Mcp medium cell parameter and Hcp high cell parameter. The conditions used for the synthesis of the selected samples are described in Table 12. Mcp-134 and Hcp-158 apparently

share similar synthetic conditions and result in different cell parameters. This is due to the fact that they were prepared before all synthetic variables were successfully controlled and thus, in reality, they do not share exactly the same synthetic conditions (i.e., gel formation time, cooling ramp, ventilation, thermal stability in the heating plate, See Section 2.4.).

	Lcp-357	Mcp-134	Hcp-158
Position	B2	A1	A1
Li excess (f.u.)	0.02	0.02	0.02
Gel formation time (h)	4	NR	NR
Heating ramp temperature (°C/min)	5	5	5
Annealing temperatura (°C)	700	900	900
Annealing time (h)	10	10	10
Cooling ramp temperature (°C/min)	5	NR	NR
Cell parameter (Å)	8.244(2)	8.266(15)	8.294(12)

Table 12: Synthetic parameters of the selected samples for the structural and morphological study. NR stands for not registered.

4.3.1. Scanning electron spectroscopy

Scanning Electron Spectroscopy (SEM) images corresponding to the selected samples, Mcp-134 and Hcp-158, are shown in Figure 30. The morphology of the two samples is very similar with agglomerates of primary particles with a size of 5-30 μm, see Figure 30-a and b. The primary particles, whose size ranges between 1 and 4 μm are overall isotropic as can be seen in Figure 30-c and d. Such morphology is representative of all the samples prepared in this chapter, from which it can be concluded that the morphology of the different samples does not vary within the range of the synthetic parameters explored.

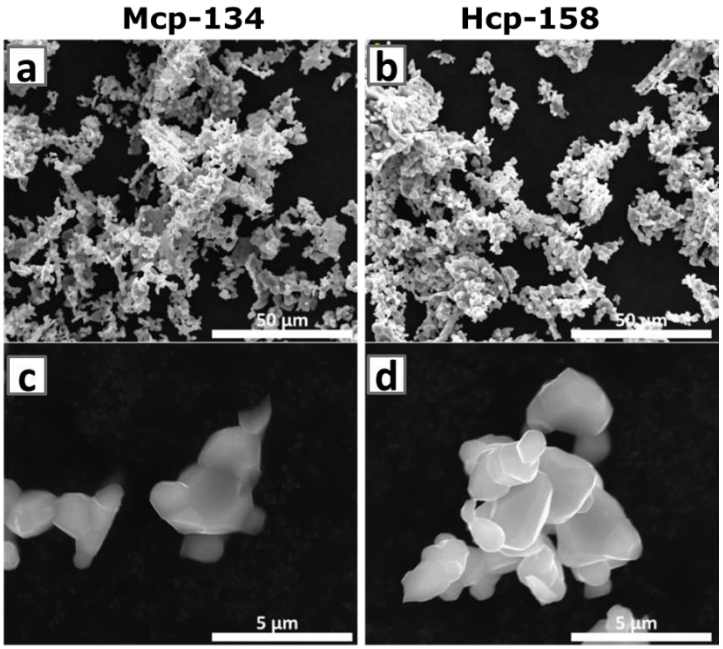

Figure 30: SEM images for two different samples of LFMO with lower, Mcp-134, (a, c) and higher, Hcp-158, (b, d) cell parameters at 50µm (a, b) and 5µm (c, d) scale.

4.3.2. X-ray diffraction

As mentioned before, besides the cell parameter, differences were also observed regarding the intensity of the (220) reflection, which becomes more intense as the cell parameter increases. The Rietveld refined XRD patterns of the selected samples can be found in Figure 31, and will be further discussed later in this Section.

In spinel structures, transition metals typically occupy octahedral 16*d* sites, Li atoms occupy 8*a* tetrahedral sites and oxygen atoms lie in 32*e* sites of the *Fd*-3*m* space group. As shown in chapter 3, the phase stability of different Fe and Mn distributions is comparable, so it is considered that the structure exhibits Fe and Mn disorder. In ideal LFMO, the (220) reflection has no intensity. However, it has been shown by other authors that this peak appears when Fe occupies the lithium 8*a* sites in the *Fd*-3*m* space group.[89,95,158] This type of defect (considering that lithium and iron

atoms exchange positions *i.e.* antisite defect) is illustrated in Figure 32.

Table 13 indicates the Shannon ionic radius for the different possible lithium and iron environments in the LFMO structure. Interestingly, the ionic radius of lithium in octahedral environment is larger than that of Fe atoms, which would explain the structural expansion observed in the samples with antisite defects.

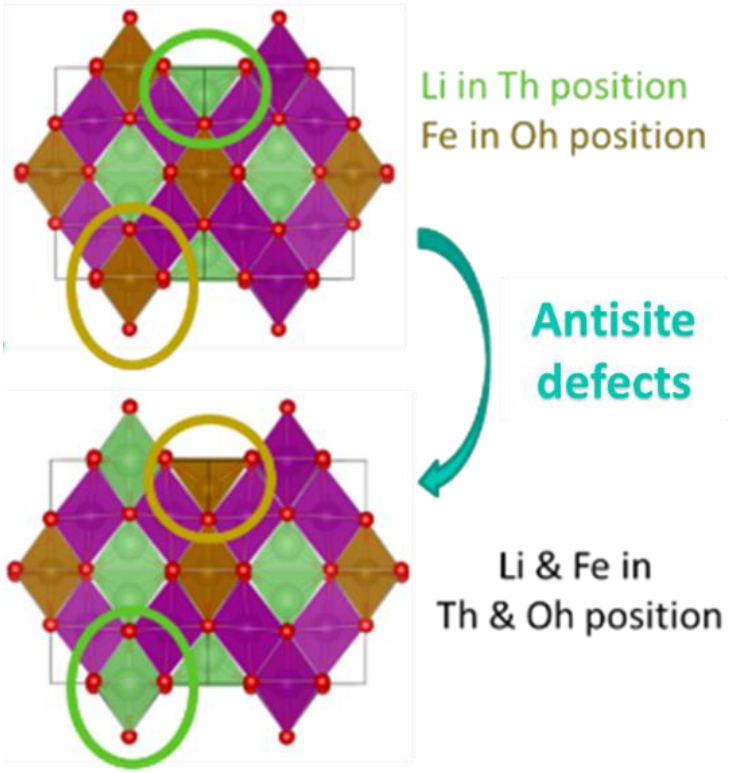

Figure 32: Representation of the structures of LFMOs with no antisite defects (above) and with the exchange in the Li/Fe atoms corresponding to antisite defects (below).

Ion	Coordination	Ionic radius (Å)
Li^{+}	4	0.59
Li^{+}	6	0.76
Fe^{3+}	4	0.49
Fe^{3+}	6	0.645

Table 13: Shannon ionic radii for Fe and Li[159]. Note that it has been considered that Fe^{3+} ions are high spin in LFMO.[86,160]

The hypothesis of the presence of antisite defects was validated by the Rietveld refinement of the samples. Different structural models were considered, through the use of different constrains (*i.e.,* Li/Fe antisite, Fe in tetrahedral and octahedral sites with no Li in octahedral positions, Fe occupancy constrained to 0.5 or not constrained). The antisite model was found to be the one leading to the best fits of the experimental patterns. This model considers the general formula $[Li_{1-x}Fe_x]_{8a}[Li_xFe_{0.5-x}Mn_{1.5}]_{16d}O_4$ where Fe and Li exist in both tetrahedral and octahedral positions corresponding to a strict antisite defect. The occupancies were refined taking into account that the sum of Li and Fe in tetrahedral sites must be 1 and their sum in octahedral sites 0.5. The Biso parameters were independently refined for each site. In all cases, the atomic position of oxygen was refined and resulted to be around x=0.26 for the three samples. The results of the refinements can be seen in Figure 33, Table 14 and Table 15. The percentage of Fe in 8*a* sites, and thus the quantity of antisite defects, was calculated considering the Fe_{8a} occupancy with respect to the total amount of iron and resulted to be 6(4)%, 15(4)% and 27(3)% for samples Lcp-357, Mcp-134, and Hcp-158 respectively, and thus confirming a direct correlation with the cell parameter.

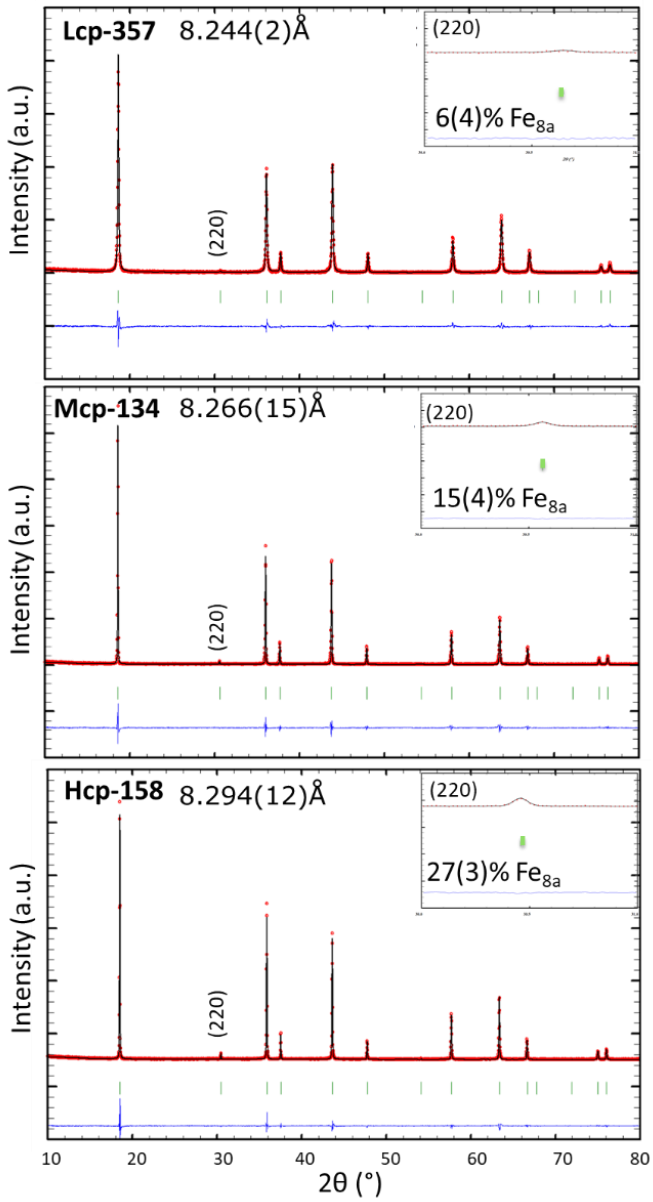

Figure 33: Rietveld refinements corresponding to $[Li_{1-x}Fe_x]_{8a}[Li_xFe_{0.5-x}Mn_{1.5}]_{16d}O_4$, for samples Lcp-357, Mcp-134 and Hcp-158 with cell parameters of 8.244(2)Å, 8.266(15)Å and 8.294(12)Å, respectively. In the upper-right part of each refinement the enlargement of the (220) diffraction peak related to the quantity of Fe occupying tetrahedral position can be observed. In green the Bragg positions, in black the calculated XRD pattern, in red the observed patterns are represented and, in blue the difference between observed and calculated is shown.

	Lcp-357	Mcp-134	Hcp-158
Cell par. *a/b/c* (Å)	**8.244(2)**	**8.266(15)**	**8.294(12)**
Volume (Å³)	560.3(3)	564.9(18)	570.6(15)
Rp	14.9	17.5	14.6
Rwp	22.1	21.7	18.1
Rexp	14.96	11.83	11.73
RBragg	2.62	4.49	3.7
Rf	3.56	3.81	4.83
χ^2 (Bragg)	2.19	3.38	2.38

Table 14: Unit cell parameters and conventional Rietveld factors for the XRD Rietveld refinements of the selected LFMO selected samples.

	Lcp-357		Mcp-134		Hcp-158	
	Biso	**Occupancy**	**Biso**	**Occupancy**	**Biso**	**Occupancy**
Li_{8a}	**3(3)**	0.96(2)	**3(2)**	0.92(2)	**1(1)**	0.86(1)
Fe_{8a}	**3(3)**	0.03(2)	**3(2)**	0.07(2)	**1(1)**	0.13(1)
Li_{16d}	**0.2(1)**	0.03(2)	**0.5(1)**	0.07(2)	**0.6(1)**	0.13(1)
Fe_{16d}	**0.2(1)**	0.46(2)	**0.5(1)**	0.42(2)	**0.6(1)**	0.36(1)
Mn_{16d}	**0.2(1)**	1.5	**0.5(1)**	1.5	**0.6(1)**	1.5
O_{32e}	**0.2(3)**	4	**1.1(3)**	4	**1.8(3)**	4
$O_{x/y/z}$	0.260(9)		0.262(1)		0.261(8)	

Table 15: Rietveld refinement results of atom occupancies, Biso parameters and atomic position of oxygen for the LFMO selected samples

4.3.3. Combined X-ray and neutron powder diffraction study

In order to validate the cation distribution and the lithium environment, Neutron Powder Diffraction (NPD) measurements were performed, followed by combined XRD-NPD Rietveld refinements against the cubic spinel structure of Lcp-357 and Hcp-158 using the FullProf Suite[133,134]. Again, the antisite model corresponding to $[Li_{1-x}Fe_x]_{8a}[Li_xFe_{0.5-x}Mn_{1.5}]_{16d}O_4$ was found to be the one leading to the best fit of the experimental patterns as for the single XRD refinements.

Due to the lower signal-to-noise ratio of the NPD diffractograms the combined XRD-NPD refinements were performed in a 70:30 weight ratio. The overall isotropic displacement factor, Bov, was refined

since it was difficult to assign the Biso parameter to each site due to the quality of the NPD data. In both cases, the atomic position of oxygen was refined and resulted to be around x=0.26 for both samples at the 32*e* sites in the space group of *Fd*-3*m*. The results of the refinements can be seen in Figure 34, Table 16 and Table 17. The percentage of antisite defects resulted in 4(2)% and 24(2)% for samples Lcp-357 and Hcp-158 respectively, which is in agreement with the 6(4)% and 27(3)% that resulted from the single XRD Rietveld refinements. NPD allowed to confirm that Li can be found in 16*d* positions. The differences in the results obtained with different techniques are discussed in Section 4.3.6.

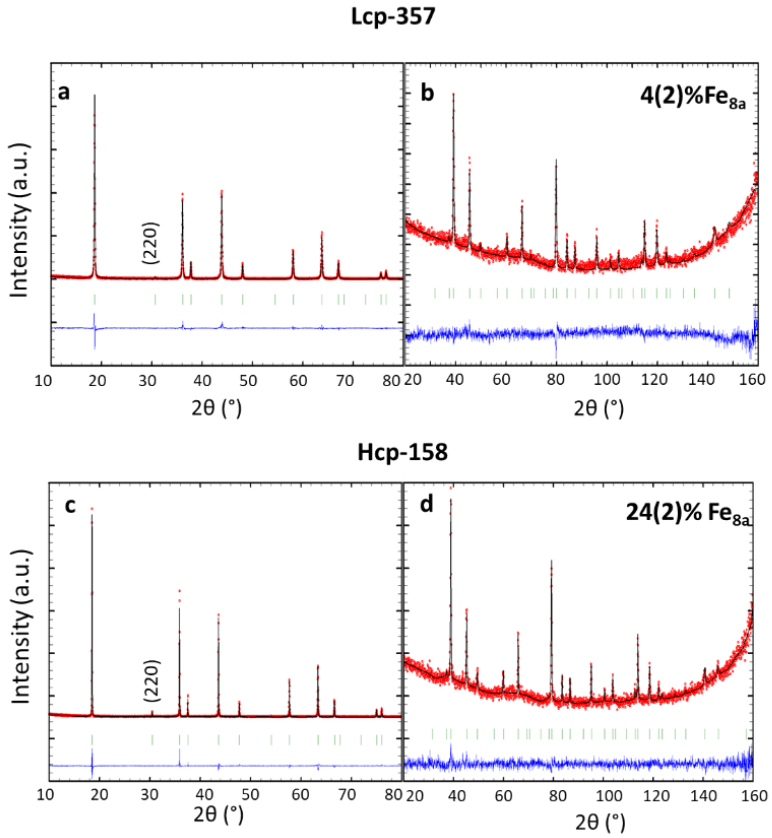

Figure 34: Combined XRD-NPD Rietveld refinements for samples Lcp-357 (a, b) and Hcp-158 (c, d). The percentage of antisite defects are written for each sample. In green the Bragg positions, in black the calculated XRD patterns, in red the observed patterns are represented and, in blue the difference between observed and calculated patterns are shown.

	XRD	
	Lcp-357	**Hcp-158**
Cell par. *a/b/c* (Å)	8.245(15)	8.294(15)
Volume (Å³)	560.5(18)	570.6(15)
Rp	15.7	15.3
Rwp	22.6	18.5
Rexp	14.97	11.75
RBragg	8.62	7.52
Rf	5.85	6.13
χ^2 (Bragg)	2.29	2.48
	NPD	
	Lcp-357	**Hcp-158**
Cell par. *a/b/c* (Å)	8.240(3)	8.291(9)
Volume (Å³)	559.5(7)	570.(1)
Rp	97.8	114
Rwp	45.9	38.3
Rexp	36.71	36.41
RBragg	40.4	12.7
Rf	32.5	10.5
χ^2 (Bragg)	1.56	1.11

Table 16: Unit cell parameters and conventional Rietveld factors for the XRD (above) and NPD (below) combined Rietveld refinements of the LFMO selected samples.

	XRD-NPD			
	Lcp-357		**Hcp-158**	
	Biso	**Occupancy**	**Biso**	**Occupancy**
Li_{8a}	1.44491	0.97(1)	1.44491	0.87(1)
Fe_{8a}	1.44491	0.02(1)	1.44491	0.12(1)
Li_{16d}	0.44216	0.02(1)	0.44216	0.12(1)
Fe_{16d}	0.44216	0.47(1)	0.44216	0.37(1)
Mn_{16d}	0.44216	1.5	0.44216	1.5
O_{32e}	0.80536	4	0.80536	4
Bov XRD	-0.4(1)		0.1(17)	
Bov NPD	-0.1(3)		0.4(3)	
O *x/y/z*	0.261(9)		0.262(6)	

Table 17: Rietveld refinement results of atom occupancies and biso parameters of the XRD-NPD combined refinements for the LFMO selected samples.

4.3.4. Mössbauer spectroscopy

^{57}Fe Mössbauer spectroscopy can help to identify different iron environments and iron oxidation states, being very useful to quantify the percentage of defects in this case. Two of the previously characterized samples, Mcp-134 and Hcp-158, have been analyzed by Mössbauer. The samples were fitted with two doublet peaks and, considering the IS parameter, the oxidation states of iron in both cases corresponded to Fe^{3+}. Table 18 shows the values of the isomer shift (IS), quadrupole splitting (QS), line width (WID) and iron percentage (%Fe) corresponding to each component. The doublets with highest IS, 0.34 mm/s, were assigned to Fe in octahedral position (Figure 35, green line) and the doublets with the smallest isomer shifts, 0.22 and 0.21 mm/s, were assigned to Fe in tetrahedral position (Figure 35, blue line) for both samples as referred in bibliography[86,161]. The percentage of each kind of iron is calculated by the ratio between the area of both doublets.

Thus, Mössbauer spectroscopy confirmed that there is Fe in octahedral and tetrahedral positions in different proportions depending on the synthetic parameters and that Fe is in oxidation state 3+. In sample Hcp-158, the quantity of Fe found in tetrahedral positions was 26(3)%, while for sample Mcp-134 the quantity of Fe found in tetrahedral positions was 9(3)% (Table 18). The comparison between the results of the different techniques will be discussed in Section 4.3.6.

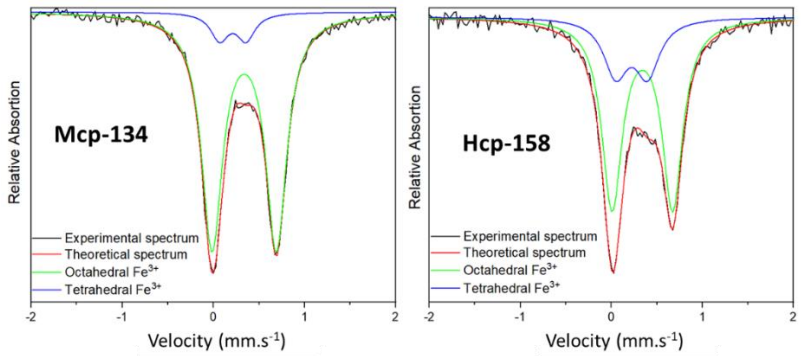

Figure 35: ^{57}Fe Mössbauer spectra fits of Mcp-134 and Hcp-158 samples measured at room temperature, both collected at 3 mm/s velocity. The reference used for the IS was α-Fe at room temperature.

	Fe (16*d* Octa)				Fe (8*a* Tetra)			
Sample	**IS mm.s^{-1}**	**QS mm.s^{-1}**	**WID mm.s^{-1}**	**Fe %**	**IS mm.s^{-1}**	**QS mm.s^{-1}**	**WID mm.s^{-1}**	**Fe %**
Mcp-134	0.34	0.71	0.28	**91(3)**	0.21	0.29	0.24	**9(3)**
Hcp-158	0.34	0.66	0.27	**74(3)**	0.22	0.35	0.32	**26(3)**

Table 18: ^{57}Fe Mössbauer spectra fitting values at room temperature of Mcp-134 and Hcp-158 samples. Reference is α-Fe at room temperature. Mössbauer values for the fitted spectra, isomer shift (IS), quadrupole splitting (QS), line width (WID) and iron percentage (%Fe).

4.3.5. X-ray absorption spectroscopy

The two LFMO samples were also analyzed via dual-edge **X-ray absorption spectroscopy (XAS)** on both TM edges to extract information on the oxidation states of both Mn and Fe and on the local structure around the absorbing atom. The **X-ray absorption near edge spectra (XANES),** depicted in Figure 36 for Mn (left) and Fe K-edge (right) respectively, indicate that the two samples have distinct Mn oxidation state but similar iron oxidation state. In fact, sample Mcp-134 Mn k-edge is shifted to higher energy compared to Hcp-158, which reflects a higher average oxidation state of the absorbing Mn. With the help of metal reference fingerprint, the approximate oxidation state can be estimated. However, in the case of Mn both samples have an oxidation state in the range between 3.4 and 3.6, respectively, while in the case of Fe the oxidation state is in vicinity of Fe^{3+} which is in accordance with the Mössbauer results. Another noteworthy observation is the increased Fe K-edge pre-edge feature of the Hcp-158 as compared to Mcp-134. The increase of a dipole forbidden transition hints a larger share of tetrahedrally coordinated iron as a result of a larger overlap of *p* and *d* orbitals in such non-centrosymmetric coordination.

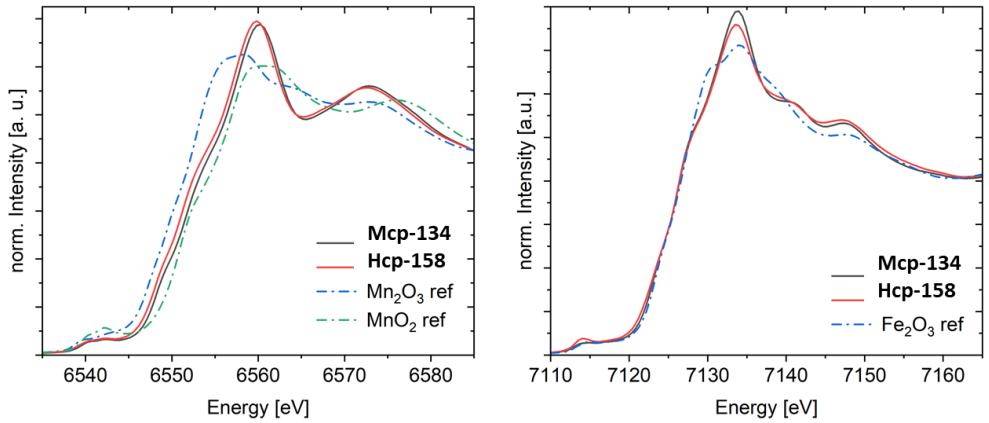

Figure 36: Comparison of the Mn K-edge (left) and Fe K-edge (right) of XANES spectra of Mcp-134 and Hcp-158 along with the reference spectra of relevant metal oxides, MnO_2 (Mn^{4+}), Mn_2O_3 (Mn^{3+}) and Fe_2O_3 (Fe^{3+}) (dash dotted lines).

The analysis of the **extended X-ray absorption fine structure (EXAFS)** of the two samples allows to gain insights on the local structure around the absorbing atom. In both samples the Fourier transform of Fe K-edge EXAFS spectra are dominated by two features, see Figure 37, which can be attributed to Fe--O and Fe--TM shells, respectively. It is salient that while both shells are at similar distance (R) from absorbing atom in both LFMO samples, their intensities are damped and broadened in the case of Hcp-158. This is reflected in a higher Debye Waller (ss) factor in the EXAFS fitting, see Table 19. An elevated Debye Waller factor indicates a greater local disorder which could be the result of a broader distribution of bond lengths due to the coexistence of different Fe coordination for sample Hcp-158 because of antisite defects.

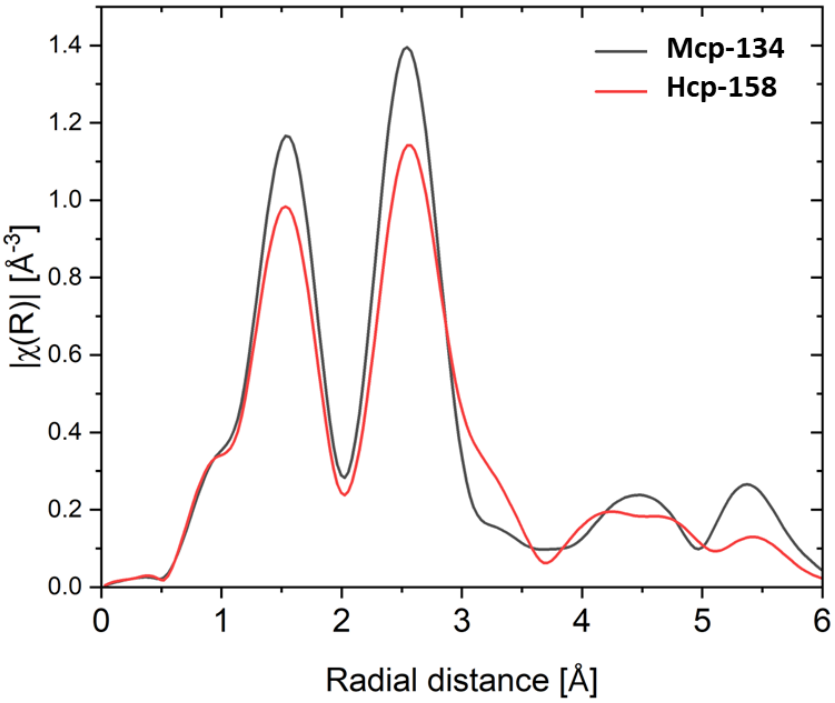

Figure 37: Fourier transform of the Fe K-edge EXAFS plots of Mcp-134 vs Hcp-158.

	Mcp-134		**Hcp-158**	
	R (Å)	**ss (Å²)**	**R (Å)**	**ss (Å²)**
Fe-O1	2.008(5)	0.0071(4)	1.99(1)	0.0094(9)
Fe-TM	2.956(5)	0.0068(3)	2.91(7)	0.0085(6)
Fe-O2	3.93(3)	0.011(5)	3.62(3)	0.003(4)

Table 19: Fe K-edge EXAFS fitting parameters of the two LFMO samples. The amplitude reduction factor was fixed at 0.95 and Enot at -0.4, coordination number was kept at 6. R indicates the radial distance and ss the Debye Waller factor that measures the disorder.

A tentative estimation of the approximate number of ligands for the first shell (Fe—O) revealed that, in Mcp-134, Fe is coordinated by approximately 5.6 oxygen, while, in Hcp-158, it is coordinated only by 4.8. This supports the hypothesis that an increased share of

tetravalent coordinated Fe is present in the Hcp-158 sample in agreement with the previous results of diffraction and Mössbauer.

4.3.6. Discussion

As it has been shown by means of XRD, NPD and Mössbauer spectroscopy the selected samples crystallize with antisite defects, although differ the percentage of iron located in tetrahedral position. The increasing amount of antisite defects correlates with a larger cell parameter. This hypothesis was also supported by the XAS results. Slight differences in the quantification of such defects have been found between techniques, as shown in Table 20. The XRD and the combined XRD-NPD results show a good agreement in the quantification while, when compared with Mössbauer spectroscopy, a higher difference in the percentage of defects is observed for sample Mcp-134. This can be attributed to the very small intensity of the (220) diffraction peak and/or to the low quality of the NPD patterns, which exhibit a low signal-to-noise ratio. However, all values are in accordance when considering their standard deviations.

	XRD	XRD	XRD-NPD	Mössbauer
	Cell parameters (Å)	Fe_{8a} (%)		
Lcp-357	8.244(2)	6(4)	4(2)	-
Mcp-134	8.266(15)	15(4)	-	9(3)
Hcp-158	8.294(12)	27(3)	24(2)	26(3)

Table 20: Comparison on the resulting percentage of iron in tetrahedral position with the different characterization techniques.

The structure that has demonstrated to unify all the results is the strict definition of the antisite defect, $[Li_{1-x}Fe_x]_{8a}[Li_xFe_{0.5-x}Mn_{1.5}]_{16d}O_4$, where Fe and Li exist in both tetrahedral and octahedral positions maintaining their stoichiometry, and Fe is in the oxidation state +3, confirming the initial hypothesis. Once the structural definition and the correlation between cell parameters and percentages of iron in tetrahedral sites was clarified, it is of interest to analyze the impact of these defects on the electrochemical performance. For this evaluation, the percentage of antisite defects considered will be the ones extracted from the XRD Rietveld refinements as it is a trustable technique, and, at the same

time, it is easier to access compared with NPD or Mössbauer spectroscopy. Before the deep study of the electrochemical performances a study of the correlations between structure and synthetic parameters is presented.

4.4. Correlations between synthetic parameters and structure

Herein, the correlation between the **intensity of the (220) reflection** and the cell parameter was confirmed for the rest of synthesized samples as shown in Figure 38, where the area of the (220) diffraction peak is plotted as a function of the cell parameter. The area of this peak was automatically measured using a python routine. The selected synthesis conditions described in Section 4.2. (Table 11) allowed obtaining a set of samples with a large variability of antisite defects. In this section, the individual impact of each synthetic variable in the final structure will be discussed.

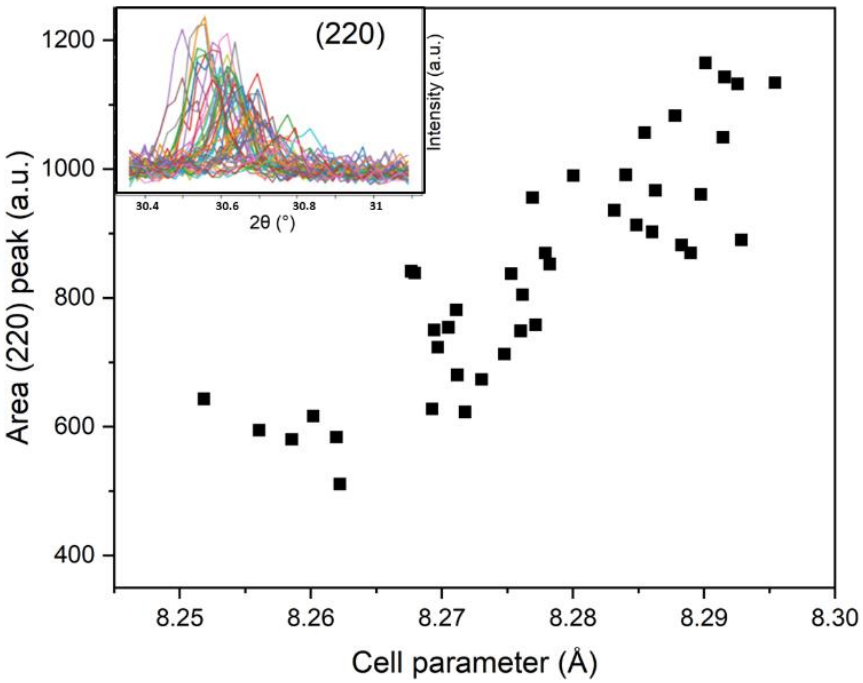

Figure 38: Correlation between the area of the (220) diffraction peak of the F-3dm unit cell and the cell parameters for the synthesized samples. The diffraction peak (220) for the different samples is shown in the upper left part.

In Figure 39-a-d, cell parameters of the LFMO main phase are plotted with respect to different synthetic variables. Figure 39-a shows the correlation with **annealing temperature**. It can be observed that, overall, the cell parameter increases with the annealing temperature. However, a high variation is also observed for samples prepared with the same annealing temperature because other parameters such as Li excess (represented in different colors) also contribute. Overall, for a same annealing temperature, the cell parameters were higher when a lower amount of Li was added (Figure 39-a). This is confirmed in Figure 39-b, which shows the evolution of the cell parameter with the **Li excess** at a fixed temperature (750ºC). This can be correlated to Li evaporation during the annealing at higher temperatures[162,163], which would favor having a larger amount of Fe in tetrahedral positions.

The correlations observed for the different **annealing times** in Figure 39-c match with the correlation described for the annealing temperature, higher temperatures give higher cell parameters. However, since longer annealing times were employed for higher temperature, further sampling would be needed to understand if a correlation between annealing time and cell parameter exists.

Figure 39-d shows the cell parameter obtained for different **gel formation times** for samples for which the rest of parameters were fixed. The results indicate that the gel formation time does not affect the final structure of the material as only variations in the third decimal of the cell parameter are observed for samples prepared using the same amount of excess Li.

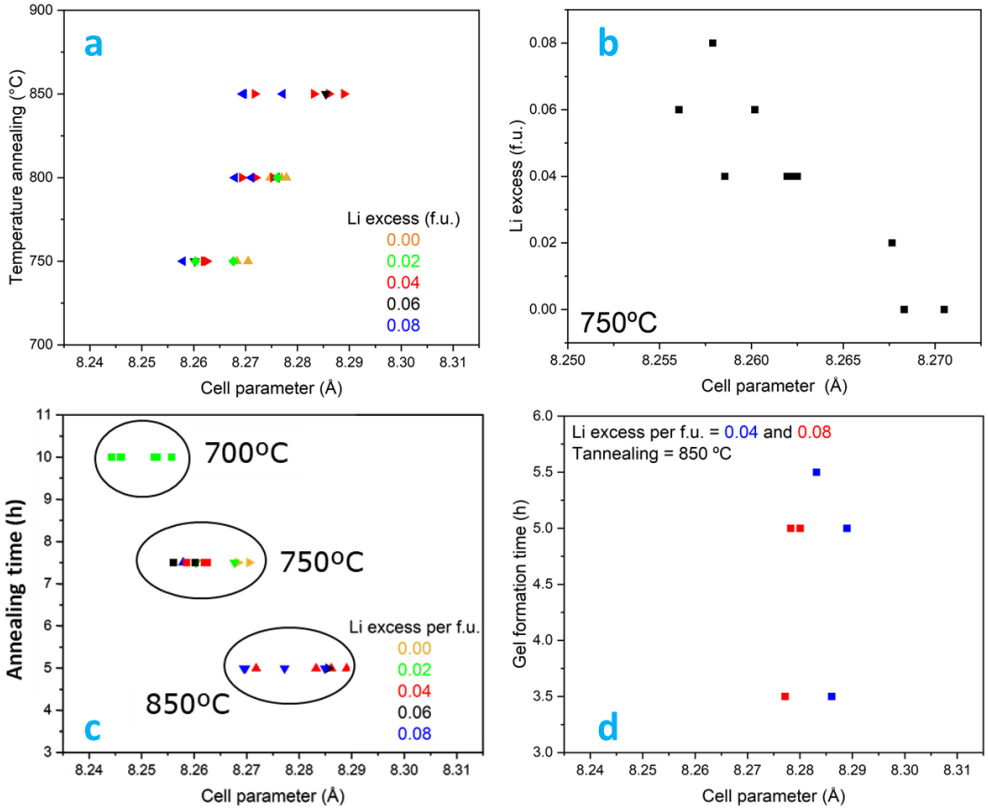

Figure 39: Correlations between cell parameters of the pure LFMO synthesized set of samples and A) the annealing temperature and Li excess added at the beginning of the synthesis, B) the Li excess for a fix annealing temperature of 750ºC, C) the annealing time and the Li excess at different annealing temperatures, D) the gel formation times for different Li excess at 850ºC. It can be highlighted that the error bars are included in this graphic, but they are so small that cannot be distinguished.

Finally, for the **cooling and heating ramps** important changes were not expected nor found. Although it is important to remember that quenched samples were impure.

4.5. Electrochemical characterization of LFMO samples

Structural defects have shown to have an impact on the electrochemical performance of cathode materials such as LFP or layered oxides like NMC and NCA.[164] To study how the antisite defects affect the electrochemical behavior of LFMO, different

experiments have been performed. Five different samples, with different cell parameters ranging from 8.257(3) to 8.304(2)Å, and thus different quantity of antisite defects, have been selected for this purpose. The synthetic conditions and structural characteristics of these five samples are described in Table 21 indicating the percentage of antisite defects of each sample determined form Rietveld refinements of the XRD patterns. The percentage of defects was calculated considering $[Li_{1-x}Fe_x]_{8a}[Li_xFe_{0.5-x}Mn_{1.5}]_{16d}O_4$ composition in the Rietveld refinements. Owing to sample availability issues, from the samples characterized in Section 4.3, only Mcp-134 could be used for the electrochemical characterization, however a good correlation between cell parameter and $\%Fe_{8a}$ is also obtained for this set of samples as depicted in Figure 40.

	LFMO-290	Mcp-134	LFMO-325	LFMO-323	LFMO-234
Position	C1	A1	B1	A3	A1
Li excess per f.u.	0.08	0.02	0.02	0.02	0.02
Gel formation time (h)	3.5	NR	3	3	4.5
Heating ramp temperature (°C/min)	2.5	5	5	5	5
Annealing Temperature (°C)	750	900	800	800	900
Annealing time (h)	7.5	10	10	10	10
Temperature cooling ramp (°C/min)	2	NR	5	5	5
Cell parameter (Å)	8.257(3)	8.265(15)	8.281(2)	8.290(2)	8.304(2)
Antisite defects (%)	14(4)	15(4)	22(5)	26(2)	35(5)

Table 21: Synthetic and structural characteristics of the five selected samples for the electrochemical study. In blue the percentage of antisite defects, calculated from the Rietveld refinements of XRD data, is highlighted. NR means Not Recorded.

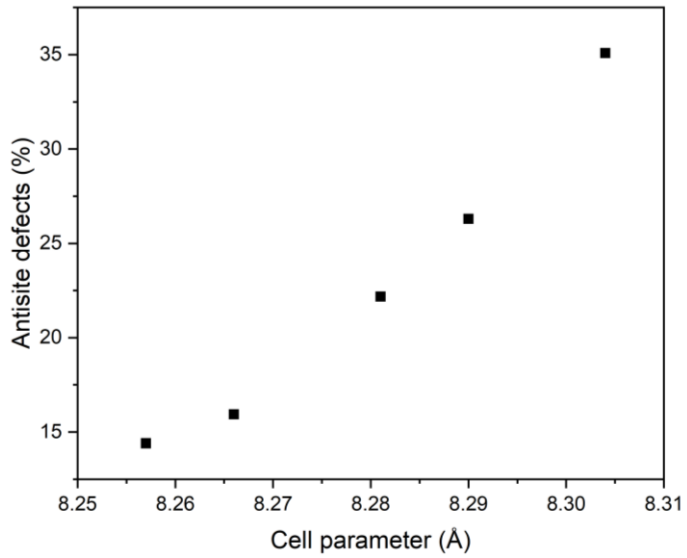

Figure 40: Correlation between cell parameter and antisite defects for the selected samples. It can be highlighted that the error bars are included in this graphic, but they are so small that they cannot be distinguished.

The selected materials were cycled *vs.* Li/Li^+ at a C-rate of C/10 in a voltage window from 3 to 5V *vs.* Li/Li^+ using 1M $LiBF_4$ in EC:DMC (3:7 by wt.) as electrolyte and assembled in EL PAT-type cells in half-cell configuration. $LiBF_4$-based electrolytes offer promising advantages in terms of thermal stability, passivation, cycling performance, and water tolerance in comparison with other electrolytes, such as $LiPF_6$-based ones. Indeed, it has been proved that using $LiBF_4$ salt the amount of HF produced during cycling is reduced leading to less Mn dissolution[165]. The electrode formulation and preparation are described in Chapter 6 (Section 6.2.2.).

Figure 41 presents the voltage-capacity curves of the galvanostatic cycling and their corresponding dQ/dV plots for the 1st (Figure 41-a,b) and the 10th cycles (Figure 41-c, d) for the selected materials. As expected from previous reports, the voltage curves exhibit two pseudo-plateaus; a first pseudo-plateau close to 4V *vs.* Li/Li^+, usually attributed in the literature to the $Mn^{3+/4+}$ redox activity, and a second one close to 5V *vs.* Li/Li^+, attributed to the $Fe^{3+/4+}$ redox activity[75,95,161]. As also shown in Table 22 a very clear correlation is

obtained between the amount of antisite defects and both the discharge capacity and the total average voltage for the discharge (obtained by measuring the area below the experimental curve). Antisite defects are thus found to be detrimental for the electrochemical properties of LFMO, as the electrochemical performance changes from a discharge capacity of 102.47mAhg^{-1} and an average voltage of 4.28V (14(4)% of defects, LFMO-290) to 66.56mAhg^{-1} and 4.12V (35(5)% of defects, LFMO-234).

In Figure 41-b it can be observed that the $Mn^{3+/4+}$ plateau involves in fact two processes, covering a broad voltage range, although for the samples with smaller cell parameter the redox peak becomes more symmetric in the 10th cycle. To understand better these processes further mechanistic studies, such as Potentiostatic Intermittent Titration Technique (PITT) experiments, or in operando XRD would be needed.

In Figure 41-b and d it can be observed that the iron redox processes are not finished at 5.0V as the dQ/dV curves intensity is still increasing when the cut-off is reached. This fact indicates that the electrochemical performance could be improved by increasing the voltage window.

In order to obtain further insight in the different redox processes, the discharge capacities related to each pseudo-plateau have been separated by considering 4.5V as lower voltage limit for the $Fe^{3+/4+}$ and as maximum voltage limit for the $Mn^{3+/4+}$ redox pseudo-plateaus. Figure 42 depicts the discharge capacities and the average voltages of the overall curves for the 1st discharge curve (Figure 41-a) of each pseudo-plateau *vs.* the quantity of defects found in each sample. Both Mn and Fe discharge capacities and average voltages showed to be affected by the percentage of antisite defects. For Fe, the higher the quantity of antisite defects, the lower the capacities are; and, in the case of Mn, although the sample with lower quantity of defects presents a slightly smaller discharge capacity, the same trend is observed. With respect to the average voltage of the overall curve, both transition metals exhibit the same tendency, the higher the quantity of antisite defects, the lower the average voltage of the overall curves. This suggests not only that the Fe in tetrahedral

position is not electrochemically active, but also that it introduces an environment in which the mobility of lithium for its extraction and insertion into the structure is hindered and also hampers the redox activity of Mn during cycling. Moreover, this trend is maintained after 10 cycles as it can be seen in Figure 41-c.

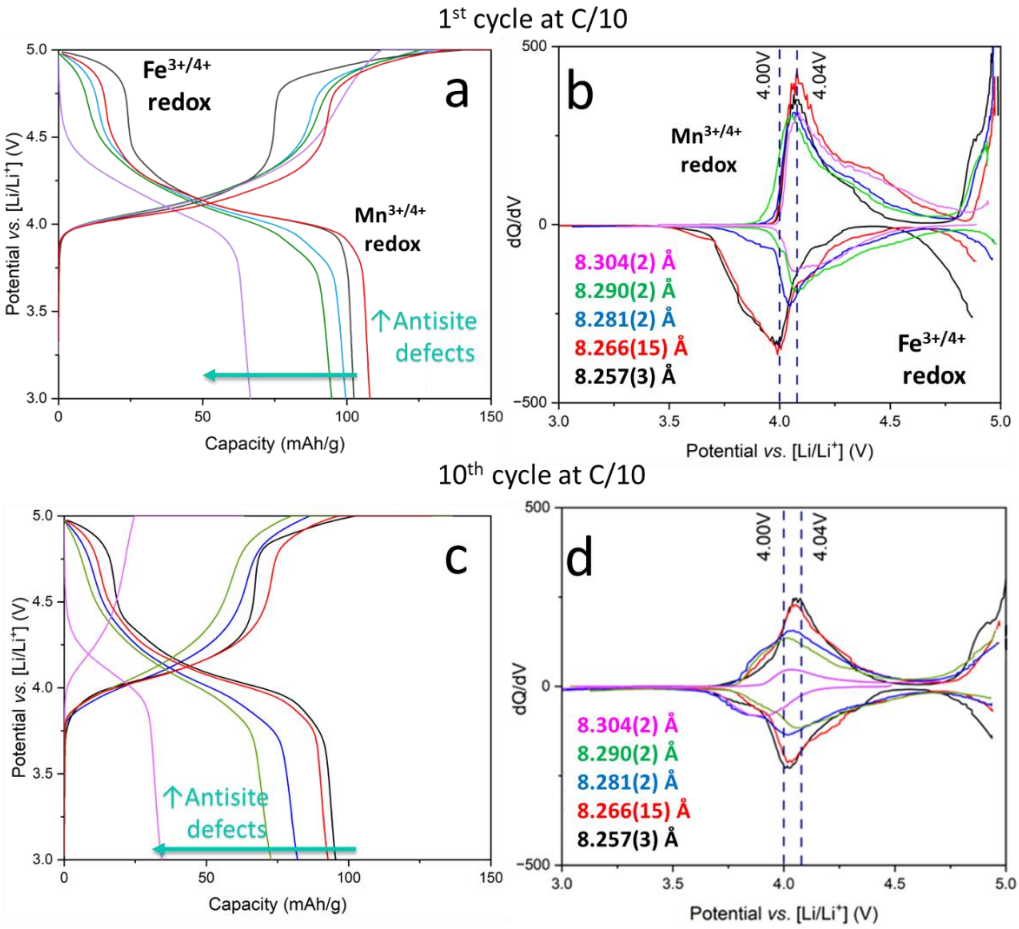

Figure 41: First (a, b) and tenth (c, d) cycles at C/10 in a 3.0-5.0V vs Li/Li⁺ voltage window for the five selected LFMOs with different quantity of antisite defects. In the left part-a & c- the voltage curves are shown and, in the right part -b & d-of the figure the dQ/dV for the same cycles are depicted. The arrows indicate the increase in the percentage of antisite defects.

	Antisite defects (%)	Discharge capacity 1st cycle ($mAhg^{-1}$)	Total average voltage (V)
LFMO-290	14(4)	102.47	4.28
Mcp-134	15(4)	107.99	4.21
LFMO-325	22(5)	103.05	4.20
LFMO-323	26(2)	94.75	4.17
LFMO-234	35(5)	66.567	4.12

Table 22:Discharge capacity and average voltage for first cycle of the five selected samples cycled at C/10 in a 3-5V vs. Li/Li^+ voltage window.

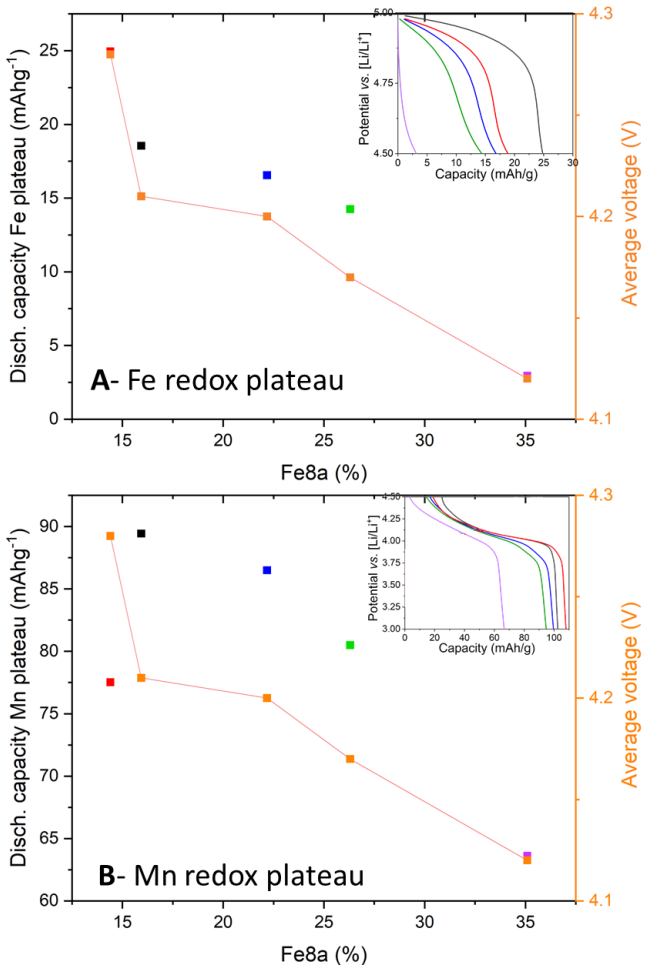

Figure 42: Discharge capacity and total average voltage of the first discharge pseudo-plateaus, related to $Fe^{3+/4+}$ at 4.5V (A) and $Mn^{3+/4+}$ at 3V (B) vs. the percentage of Fe in tetrahedral positions.

The evolution of the discharge capacity over cycling is shown in Figure 43. The trend observed during the first cycle is maintained during the first 35 cycles, resulting in higher discharge capacities in the samples with lower quantity of defects (black curve) than in the samples with higher quantity (purple curve). Furthermore, the sample with a greater quantity of antisite defects presents a faster capacity decay. It should be noted that at such high voltage the instability of the electrolyte at high voltages also contributes to the capacity decay. Indeed, as shown in Table 23 the coulombic efficiency of the half cells does not exceed 61.17% in the first cycle (15(4)% of antisite defects, Mcp-134) nor 69.12% in the 35th cycle (35(5)% of antisite defects, LFMO-234). However, samples with little quantity of defects are more stable maintaining 81.67% of capacity retention (LFM-290), while samples with high quantities of defects maintain only 31.43% of the initial capacity (LFMO-234).

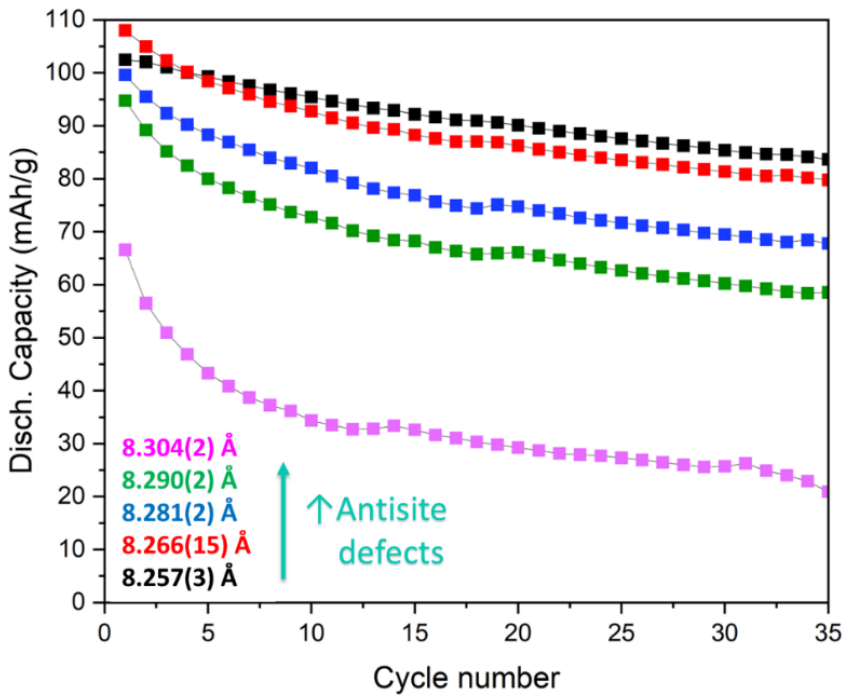

Figure 43: Discharge capacity within the first 35 cycles at C/10 in a 3-5V vs. Li/Li$^+$ voltage window for the five LFMOs selected with different quantity of antisite defects.

	Capacity retention 35th cycle (%)	Coulombic efficiency 1st cycle (%)	Coulombic efficiency 35th cycle (%)
LFMO-290	81.67	57.99	64.37
Mcp-134	73.88	61.17	67.93
LFMO-325	65.78	58.72	60.08
LFMO-323	61.79	56.01	51.43
LFMO-234	31.43	37.87	69.12

Table 23: Capacity retention for the 35th cycle and coulombic efficiencies for both 1st and 35th cycles of the selected samples cycled at C/10 in a 3-5V vs. Li/Li^{+} voltage window.

Preliminary rate capability experiments of the samples with higher and lower quantity of defects have been first performed at different charge-discharge-rates (C(D)-rates), applying the same rate to both charge and discharge processes, and within the same voltage window as for the C(D)/10 galvanostatic tests (3-5 V *vs*. Li/Li^{+}). To do so, 5 cycles were run for each C-rate (C(D)/20, C(D)/10, C(D)/5, C(D)2, C(D)) and again C(D)/20 to evaluate the reversibility. In Figure 44 the evolution of the discharge capacity over the 30 cycles is represented.

The discharge capacity for the sample with the higher quantity of defects (LFMO-234) decays drastically as only 12.64% of capacity retention is obtained after 25 cycles and the initial capacity value is not recovered when coming back to low C(D)-rate (reaching only 46.12% of the initial capacity at the 30th cycle C(D)/20). For the sample with the least amount of antisite defects (LFMO-290), it is remarkable that the capacity retention for the 25th cycle at C(D) is still 87.38% and it increases to 91.29% for the 30th cycle at C(D)/20.

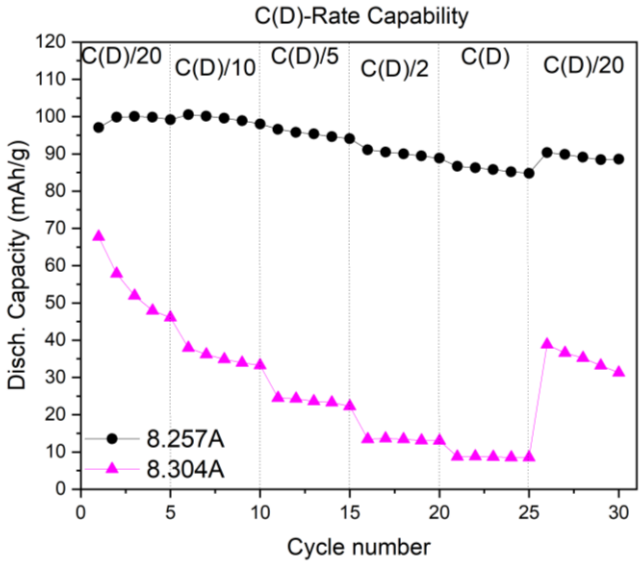

Figure 44: Discharge capacities vs cycle number for the Rate Capability experiment on the LFMOs with the higher (pink) and lower (black) quantities of antisite defects in a voltage window of 3-5V.

The composition that has shown the best electrochemical performance is the less defective sample, thus, the one with smaller cell parameter, LFMO-290 (a=8.257(3)Å). This sample has been subjected to further tests and higher C- (charge), D- (discharge) and C(D)- (charge and discharge) rates to better understand the LFMO kinetic limits due to the fast insertion, during discharge, or fast extraction, during charge, of the lithium ions.

Figure 45 shows the rate capabilities in a 3.5-5V voltage window *vs.* Li/Li^+ performed in Swagelok-type cells. In Figure 45-a, the C(D)-rate capability is depicted indicating the discharge capacities for each cycle. C(D)-rates were performed from C(D)/10 to 20C(D) intercalating two cycles at C(D)/10 between C(D)-rates to ensure the equilibrium of the material before every change. The discharge capacity decreases with the increase in C(D)-rate from 117 $mAhg^{-1}$ at the 1st cycle at C(D)/10 to 0 $mAhg^{-1}$ at 20C(D) in the 34th cycle. When cycling again at C(D)/10, 85.5% of the discharge capacity is recovered with respect to the first cycle.

In Figure 45-b, the C-rate capability is depicted indicating the discharge capacities for each cycle. Discharges were performed at

C/10 while charges went from C/20 to 50C. The discharge capacity increases for the first 5 cycles at C/20 until 103 $mAhg^{-1}$ at C. Then, the discharge capacity decreases at faster C-rates until 0 $mAhg^{-1}$ at 40C. However, within the 5 cycles performed at each C-rate, the discharge capacity remained stable.

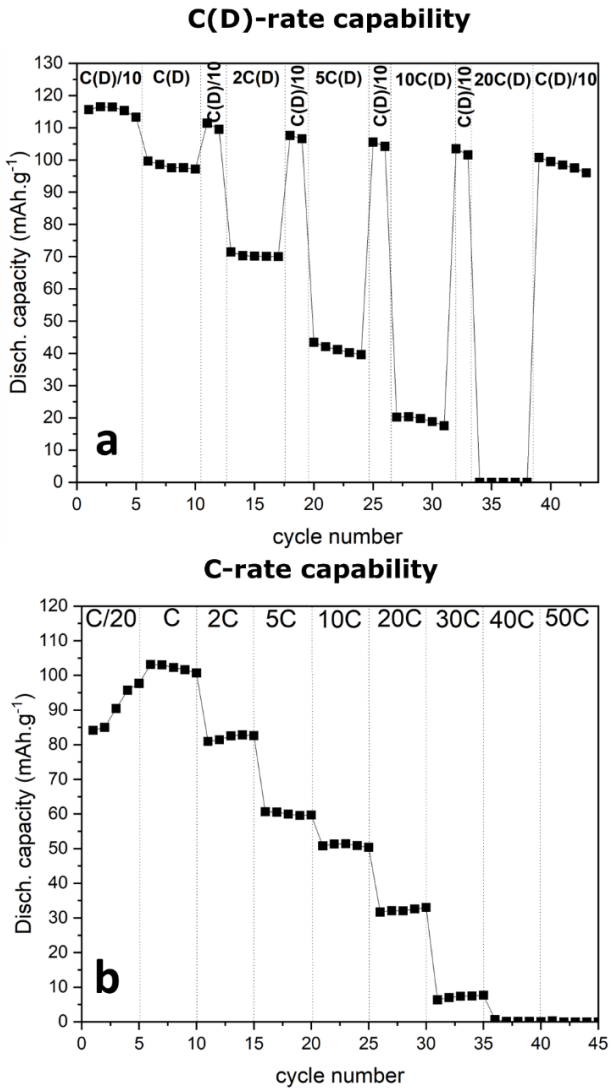

Figure 45: Rate capability tests performed on LFMO with low quantity of antisite defects for a) from C(D)/10 to 20C(D) intercalating 2 cycles at C(D)/10 between C(D)-rates and, b) from C/20 to 50C, in this case discharges were performed at D/10. Dot lines indicate the change in the C-rate.

In the previous C-rate experiments, a limitation of the material while cycling at fast C-rates was found. The capacity decays while increasing the C-rates and it was not possible to cycle faster than 30C. In Figure 46-a, the discharge capacities for the D-Rate capability are depicted charging the cell at C/10 and discharging from D/20 to 700D increasing 20D the D-rate every five cycles. It should be noted that the cells were cycled in constant current mode CC (and not constant current constant voltage, CCCV) to avoid degradation of the electrolyte at the highest voltage. The discharge capacity slightly decreases with the cycle number, which can be due not only to the limitations of the material but also to the degradation of the electrolyte at high voltages during charge. However, the material exhibits a remarkable capacity, even when discharged at very fast rates. Indeed, the discharge capacity is maintained in D/20 and D and, at 700D, 30% of the capacity is still maintained.

Figure 46-b depicts the voltage curves for the first cycle of 6 of the D-rates tested (D/20, D, 60D, 120D, 360D y 700D corresponding to the following discharge times: 20h, 1h, 1min, 30s, 10s and 5.2s, respectively). It can be observed that, as expected, polarization increases with the discharge rate. After cycling at D, both plateaus decreased at faster D-rates obtaining a decrease in the discharge capacity from 105mAh/g in the 1^{st} cycle at D/20 to 29mAh/g in the 210^{th} cycle at 700D.

The results obtained from the different rate capability tests suggest that extracting the lithium ions from the structure is more kinetically limited than inserting them and impressive discharge kinetics are observed.

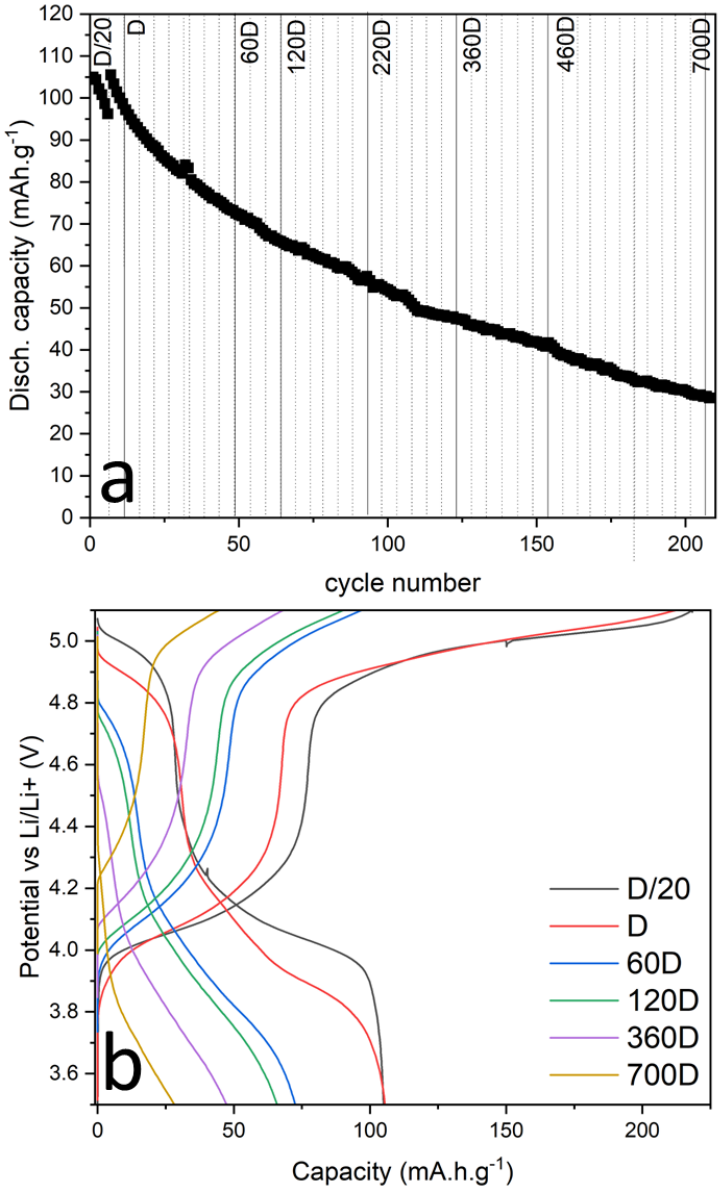

Figure 46: Discharge rate capability discharging from D/20 to D-rates up to 700D and charging at C/10 on the LFMO-290 (8.257(3)Å) in a voltage window of 3.5-5.1V vs. Li/Li$^+$. a) The discharge capacity over the 210 cycles performed at different D-rates. Dot lines indicate each increase in the D-rate and solid lines the written D-rate in the graphic. b) The voltage curves for 6 of the D-rates tested.

4.6. In operando XRD and XAS study of LFMO

To further understand the electrochemical and structural behavior of LFMO upon cycling, in operando synchrotron XRD (sXRD) and XAS experiments on three samples with different quantities of antisite defects have been performed at NOTOS beamline in ALBA synchrotron. The synthetic conditions and quantities of defects of the selected samples, Lcp-358, Mcp-359 and Hcp-244, are indicated in Table 24.

	Lcp-358	Mcp-359	Hcp-244
Position	A2	B2	C3
Li excess (f.u.)	0.02	0.02	0.02
Gel formation time (h)	4	4	4.5
Temperature heating ramp (°C/min)	5	5	5
Annealing temperatura (°C)	700	700	900
Annealing time (h)	10	10	10
Temperature cooling ramp (°C/min)	5	5	5
Cell parameter (Å)	8.246(3)	8.267(3)	8.299(2)
Antisite defects (%)	Not detected by sXRD	22(4)	33(3)

Table 24: Synthetic parameters used to synthesize the selected samples for the in operando study and their resulting cell parameter.

The electrodes of each sample, with around 6mg of mass loading, were assembled in a special in situ cell with Be window[166] in half-cell configuration and cycled at a C-rate of C/10 and a D-rate of D, in the case of Lcp-358, and D/10, in the case of Mcp-359 and Hcp-244, in a voltage window from 3.5 to 5V *vs.* Li/Li^+ using 1M $LiBF_4$ in EC:DMC (3:7 by wt.) as electrolyte. The electrode preparation and the equipment specifications are described in Chapter 6 (Section 6.2.2.).

As observed in Figure 47, independently on the quantity of defects present on the sample, a solid solution behavior was observed, as expected from the calculations performed in Chapter 3. For Lcp-

358, a discharge capacity of 130 $mAhg^{-1}$ was obtained. Although Mcp-359 and Hcp-244 were discharged 10 times slower than Lcp-358, the discharge capacity decreased with the increase in the quantity of defects, obtaining 111 $mAhg^{-1}$ and 87.8 $mAhg^{-1}$ of discharge capacity for Mcp-359 and Hcp-244, respectively. While comparing the sXRD patterns at OCV and at the end of the discharge, both patterns overlap for Lcp-358, indicating that reversibility was completely achieved. On the contrary, for Mcp-359 and Hcp-244 patterns did not overlap and, thus, the cell volume after the contraction of the structure due to the lithium extraction was not recovered. These results indicated that the reversibility was poorer for higher quantity of defects.

The in operando sXRD patterns of Lcp-358 and Mcp-359 samples were refined performing pseudo-Rietveld refinements, as the quality of the data did not allow to refine the structure of the materials due to the short 2theta range studied. However, the evolution of their cell parameters was studied, as depicted in Figure 48. It is worth noting that for Mcp-359 the initial cell parameter values (a= 8.2647(9)Å) are not recovered at EOD (a= 8.2525(9)Å). In addition, during charging there is a change in the slope denoting a different charge mechanism. This observation may be due to the affection of the antisite defects upon delithiation. It can be hypothesized that it is easier to extract the initial lithium atoms during the Mn redox activity (Patterns 0-10) and less preferred during the Fe redox activity (Patterns 11-25) as the charge in the slope reflects a slower contraction of the cell in this plateau. In the case of Hcp-244, it was not possible to perform the refinements due to the lower quality of the data, see Figure 49-a, due to the presence of different particle sizes and the impossibility of measuring at different angles while moving the cells during cycling in NOTOS beamline. This hypothesis was confirmed by measuring the same sample in a rotating capillary in MSPD beamline, in ALBA synchrotron, and observing that the peaks were well defined in this kind of measurement, see Figure 49-b.

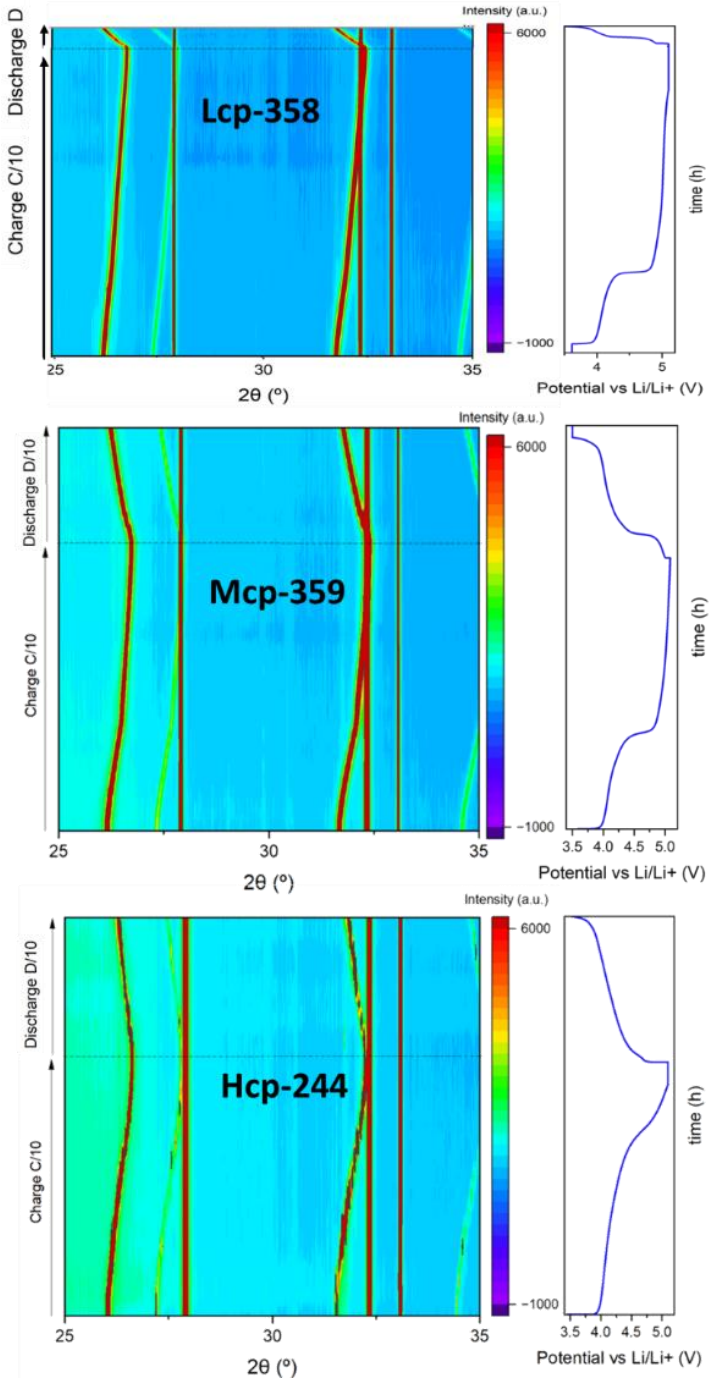

Figure 47: 2D plot for the in operando XRD patterns for the 1st cycle at C-rate of C/10 and a D-rate of D, in the case of Lcp-358, and D/10, in the case of Mcp-359 and Hcp-244, in a voltage window from 3.5 to 5V vs. Li/Li+.

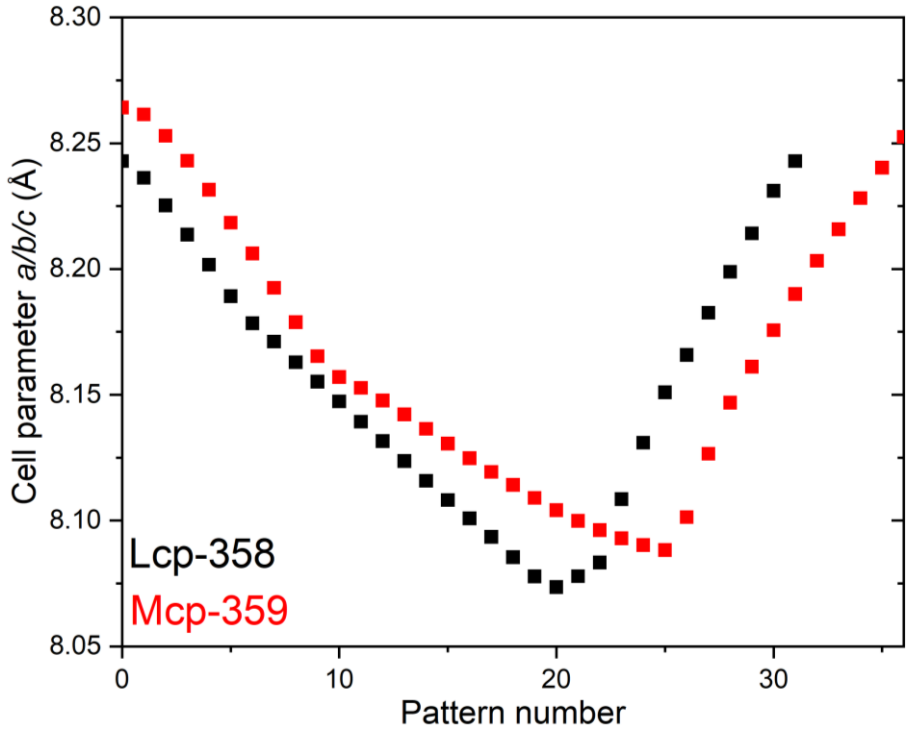

Figure 48: Evolution of cell parameters upon cycling for samples Lcp-358 and Mcp-359. Note that for Lcp-358, EOC is achieved at pattern #20 and EOD at #32, for Mcp-359 EOC is achieved at pattern #25 and EOD at #36.

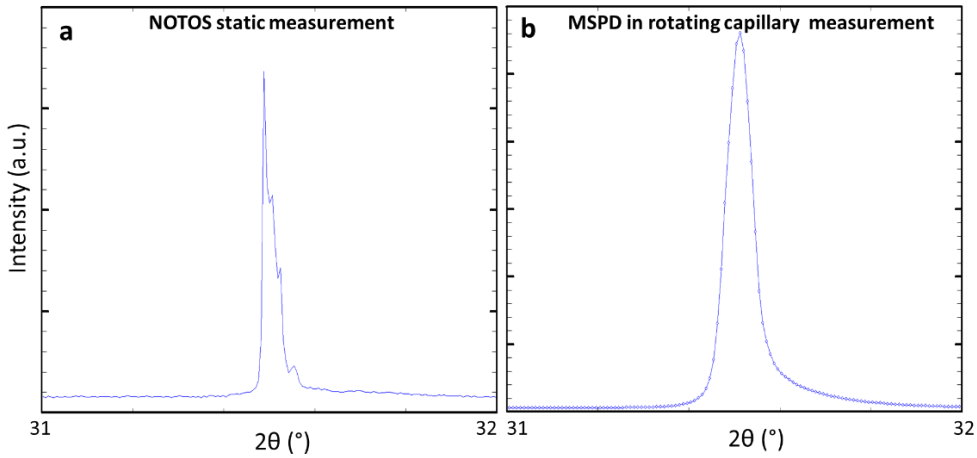

Figure 49: Hcp-244 diffraction patterns measured under different conditions: a) measured at NOTOS beamline in static mode in the in situ cell, and b) measured at MSPD beamline under rotation in a capillary.

In operando XAS measurements were performed simultaneously with the sXRD measurements. The XAS results obtained confirmed that, for all samples, during the charge Mn reacted first followed by Fe. The 2D plots of the Fe and Mn K-edge spectra obtained during the in operando measurements are depicted in Figure 50. With the measurements performed via in operando XANES, the Fe oxidation states during cycling have been elucidated, as presented in Table 25, by fitting the data using Fe, Fe_3O_4, FeO and Fe_2O_3 as reference materials (Figure 51, above). Sample Lcp-358 was the one achieving a higher Fe oxidation state of +3.3(1) at the end of charge (EOC) at 5.1V *vs.* Li/Li^+. It also presented high reversibility, obtaining +3.0(1) at the end of discharge (EOD) at 3.5V *vs.* Li/Li^+, the same value obtained at OCV. In the case of Mcp-359 and Hcp-244 only +3.2(1) was achieved at the EOC with lower reversibility respect to Lcp-358.

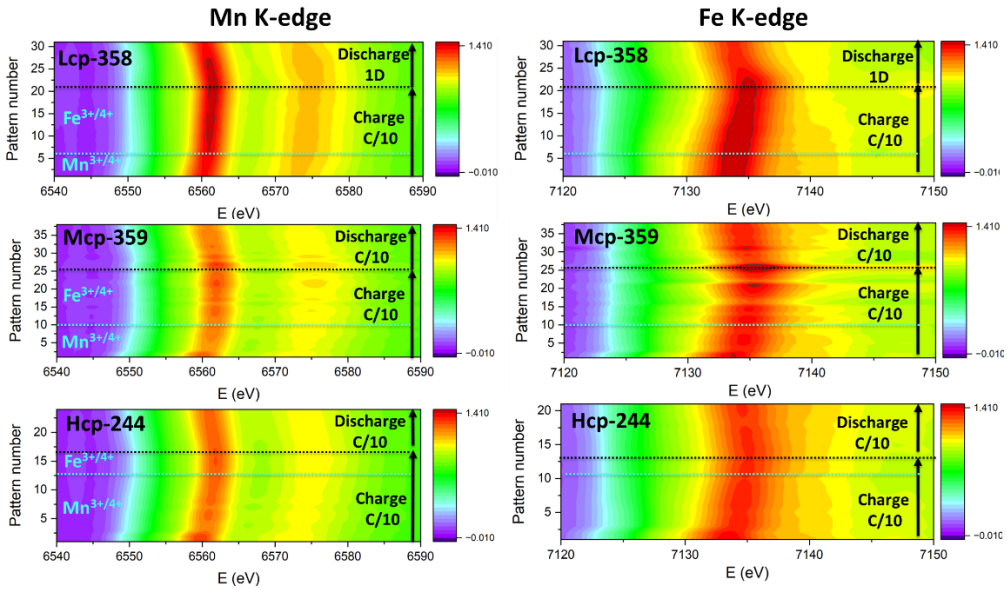

Figure 50: 2D plot for the in operando Mn K-edge (left) and Fe K-edge (right) XAS spectra for the 1st cycle at C-rate of C/10 and a D-rate of D, in the case of Lcp-358, and D/10, in the case of Mcp-359 and Hcp-244, in a voltage window from 3.5 to 5V vs. Li/Li^+. Black dash lines indicate the end of the charge and blue dash lines indicate the half charge with indication of the $Mn^{3+/4+}$ redox couple contribution and the $Fe^{3+/4+}$ redox couple contribution.

	Lcp-358	Mcp-359	Hcp-244
Edge position at OCV (eV)	7123.1	7123.1	7123.1
Fe approx. oxidation state at OCV	**3.0(1)**	**3.0(1)**	**3.0(1)**
Edge position at EOC (eV)	7124.4	7123.8	7123.9
Fe approx. oxidation state at EOC	**3.3(1)**	**3.2(1)**	**3.2(1)**
Edge position at EOD (eV)	7123.3	7122.9	7123.6
Fe approx. oxidation state at EOD	**3.0(1)**	**2.9(1)**	**3.1(1)**

Table 25: Fe Edge position and oxidation states obtained by the XAS measurements of the selected samples during in operando experiments.

The Mn oxidation states upon cycling revealed by XAS, by fitting the data using MnO MnO_2, Mn_3O_4 and Mn_2O_3 as reference materials (Figure 51, below), are presented in Table 26. The three studied samples presented comparable Mn oxidation states at OCV and EOC. Regarding the EOD, a trend could be identified in which more antisite defects lead to lower reversibility in the Mn oxidation state.

	Lcp-358	Mcp-359	Hcp-244
Edge position at OCV (eV)	6548.3	6547.8	6547.9
Mn approx. oxidation state at OCV	**3.2(1)**	**3.1(1)**	**3.2(1)**
Edge position at EOC (eV)	6550.3	6550.8	6550.7
Mn approx. oxidation state at EOC	**3.8(1)**	**3.9(1)**	**3.9(1)**
Edge position at EOD (eV)	6548.3	6548.6	6548.9
Mn approx. oxidation state at EOD	**3.2(1)**	**3.3(1)**	**3.4(1)**

Table 26: Mn Edge position and oxidation states obtained by the XAS measurements of the selected samples during in operando experiments.

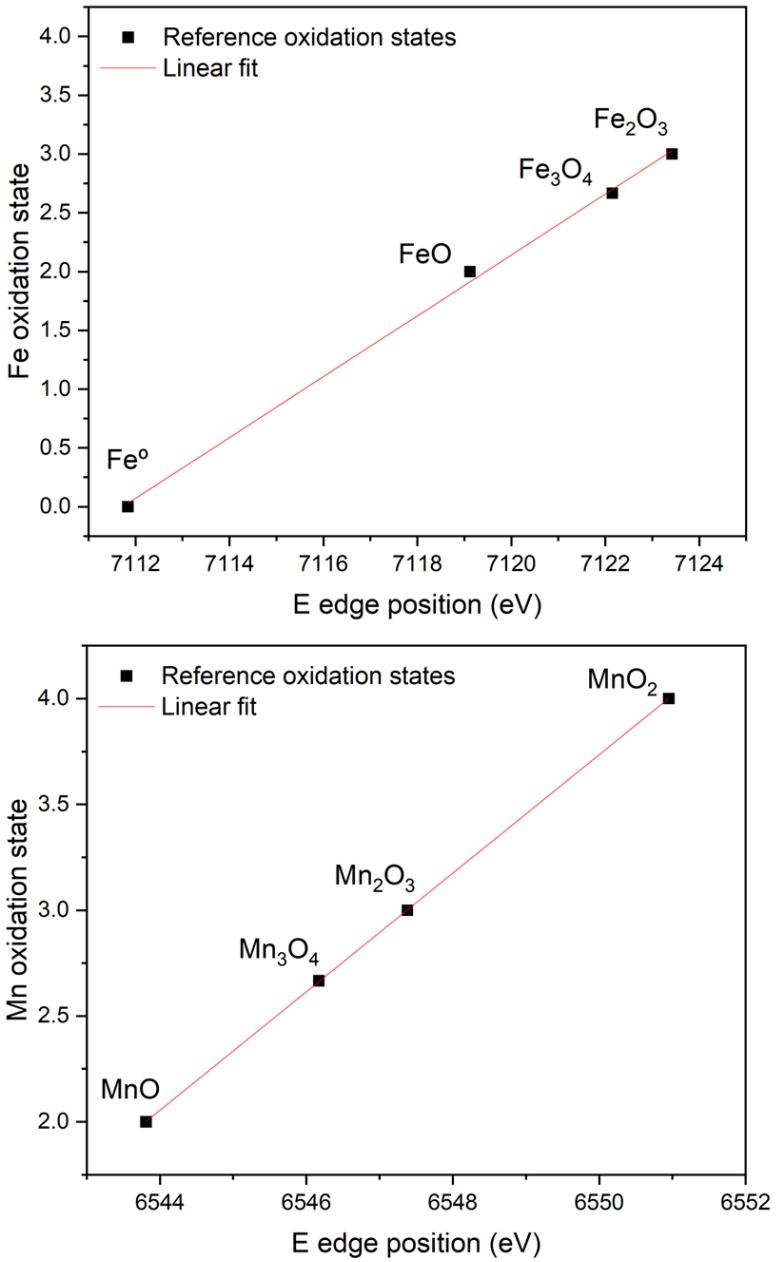

Figure 51: Oxidation states fitting for Mn references (below) and Fe references (above) used to elucidate the oxidation states during the in operando XAS measurements.

4.7. Microstructural design to optimize LFMO

During the previous sections the impact of synthetic parameters in the final structure of LFMO samples was clarified. This knowledge gained made possible to optimize the synthetic conditions to get LFMO with minimized quantity of antisite defects and thus, the best electrochemical performance. Sample Lcp-358, whose synthetic conditions are specified in Table 24, was cycled in a Swagelok-type cell at C/10 in a 3.5-5.0V vs. Li/Li^+ voltage window as depicted in Figure 52. This sample showed a discharge capacity of almost $130mAhg^{-1}$ with an average voltage of 4.4V, as depicted in Figure 52. The obtained values are the highest values ever reported for LFMO as the quantity of defects have not been controlled until the present work.

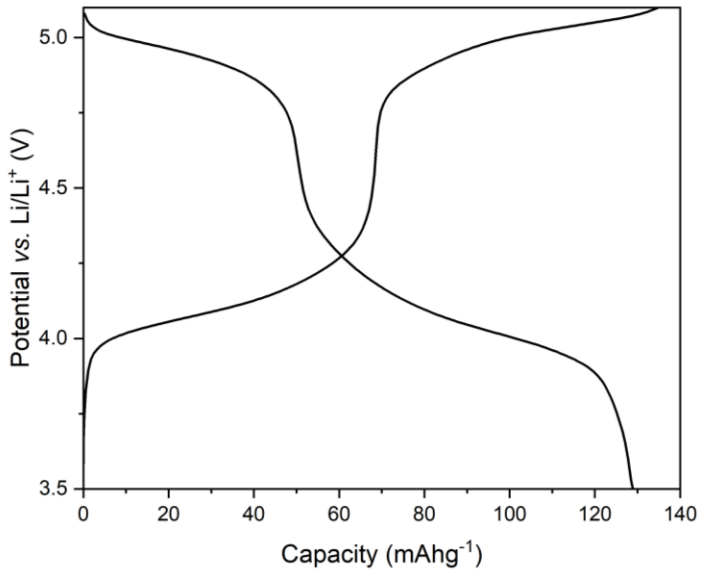

Figure 52: Second cycle at C/10 in a 3.5-5.0V vs. Li/Li^+ voltage window for LFMO-358.

Table 27 presents the synthesis method and the electrochemical results of the most relevant bibliographic studies performed on LFMO. In the literature only three studies reported rate capability results, in all cases significantly inferior to the ones herein presented. Indeed, LFMO had never been cycled at rates higher than 20C until now.

Scientific work	Synthesis	Rate capability	Comparison of results
This thesis	**Sol-gel synthesis using nitrates**	**>100mAh/g at D & 29mAh/g at 700D (cycle 210th) with 5.1V cut-off-See Fig. X-**	**≈130mAh/g in the first cycle at C/10 with 5.2V cut-off -See Fig.52- with ≈82% of capacity retention -See Fig. 43-**
Bhaskar *et al.* 2010[73]	Pechini using acetate precursors	<80mAh/g (11th cycle) at 2C, 0mAh/g (21st cycle) at 20C with 5.3V cut-off	120mAh/g in the first cycle at C/2 with 5.3V cut-off
Pico *et al.* 2014[94]	Sol-gel in solution using nitrate precursors	<60mAh/g at C/5 cycling with 5.3V cut-off	75mAh/g in the first cycle at C/10 with 5V cut-off. <40mAh/g in 10th cycle
Mu *et al.* 2017[96]	Solid state using oxide and carbonate precursors	≈75 mAh/g at 1C (31st cycle) and ≈75mAh/g at 1D (31st cycle) with 5V cut-off	<115mAh/g in the first cycle at C/10 with 5V cut-off
Ohzuku *et al.* 2001[86]	Solid state using hydroxide precursors	Not reported	125mAh/g in the first cycle at 0.17mA/cm^2 with 5.2V cut-off (only first cycle shown)
Shigemura *et al.* 2001[95]	Solid state using oxide, hydroxides, and carbonate precursors	Not reported	≈125mAh/g in the first cycle at C/10 with 5.3V cut-off (high capacity fading)
Eftekhari *et al.* 2003[78]	Solid-state using carbonates and hydroxides.	Not reported	123 mAh/g at C/10 with 5.3V cut-off (only 1 cycle reported)
Kawai *et al.* 1998[161]	Solid-state using carbonate precursors	Not reported	125 mAh/g in the first cycle at 0.5mA/cm^2 with 5.3V cut-off (high capacity fading)

Table 27 Bibliographic study of the LFMO literature.

The presented LFMO thus reaches an energy density of 572 Wh/kg and is potentially able to deliver >660 Wh/kg. Such value would be superior to that of the commercial 622NMC (170 $mAh.g^{-1}$ discharge capacity at 4.3 V cut-off voltage and with an average voltage of 3,8 V), in addition, LFMO results in a reduction of 66% of critical elements (Li, Ni, Co) compared to 622NMC.

4.8. Conclusions

In this study, the impact of various sol-gel synthetic parameters on the structure of LFMO has been investigated. The structural characterization performed via SEM, Mössbauer, XRD, NPD, XANES and EXAFS revealed the presence of antisite defects that were quantified and correlated with cell parameters. Through systematic variations on the synthetic parameters, it was found that higher annealing temperatures and lower nominal Li excess per f.u. resulted in an increased of antisite defects in the LFMO spinel structure.

The presence of antisite defects has a very strong influence on the electrochemical properties of LFMO. A significant decrease in discharge capacity and in the average voltage of the Fe and Mn redox plateaus was observed in the presence of these defects. Additionally, the C-rate and capacity retention were adversely affected. By controlling the quantity of antisite defects in the material, the electrochemical properties of LFMO have been effectively optimized maximizing its overall performance. Thanks to the control of these defects in the LFMO structure the best electrochemical results ever published in literature are reported in this study, reaching 130$mAhg^{-1}$ with 4.4V *vs.* Li/Li^+ of average voltage at 1D and with 30% of capacity retention at 700D (5.2 s).

The analysis of the redox processes conducted through in operando X-ray Absorption Spectroscopy (XAS) confirmed the presence two distinct redox processes at approximately 4.0 V and 5.0 V *vs.* Li/Li^+. These processes were attributed to the oxidation of Mn^{3+} into Mn^{4+} and the oxidation of Fe^{3+} into Fe^{4+} across all the tested electrodes.

These findings shed light on the complex electrochemical behavior of the LFMO and provide valuable insights for further research and development in energy storage applications.

CHAPTER 5: Summary and future perspectives

5.1. General conclusions

The research conducted in this PhD thesis represents a significant contribution to the field of materials research and energy storage technology. The combination of theoretical and high-throughput experimental approaches has enabled a comprehensive understanding of the behavior of LFMO as a promising material for lithium-ion batteries.

Batteryino-I automated platform has been designed for the efficient synthesis of electroactive inorganic materials on a lab-scale with high-throughput capabilities. This module is specifically engineered to handle and mix precursor solutions in precise stoichiometries, enabling various synthesis routes such as solid-state, sol-gel, Pechini, and other hydro/solvothermal methods. The high-throughput capabilities of this platform allowed for the efficient exploration of various synthesis parameters and the creation of a wide range of materials. The **successful demonstration of the use of the module for sol-gel synthesis of LFMO and Li-Ni-Mn oxide** showcases the platform's versatility and its potential to accelerate the discovery and development of new battery materials. This automation not only reduces manual handling but also ensures repeatability and consistency in the synthesis process, thereby saving time and resources in research and development.

LFMO has been shown to be an interesting high-voltage cathode material that operates at an average voltage of 4.4V *vs.* Li/Li^+ with a theoretical capacity of $148mAhg^{-1}$ and that allows reducing notably the quantity of critical elements (such as Li, Ni, Co) in comparison with other cathode materials such as NMC, NCA or other Mn-spinels. In this work, it has been suggested, by a computational study via density functional theory (DFT) using SCAN and PBE+U functionals, that LFMO operates by a **preferred solid solution mechanism** during the lithium (de)insertion process and that **the**

phase stability and voltage behavior are unaffected by the Fe/Mn distribution. While the SCAN functional exhibited better agreement with experimental cell parameters and volumes, the PBE+U functional provided more accurate average voltages. Bader charge calculations confirmed a transition from $Mn^{3+/4+}$ to Mn^{4+} and, the Bader analysis performed via SCAN functional clearly identified Fe redox transitions from Fe^{3+} to Fe^{4+}, consistent with the experimentally described redox process. Additionally, **both functionals predicted an oxygen redox contribution to the electrochemical mechanism**, and the SCAN functional suggested the anionic redox in LFMO to be reversible.

It has been experimentally shown that antisite defects in the LFMO structure significantly influence its electrochemical behavior, a fact that was not understood from previous works. Samples with **fewer antisite defects exhibited superior electrochemical performance, with higher discharge capacity, Fe and Mn redox plateaus, and capacity retention.** Through the synthesis of more than 150 LFMO samples under varying conditions using Batteryino-I, it was shown that **synthetic conditions, such as the annealing temperature and the excess of lithium added at the beginning of the synthesis, are key parameters to control the percentage of antisite defects** in the final LFMO performance. The controlled synthesis of LFMO with minimized defects represents a crucial step in optimizing the electrochemical performance and advancing the efficiency of this kind of cathode materials. Furthermore, the **solid solution mechanism was confirmed experimentally** by in operando measurements.

The research conducted in this thesis demonstrates the importance of interdisciplinary approaches and the integration between experiments and theory in materials research. It provides a solid foundation for future studies in battery materials and energy storage technologies, promising further innovations and breakthroughs. The knowledge gained from this work is not limited to LFMO but can be extended to other battery materials, accelerating the discovery of advanced materials for the next generation of energy storage devices. Overall, this PhD research has significant implications for the development of greener and

more efficient energy storage solutions, contributing to a sustainable and cleaner future.

5.2. Future perspectives

In this work the enormous potential of high throughput experimentation for the acceleration of materials research has been shown. For this reason, future work should be focused on the creation of material acceleration platforms (MAPs) aimed at designing and test new materials in an autonomous and faster way combining robotics, artificial intelligence, and advanced computing with material science. These platforms should integrate, not only synthesis modules as we did in this work, but also other experimental steps that have represented a bottleneck in this work. These could include autonomous modules dedicated to the grinding of the samples and the preparation of the XRD and electrochemical measurements. Moreover, machine learning experimental planners should be considered to extract reliable correlations with the minimum number of experiments. Additional applications that allow automatic data treatment, such as the in-house developed FullProfAPP program for XRD data treatment, would be really useful to accelerate developments in the field. This would allow to move forward self-driven platforms that generate a closed-loop experimental process that integrates the feedback from theoretical calculations, synthesis outcomes, and characterization data.

Furthermore, during the study of the LFMO in the present work, there have been some open questions as how the lithium ions migrate during (de)lithiation in the defective LFMOs, and the oxygen redox mechanism of this material upon lithiation and delithiation. A computational study of the defective LFMO should be performed to better understand the ionic paths and the role of the tetrahedral iron. In operando NPD would also be useful to clarify the lithium behavior in the structure. Other mechanistic studies using for example Potentiostatic Intermittent Titration Technique (PITT) experiments are also recommended. The oxygen redox mechanism has been clearly identified from a computational point of view but must be studied from an experimental perspective to better understand its reversibility and mechanism. Future efforts should

also be directed towards further optimizations (i.e., coatings to stabilize the electrode/electrolyte interphase at high voltage) and upscaling of the defect-free LFMO.

CHAPTER 6: Methodology

6.1. Theoretical methods

6.1.1. Density functional theory

Density functional theory (DFT) is a highly successful computational approach used to determine the electronic structure of atoms, molecules, and solids. Its primary goal is to quantitatively understand various material properties based on the principles of quantum mechanics. In contrast to traditional electronic structure methods, which aim to find approximate solutions to the intricate Schrödinger equation for N interacting electrons in an external electrostatic potential created by atomic nuclei, DFT utilizes the one-body density as the fundamental variable. This simplification allows for computationally efficient calculations, even for large systems, as the dependence is reduced to just three spatial coordinates instead of the complex 3N coordinates associated with the wave function. The theoretical foundation of DFT is rooted in the Hohenberg–Kohn and Kohn–Sham theorems.[168]

DFT's precision and computational efficiency are constrained by the approximation of its exchange-correlation energy. As of now, researchers commonly employ the Local Density Approximation (LDA) and Generalized Gradient Approximations (GGAs) for their computational efficiency. However, the recently developed non-empirical Strongly Constrained and Appropriately Normed (SCAN) meta-GGA exhibits enhancements over LDA and the standard Perdew-Burke-Ernzerhof (PBE) GGA, particularly for a broad spectrum of materials with diverse bonding characteristics. Remarkably, in numerous instances, SCAN matches or even surpasses the accuracy of computationally expensive hybrid functionals, offering comparable efficiency to GGAs.[169]

6.1.1.1. Perdew-Burke-Ernzerhof plus the empirical Hubbard U correction generalized gradient approximation (PBE+U GGA)

One of the limitations of the LDA and GGA functionals is the presence of self-interaction. Within the Coulomb potential, an electron experiences self-repulsion, which is effectively canceled out in the Hartree-Fock method through the exchange term. However, in DFT, where the exchange term is approximated, self-interaction is not completely eliminated. As a result, highly localized Kohn-Sham (KS) orbitals become unstable, causing unpaired electrons to delocalize spatially to minimize self-interaction. Consequently, both the LDA and GGA methods inadequately account for electronic correlation in systems with highly localized states, as they rely on the electron gas model to describe electronic interactions. For instance, the GGA method incorrectly predicts metallic or semiconductor behavior for many transition metal oxides, whereas these materials are experimentally known to exhibit strong insulating properties. In essence, the LDA and GGA approximations fail to provide an accurate description of the electronic structure of these highly correlated materials, especially concerning the gap between the conduction and valence bands.

In GGA the E_{XC} functional, exchange-correlation energy per particle of a system, can be described as follows:

$$\varepsilon_{XC}^{GGA}[\,\rho(\vec{r})] = \int f\,(\rho,\rho)\,\nabla\, d\,\vec{r} \tag{12}$$

In the 1990s, the PBE+U method was developed as an extension of the approximation functional to address electronic interactions.[170,171] The term PBE+U is used to denote the method itself, independent of explicit reference to LDA or GGA (LDA+U or GGA+U). This approach combines the computational efficiency of LDA/GGA with an explicit treatment of correlation using a Hubbard-like model for a specific subset of states within the system. As a result, the treatment of d and f electrons (which are inaccurately delocalized by standard DFT) is separated from that of s and p electrons. For this, a Hubbard-like interaction term, $E_{Hub,}$ is applied to correct the functional:

(13) $$E_{GGA+U}[\rho(r)] = E_{GGA}[\rho(r)] + E_{Hub}[\{n_i^\sigma\}] - E_{DC}[\{n_i^\sigma\}]$$

In this context, ρ(r) represents the electronic density, and ni^σ represents the occupations of the orbitals of atom i with spin σ, which are affected by the Hubbard term. Additionally, an extra term is introduced to prevent the duplication of interactions present in E_{Hub} and E_{GGA}. This term relies on two factors: the Coulomb interaction (U) and the exchange interaction (J). During the realization of this thesis, the rotationally invariant formalism introduced by Dudarev *et al.*[172] has been used, as implemented in the VASP code[145,146]. In this formalism, the parameters U and J are combined into a single effective parameter Ueff defined as Ueff=U -J.

The suitable value of the parameter U for the calculation varies depending on the material[173] and can be determined from experimentally derived properties like magnetic moments and band gaps[174], lithium insertion voltages[175], or reaction enthalpies[176].

For the study of the LFMO in this thesis the values have been taken from the Materials Projects database[177] (3.9 eV and 5.2 eV for Mn and Fe, respectively), which were obtained by fitting binary oxide formation energies[176.]

We performed spin-polarized calculations, initializing from a high-spin configuration. This approach is primarily aimed at enhancing the electronic convergence of our calculations. It is worth noting that as the DFT relaxation progresses, the system may naturally transition to its energetically favorable state. Although, Li et al. studied experimentally the magnetic properties of LFMO concluding that it presents an antiferromagnetic ordering below a Neel temperature (T_N) of 34K[91,93], we restricted our calculations to ferromagnetic ordering for simplicity, as a practical computational compromise necessary for conducting a high-throughput study involving hundreds of distinct atomic geometries[111] considering the often minimal energy differences between different magnetic orderings.[178,179] PBE-based projector augmented wave potentials[180] were used to replace core electrons, while the Li (1s, 2s), Fe (3p, 3d, 4s), Mn (3p, 3d, 4s), and O (2s, 2p) electrons were treated

explicitly as valence electrons and their wave-functions were expanded in plane waves with a cut-off energy of 600 eV. The grid of k points used for each supercell can be seen in Annex II.

6.1.1.2. Strongly Constrained and Appropriately Normed meta- generalized gradient approximation (SCAN mGGA)

Efficient computation of the ground-state energy, electron density, and related properties of ordinary matter is achieved using semilocal approximations to the exchange-correlation energy as a functional of the density. In 2015, Perdew *et al.*[169] introduced the first fully constrained meta-generalized-gradient approximation (mGGA) that satisfies all known exact constraints for a meta-GGA. This novel approach was also exact or nearly exact for certain "appropriate norms," such as rare-gas atoms and nonbonded interactions.

The mGGA approach includes the second derivative of the electron density. In practice the orbital kinetic energy density is used, written using the occupied KS orbitals:

(14) $$\tau(r) = \frac{1}{2}\sum_i^N |\nabla \psi_i(r)|^2$$

where ψ_i is the electron orbital i for a wavefunction that describes a non-interacting N electron system.

In this case, the E_{XC} functional can then be described as follows:

(15) $$\varepsilon_{XC}^{mGGA}[n] = \int drf\ (n,(r)),|\nabla n(r)|,\ \tau(r))$$

The most used mGGA is the SCAN mGGA that demonstrates remarkable accuracy, particularly for systems where the exact exchange-correlation hole is localized near its electron, and it excels in predicting lattice constants and weak interactions.[181]

6.1.2. Clusters Approach to Statistical Mechanics (CASM)

In this thesis, in **Chapter 3**, CASM has been used to compute the configurational disorder of Li/Vac or Fe/Mn within the material of interest, LFMO, for a further study on its structural and electrochemical properties.

CASM is an open-source software package designed for first-principles statistical mechanical studies of multi-component crystalline solids developed by the Van der Ven group.[182] It offers powerful tools for systematically enumerating mechanical, vibrational, chemical, and magnetic configurations within a parent crystal structure. It enables the exploration of the energy landscape of a specific crystal, generating the training data necessary to parameterize cluster expansions of the energy. CASM's capabilities extend to studying the thermodynamics of systems with multiple components.[183]

The software is open-source and consists of C++ libraries and Python scripts. It interfaces with first-principles electronic structure codes, automates the construction and parameterization of effective Hamiltonians, and subsequently builds highly optimized (kinetic) Monte Carlo codes to predict finite-temperature thermodynamic and kinetic properties.

6.2. Experimental methods

6.2.1. Materials and synthesis

Case study 1: $LiFe_{0.5}Mn_{1.5}O_4$

For the synthesis of the LFMO spinels, described in **Chapter 2**, a sol-gel synthesis approach was used. This synthetic method involves converting a liquid mixture containing the metal reactant solutions required into a solid gel through controlled hydrolysis and condensation reactions. This results in a three-dimensional network of linked particles. The gel is then dried and subjected to heat treatment to remove solvent and organic components and enhance material properties. The sol-gel method was selected for offering several advantages, including the ability to control composition and morphology at nanoscale level. This method was also selected for allowing working in solution which permits the use of Batteryino-I.

Stoichiometric volumes of the reactant solutions, $LiNO_3$ (Sigma-aldrich >99%) 1M, $Fe(NO_3)_3.9H_2O$ (Sigma-aldrich >98%) 0.3M, $Mn(NO_3)_2.H_2O$ (Sigma-aldrich >97%) 0.5M, were pumped into the

12 crucibles using the autonomous module according to the program workflow scheme shown in Figure 12. Then, after 1 min of stirring the metal mix of solutions, citric acid 2.5M was added in a proportion 3:1 with respect to the metals as a chelating agent that increases the viscosity of the solution. Afterwards, the solutions were left under stirring overnight. Once the solutions were well mixed, ethylene glycol 6M (Sigma-aldrich >99%) was added to the 12 crucibles in a 3:1 ratio with respect to the metals as chelating agent, to generate the gel together with the citric acid. They were left to evaporate at 80°C under stirring during 3h. The 12 crucibles were placed in the oven. The annealing was made at 900°C during 10h. Both the cooling and the heating ramps were set at 5°C /min.

Prior to each synthesis, precursor solutions were flushed with N_2 to avoid the oxidation of the transition metals in solution. Furthermore, before starting each synthesis, to trace the possible errors and differences between sample batches done in different days, a certain amount of each reactant solution was stored and later measured by ICP.

Case study 2: $LiNi_{0.5+x}Mn_{1.5-x}O_4$

For the synthesis of the LNMO oxides described in **Chapter 2**, the same process as described for Case study 1 was followed using a solution of $Ni(NO_3)_2.6H_2O$ (Sigma-aldrich >97%) 0.5M as Ni precursor. The 48 syntheses were done in 4 sets of 12 samples changing the stoichiometries of the target composition for each sample.

High-throughput screening of LFMO synthetic parameters

For the synthesis of the LFMO spinels described in Chapter 4, a sol-gel synthesis approach was followed using the autonomous module previously developed in Chapter 2 undertaking the same protocol as in Case study 1. The parameters that were screened to better understand the structural properties and synthetic mechanism of this material were: annealing temperature, annealing time, cooling ramp, heating ramp, gel formation time, position in the automated module, position in the oven and Li excess added at the beginning of the synthesis.

6.2.2. Characterization techniques

X-ray diffraction

X-ray diffraction, followed by Rietveld analysis[184], was used to identify the crystallographic structure of the synthesized powders presented in **Chapter 2, 3 and 4**. XRD patterns were recorded on a Bruker D8 Discovery diffractometer equipped with a Cu source Kα1 (accelerating voltage of 40 kV, λ = 1.54053 Å) in the Bragg−Brentano geometry. The XRD data for the LFMO were collected for 2θ angles from 5 to 80◦ with a step size of 0.02◦ and a step time of 0.45 s. A reference of corundum was previously measured to include the instrumental contribution. The software FullProf Suite[133,134] was utilized for structural analysis of the materials and to confirm their purity.

The pseudo-Rietveld refinements mentioned during **Chapter 2** were performed by using an IRF and by refining the cell and profile parameters, and the background in Rietveld mode. However, atomic parameters were fixed to ideal values.

In **Chapter 4** the complete Rietveld refinement was performed, and it is described in detail in this chapter. During the course of this work, the FullProfAPP was developed by our group in collaboration with the Institut Laue Langevin (ILL), Instituto de Ciencia de Materiales de Barcelona (ICMAB) and ALBA synchrotron. FullProfAPP allows high throughput refinements of crystallographic structures accelerating considerably the data treatment and allowing the researcher to select the parameters to refine and the refined order for a large number of datasets. Whenever specified, the FullProfAPP was used. Otherwise, the refinements were performed manually.

Representations and analyses of the crystal structures were done using the program VESTA[185].

Synchrotron X-ray powder diffraction patterns (sXRPD) of LNMO, in **Chapter 2**, were collected at the BL04-MSPD beamline[186,187] of the ALBA Synchrotron Light Facility (Barcelona, Spain) with assistance from François Fauth using λ= 0.8258 Å at

13KeV in the MYTHEN2 position sensitive detector. The sample preparation was performed by filling borosilicate 0.7mm capillaries and closing them with a flame. For sXRPD a reference of $Na_2Ca_3Al_2F_{14}$ was previously measured to generate the IRF to extract the instrumental contribution.

Thermal measurements of the Batteryino-I heating plate

To study the thermal behavior of the heating plate contained in the Batteryino-I module, in **Chapter 2**, an infrared camera (FLIR 325sc) was used with the support of Jean-Luc Dauvergne. The camera was configured for data acquisition at 16 Hz in a calibrated temperature range of -20 ºC to 120 ºC. Conversion of the radiometric data to apparent temperatures was performed using the internal calibration curves of the camera and fixing the emissivity at 0.95. Reflected and atmospheric temperatures were considered constant (20 ºC). Processing of the recorded data was performed using the FLIR software ResearchIR Max Version 4.40.11.35.

Electrode formulation and cell assembly

The electrochemical experiments presented in **Chapter 3** and in **Chapter 4** were done as follows.

The slurries were prepared by mixing the LFMO samples with Carbon Black and polyvinylidene fluoride (PVdF) binder in weight ratio of 80:10:10. The mixing was performed by magnetic stirring of the PVdF in N-Methyl-2-pyrrolidone (NMP) until its complete dissolution and adding to this mixture the Carbon and the LFMO for another 2h of stirring. The coating of the slurries was performed on Al foil current collector with active material loading around 2.5 mg in a Dr Blade. After cutting and drying, the positive electrode was assembled in half-cell configuration using Swagelok type cells and EL PAT-cells in an argon-filled glove-box (≤ 0.1 ppm H_2O and O_2) with a 12mm diameter LFMO positive electrode, a glass fiber separator (Whatman) and a 11mm diameter lithium metal disc counter-electrode, using 1M $LiBF_4$ in in ethylene carbonate (EC) and dimethyl carbonate (DMC) (3:7 by wt.) as electrolyte.

Galvanostatic cycling with potential limitation was performed using both a Basytec CTS-XL multichannel battery tester and a Biologic

VMP3 multichannel potentiostat at a C/n rate (expressed as 1 electron reacted in n hours per mole of LFMO). All the electrochemical tests were carried out at room temperature.

Scanning Electron Microscopy (SEM)

In **Chapter 4**, SEM has been used to analyze the morphology of the samples. For sample preparation, a small amount of powder was deposited on a carbon film and analyzed in a FEI Quanta 200 field-emission gun Scanning Electron Microscope (SEM). The SEM has been operated at low voltage (1 keV) and low current (50 pA) to protect the sample from the exposition to the electron beam and to achieve a high resolution at magnifications over 20 kX.

Mössbauer spectroscopy

In **Chapter 4**, Mössbauer spectroscopy was used for the characterization and quantification of antisite defects presented in the LFMO samples. ^{57}Fe Mössbauer spectroscopy was performed at the University of the Basque Country, Leioa, Bilbao in collaboration with Jose Javier Saiz Garitaonandia and Aitor Herrán Lopez. Measurements were done at room temperature in the transmission geometry using a conventional constant-acceleration spectrometer with a ^{57}Co-Rh source. Isomer shifts data are relative to α-Fe. The Mössbauer spectra were measured at 3 mm/s of velocity.

Mössbauer parameters of isomer shift (IS) and quadrupole splitting (QS), line width (WID) and iron percentage (%Fe) were determined by the fitting of the Mössbauer spectra with two doublet peaks. The doublets with highest IS, 0.34 mm/s, were assigned to Fe in octahedral position and the doublets with the smallest isomer shifts, 0.22 and 0.21 mm/s, were assigned to Fe in tetrahedral position for both samples. The percentage of each kind of iron was calculated by the ratio between the surface of both doublets.

Neutron Powder Diffraction (NPD)

In **Chapter 4**, NPD was used for the characterization and quantification of antisite defects presented in the LFMO samples. NPD of pristine LFMO samples have been carried out at D2B diffractometer at the Institute Laue-Langevin (ILL), Grenoble

France by Emmanuelle Suard. A wavelength of 1.5948 Å was used for the measurements. The samples were mounted on a 6mm diameter vanadium sample holder and placed on a carousel that allows automatic sample change. The neutron diffraction patterns were collected at RT with high statistics to enhance the data accuracy. Rietveld analysis was carried out using the FullProf suite[133,134]. A reference of $Na_2Ca_3Al_2F_{14}$ was previously measured to generate the IRF to extract the instrumental contribution.

In operando LFMO characterization

To study the structure and the oxidation states of the pristine samples and under in operando conditions in **Chapter 4**, PXRD, XAS and EXAFS experiments have been performed at the NOTOS beamline of ALBA synchrotron, Barcelona, Spain. These measurements have been performed thanks to the help and support from Carlos Escudero from ALBA and Marcus Fehse from CIC energiGUNE. Below, the experimental conditions and the data analysis followed is described. It is important to consider that the electrodes for the in operando experiments were performed as described before with the difference of a lower mass loading of around 6mg per electrode to fit the experimental requirements and the utilized cells were the specially designed in situ cells with Be windows recently described.[166]

In operando Dual-Edge X-ray Absorption Spectroscopy (XAS) and Powder X-Ray Diffraction (PXRD)

Quasi simultaneous PXRD and XAS data were conducted. PXRD was conducted at 11 KeV, this energy was selected to match good angular range within the geometrical limits of NOTOS beamline configuration. The cells were mounted on a 3 cells holder that were sequentially measured following a protocol that allowed to keep constant data acquisition frequency.

The PXRD measurements were recorded on a two-circle diffractometer equipped with a Mythen position sensitive detector (λ = 1.127640 Å) in the Bragg−Brentano geometry. The data for the LFMO were collected for 2θ angles from 9 to 53° with a step size of 0.06°. The software FullProfAPP was utilized for structural

analysis. A reference of LaB_6 was previously measured to generate the IRF to extract the instrumental contribution. The LaB_6 was refined from ICSD 40947.

XAS measurements at the Fe and Mn K-edge were performed in transmission mode. A focusing double-crystal silicon (311) monochromator was used. The beam size was adjusted to 0.6 × 0.6 mm2 (V × H). XAS spectra were continuously acquired alternating every 20 min during slow charge at C/10 and every 3min during fast discharge at C between the two transmission metal edges (Fe and Mn). For energy calibration TM reference foils placed between the second and third ionization chambers were used. During charge extended X-ray absorption fine structure (EXAFS) region data were acquired up to k = 11.9 $Å^{-1}$ for both edges.

In operando extended X-ray Absorption Fine Structure (EXAFS) Fitting

The Fourier transform of EXAFS oscillations with different k weights was performed in the k range from 2.5 Å to 10.9 Å–1 for Mn and Fe. The EXAFS spectra were fitted using the IFEFFIT software package. The Fourier transform of EXAFS oscillations with different k weights was performed in the k range from 2.5 Å to 10.9Å −1 for Fe. Fitting was performed in the R range from 1.0 to 3.5 Å (not phase corrected) by using k1, k2, and k3 weights. EXAFS amplitudes and phase shifts were calculated by the software package FEFF starting from the lattice parameters of the corresponding LFMO phase ICSD187271. Interatomic distances (R) and the Debye−Waller factors (σ2) were calculated for all paths included in the fits. Amplitude reduction factor and Enot were fitted and then fixed at 0.95 and -0.4, respectively. The coordination number of all three shells was kept at 6.

ANNEX I

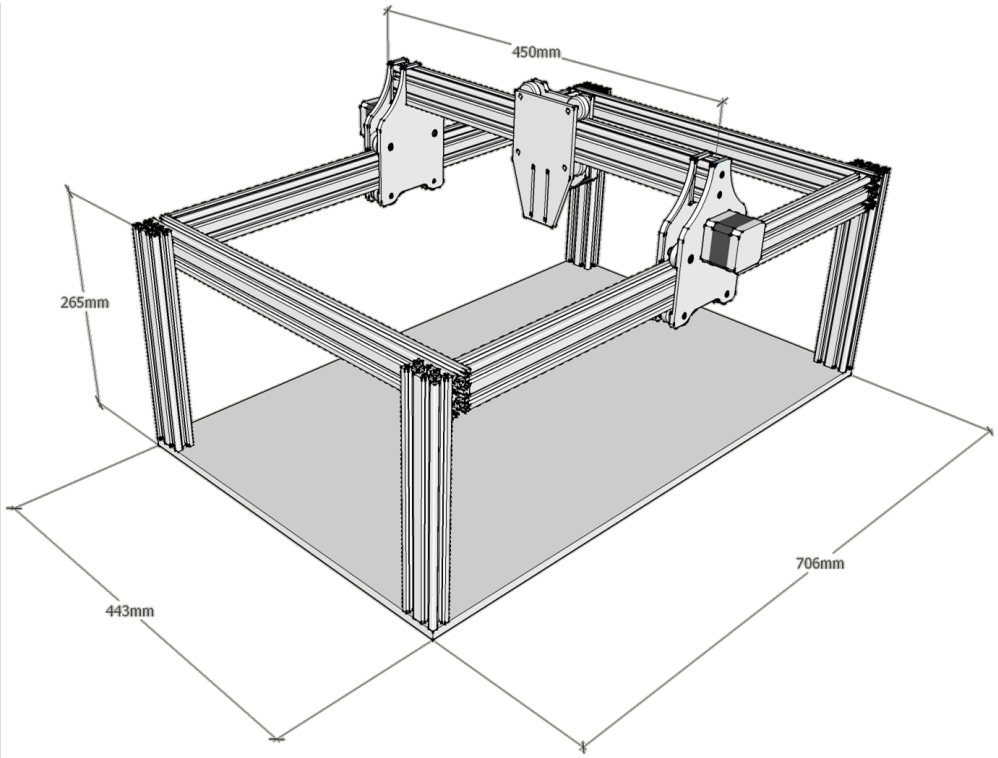

Figure 53: Design of the CNC table that integrates the Batteryino-I automated module. It contains 6 self-designed 3D printed pieces that serve to hold and attach the servo motors to the xy axis.

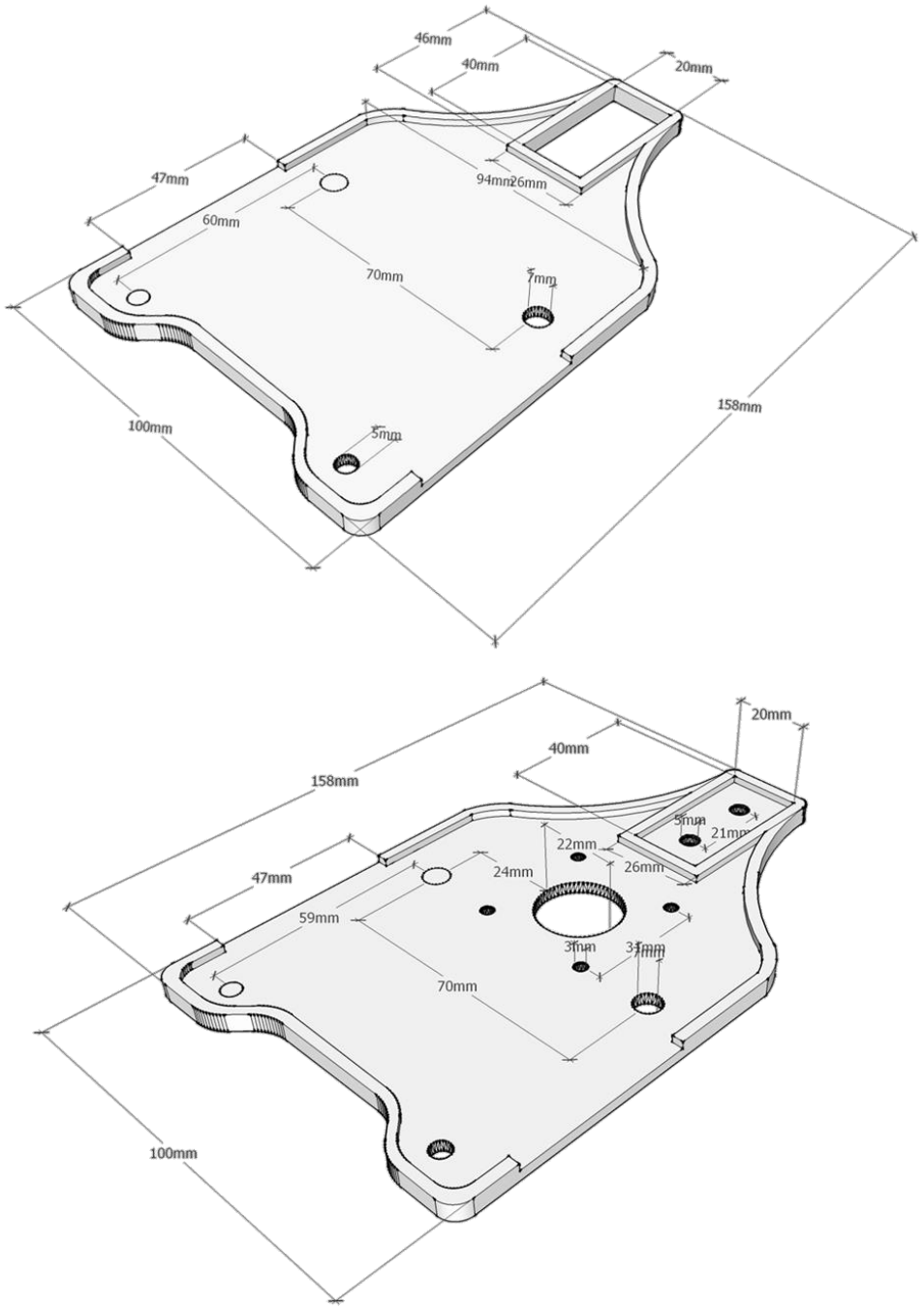

Figure 54: Design of the two homemade and 3D printed pieces that connect the servo motors of the x-axis of the CNC table that integrates the Batteryino-I automated module.

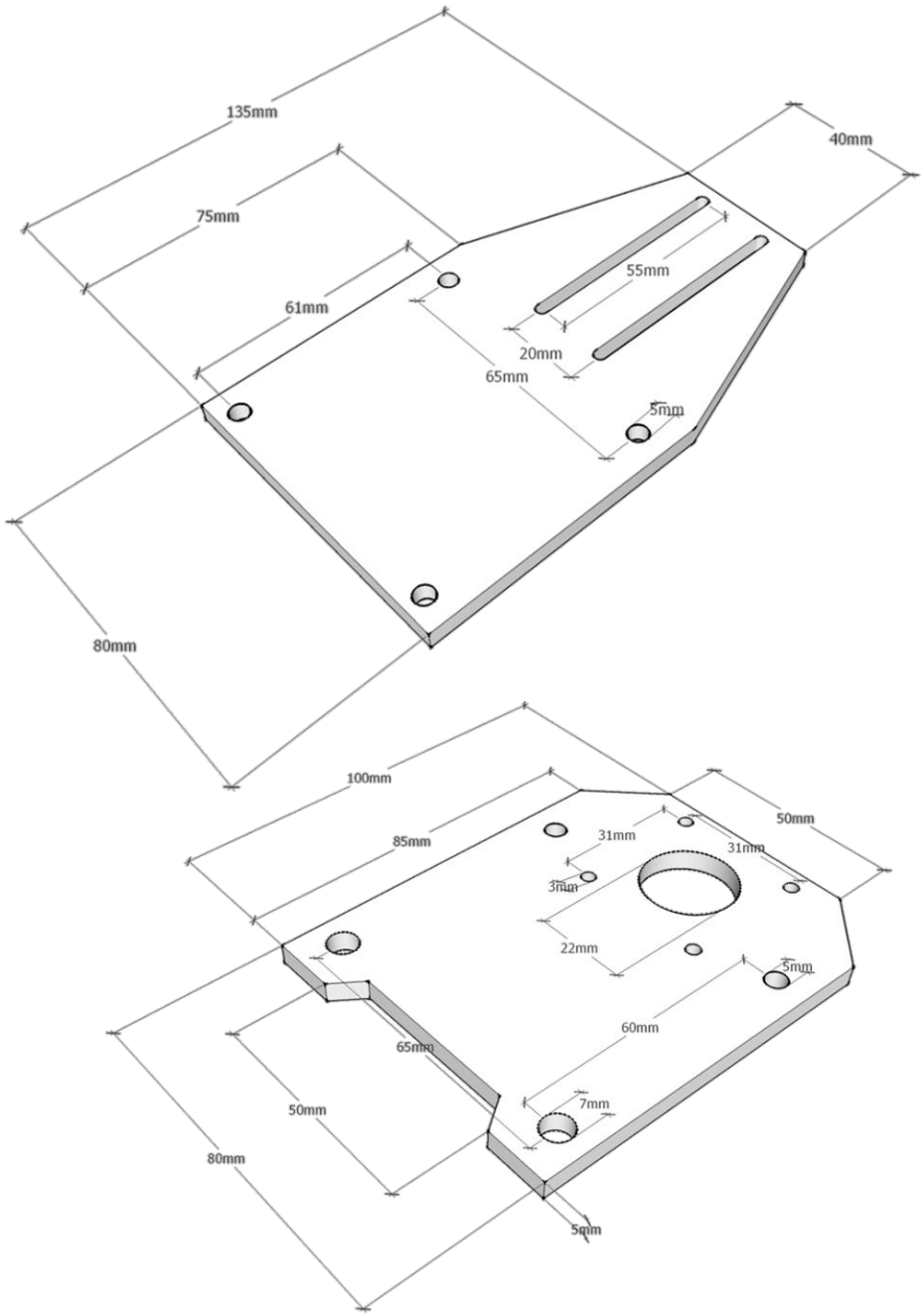

Figure 55: Design of the two homemade and 3D printed pieces that connect the servo motors of the y-axis of the CNC table that integrates the Batteryino-I automated module.

In the following lines the code, written in Arduino, for the automated module Batteryino-I is presented:

```
#include <MultiStepper.h>
#include <AccelStepper.h>
#include <Wire.h>            \\\\We include the library corresponding to the communication protocol between I2C devices. Necessary for simultaneous communication

#define Hipatia 1   \\\\We defined the I2C address for the different pumps
#define Bertozzi 2
#define Lise 03
#define Ada 04
#define Jane 05
#define Valentina 06
#define Alice 07
#define Grace 8
#define EN 8      /* Enable pin for all stepper outputs */

#define Y_DIR 6   /* Direction pin for Y axis */
#define Y_STEP 3  /* Step pin for Y axis */
#define X1_DIR 7   /* Direction pin for X1 axis */
#define X1_STEP 4  /* Step pin for X1 axis */
#define X2_DIR 5   /* Direction pin for X2 axis */
#define X2_STEP 2  /* Step pin for X2 axis */
#define A_DIR 13  /* Direction pin for Aux driver. Requires D13 and A-DIR pins to be shorted */
#define A_STEP 12 /* Direction pin for Aux driver. Requires D12 and A-STEP pins to be shorted */

#define motorInterfaceType 1

AccelStepper stepperY = AccelStepper(motorInterfaceType, Y_STEP, Y_DIR);
AccelStepper stepperX1 = AccelStepper(motorInterfaceType, X1_STEP, X1_DIR);
AccelStepper stepperX2 = AccelStepper(motorInterfaceType, X2_STEP, X2_DIR);
MultiStepper pareados;
// The volumes to be pumped for each specific set of samples is define in the following matrix where 'w' means an order of stirring 1min
String A[7][13] = {
//Crucibles   NULL    1   2   3   4   5   6   7   8   9   10    11    12
  /*NULL*/  {"0", "0", "0", "0", "0", "0", "0", "0", "0", "0", "0", "0", "0"},
  /*Patita-SAU-Li*/   {"0", "2.48", "2.48", "2.48", "2.48", "2.48", "2.48", "2.48", "2.48", "2.48", "2.48", "2.48", "2.48"},
  /*Ada-Fe4*/   {"0", "4.22", "4.22", "4.22", "4.22", "4.22", "4.22", "4.22", "4.22", "4.22", "4.22", "4.22", "4.22"},
  /*Jane-CA*/   {"0", "2.99", "2.99", "2.99", "2.99", "2.99", "2.99", "2.99", "2.99", "2.99", "2.99", "2.99", "2.99"},
  /*Valentina-EG*/  {"0", "0", "0", "0", "0", "0", "0", "0", "0", "0", "0", "0", "0"},
  /*Alice-Mn*/  {"0", "7.60", "7.60", "7.60", "7.60", "7.60", "7.60", "7.60", "7.60", "7.60", "7.60", "7.60", "7.60"},
  /*Grace-Fe8*/    {"0","W", "W", "W", "W", "W", "W", "W", "W", "W", "W", "W", "W"},
};


//The order of addition of reagents is specify in the following matrix
int O[7][13] = {
//Crucibles      0  1  2  3  4  5  6  7  8  9 10  11 12
  /*OrdenN0*/   {0, 0, 0, 0, 0, 0, 0, 0, 0, 0, 0, 0, 0},
  /*OrdenN1*/   {0, 3, 3, 3, 3, 3, 3, 3, 3, 3, 3, 3, 3},
  /*OrdenN2*/   {0, 7, 7, 7, 7, 7, 7, 7, 7, 7, 7, 7, 7},
  /*OrdenN3*/   {0, 4, 4, 4, 4, 4, 4, 4, 4, 4, 4, 4, 4},
  /*OrdenN4*/   {0, 8, 8, 8, 8, 8, 8, 8, 8, 8, 8, 8, 8},
  /*OrdenN5*/   {0, 5, 5, 5, 5, 5, 5, 5, 5, 5, 5, 5, 5},
  /*OrdenN6*/   {0, 6, 6, 6, 6, 6, 6, 6, 6, 6, 6, 6, 6},
};

// The x and y axis for each position are defined in the following matrix.
int p[16][2] = {
  //              X    Y
  /*ORIGEN*/     {0, 0},
  /*POSICIÓN1*/  {-1030, 280},
  /*POSICIÓN2*/  {-1030, 730},
  /*POSICIÓN3*/  {-1030, 1180},
  /*POSICIÓN4*/  {-1480, 280},
  /*POSICIÓN5*/  {-1480, 730},
  /*POSICIÓN6*/  {-1480, 1180},
  /*POSICIÓN7*/  {-1930, 280},
  /*POSICIÓN8*/  {-1930, 730},
  /*POSICIÓN9*/  {-1930, 1180},
  /*POSICIÓN10*/ {-2380, 280},
  /*POSICIÓN11*/ {-2380, 730},
  /*POSICIÓN12*/ {-2380, 1180},
  /*POSICIÓN13*/ {0, 0},
  /*POSICIÓN14*/ {0, 0},
  /*POSICIÓN15*/ {-350, 800},
};

String MixVolume = "15";                              // "MixVolume" defines the volumen of mixed reagents add to the crucibles
int WN;
String WashingVolume = "20";                          // 'WashingVolume' difines the volumen that would be used for washing the mixer.
String Washing2Volume = "25";                          //'WashingVolume' defines the volumen that would be pumped from the mixer to the waste water.
```

```
int y = 1;
float s = 0.00;
char computerdata[20];
byte received_from_computer = 0;
byte code = 0;                    //used to hold the I2C response code.
char pmp_data[20];                //we make a 20 byte character array to hold incoming data from the EZO-PMP.
byte in_char = 0;                 //used as a 1 byte buffer to store in bound bytes from the EZO-PMP.
byte i = 0;                       //counter used for pmp_data array.
int time_ = 250;                  //used to change the delay needed depending on the command sent to the EZO-PMP.


void setup() {            //  the system initialization is performed, this code will be run only once when starting the robot.

  Serial.begin(9600);

  Wire.begin();           //We initialize the I2C communication for its correct operation.
  /* Configure the steper drive pins as outputs */
  pinMode(EN, OUTPUT);
  pinMode(X2_DIR, OUTPUT);
  pinMode(X2_STEP, OUTPUT);
  pinMode(Y_DIR, OUTPUT);
  pinMode(Y_STEP, OUTPUT);
  pinMode(X1_DIR, OUTPUT);
  pinMode(X1_STEP, OUTPUT);
  pinMode(A_DIR, OUTPUT);
  pinMode(A_STEP, OUTPUT);

  /* Enable the X, Y, Z & Aux stepper outputs */
  digitalWrite(EN, LOW); //Low to enable

  stepperX1.setMaxSpeed(100.0);
  stepperX1.setAcceleration(1000.0);
  stepperX2.setMaxSpeed(100.0);
  stepperX2.setAcceleration(1000.0);


  stepperX2.setAcceleration(1000.0);

  stepperY.setMaxSpeed(150.0);
  stepperY.setAcceleration(150.0);
  pareados.addStepper(stepperX1);
  pareados.addStepper(stepperX2);

  Opciones();             //Execute the function 'Opciones' that shows the menu the first time that you initialize the program.
  //washing();             //When the program is initialized it automaticate wash the system.
}

void loop() {             //

  Menu();                 //Initialize the program menu where different options can be selected.
}


void Opciones() {

  Serial.println("|*************************|");
  Serial.println("|********|Batteryino|********|");
  Serial.println("|**|        Menu          |**|");
  Serial.println("|*************************|");
  Serial.println("");
  Serial.println("Select one of the following options:");
  Serial.println("1 STOP at the end of the actual synthesis");
  Serial.println("2 Safe position");
  Serial.println("3 Run complete synthesis cycle");
  Serial.println("4 Position tester");
  Serial.println("5 Mixer purge");
  Serial.println("6 Washing");
  Serial.println("12 Run complete synthesis cycle from synthesis nº2");
  Serial.println("13 Run complete synthesis cycle from synthesis nº3");
  Serial.println("14 Run complete synthesis cycle from synthesis nº4");
  Serial.println("15 Run complete synthesis cycle from synthesis nº5");
  Serial.println("16 Run complete synthesis cycle from synthesis nº6");
  Serial.println("17 Run complete synthesis cycle from synthesis nº7");
  Serial.println("18 Run complete synthesis cycle from synthesis nº8");
  Serial.println("19 Run complete synthesis cycle from synthesis nº9");
  Serial.println("20 Run complete synthesis cycle from synthesis nº10");
  Serial.println("21 Run complete synthesis cycle from synthesis nº11");
  Serial.println("22 Run complete synthesis cycle from synthesis nº12");
}
```

```
void Menu() {

  while (!Serial.available()) {}
  int i = Serial.parseInt();

  switch (i) {                                          //Depending on the option selected in the menu one option would start

    case 2:
      Serial.println("Safe position");
      posicion(15);
      break;
    case 3:
      Serial.println("Complete synthesis cycle");
      y = 1;
      accion();
      break;
    case 4:
      Serial.println("Position tester");
      delay(1000);
      Serial.println("");
      PosSelectionMenu();
      PosSelection();
      break;
    case 5:
      Serial.println("Purgin mixer");
      posicion(15);
      bombeo(Lagartija, WashingVolume);
      break;
    case 6:
      Serial.println("Washing");
      washing();
      break;
    case 12:
      Serial.println("Running from synthesis 2...");
      y = 2;                                            //la funcion "accion".
      accion();
      break;

    case 13:
      Serial.println("Running from synthesis 3...");
      y = 3;
      accion();
      break;
    case 14:
      Serial.println("Running from synthesis 4...");
      y = 4;
      accion();
      break;
    case 15:
      Serial.println("Running from synthesis 5...");
      y = 5;
      accion();
      break;
    case 16:
      Serial.println("Running from synthesis 6...");
      y = 6;
      accion();
      break;
    case 17:
      Serial.println("Running from synthesis 7...");
      y = 7;
      accion();
      break;
    case 18:
      Serial.println("Running from synthesis 8...");
      y = 8;
      accion();
      break;
    case 19:
      Serial.println("Running from synthesis 9...");
      y = 9;
      accion();
      break;
    case 20:
      Serial.println("Running from synthesis 10...");
      y = 10;
      accion();
```

```
      y = 10;
      accion();
      break;
    case 21:
      Serial.println("Running from synthesis 11...");
      y = 11;
      accion();
      break;
    case 22:
      Serial.println("Running from synthesis 12...");
      y = 12;
      accion();
      break;

  }
  Opciones();
}

void PosSelectionMenu() {

  Serial.println("Please, select the position you want to try:");
  Serial.println("Possible options:");
  Serial.println("");
  Serial.println("1. Pos 1");
  Serial.println("2. Pos 2");
  Serial.println("3. Pos 3");
  Serial.println("4. Pos 4");
  Serial.println("5. Pos 5");
  Serial.println("6. Pos 6");
  Serial.println("7. Pos 7");
  Serial.println("8. Pos 8");
  Serial.println("9. Pos 9");
  Serial.println("10. Pos 10");
  Serial.println("11. Pos 11");
  Serial.println("12. Pos 12");
  Serial.println("15. Pos 15 (waste)");
  Serial.println("100. Pos 0 (origin)");
}

void PosSelection() {
  int PS = 0;
  while (PS == 0) {
    PS = Serial.parseInt();
  }
  switch (PS) {

    case 1:

      Serial.println("\nTrying position 1");
      posicion(1);
      delay(1500);
      posicion(0);
      break;

    case 2:

      Serial.println("\nTrying position 2");
      posicion(2);
      delay(1500);
      posicion(0);
      break;

    case 3:

      Serial.println("\nTrying position 3");
      posicion(3);
      delay(1500);
      posicion(0);
      break;

    case 4:

      Serial.println("\nTrying position 4");
      posicion(4);
      delay(1500);
      posicion(0);
      break;

```

```
307     case 5:
308
309       Serial.println("\nTrying position 5");
310       posicion(5);
311       delay(1500);
312       posicion(0);
313       break;
314
315     case 6:
316
317       Serial.println("\nTrying position 6");
318       posicion(6);
319       delay(1500);
320       posicion(0);
321       break;
322
323     case 7:
324
325       Serial.println("\nTrying position 7");
326       posicion(7);
327       delay(1500);
328       posicion(0);
329       break;
330
331     case 8:
332
333       Serial.println("\nTrying position 8");
334       posicion(8);
335       delay(1500);
336       posicion(0);
337       break;
338
339     case 9:
340
341       Serial.println("\nTrying position 9");
342       posicion(9);
343       delay(1500);
344       posicion(0);
345       break;
346
347     case 10:
348
349       Serial.println("\nTrying position 10");
350       posicion(10);
351       delay(1500);
352       posicion(0);
353       break;
354
355     case 11:
356
357       Serial.println("\nTrying position 11");
358       posicion(11);
359       delay(1500);
360       posicion(0);
361       break;
362
363     case 12:
364
365       Serial.println("\nTrying position 12");
366       posicion(12);
367       delay(1500);
368       posicion(0);
369       break;
370
371     case 15:
372
373       Serial.println("\nTrying position 15 (waste)");
374       posicion(15);
375       delay(1500);
376       posicion(0);
377       break;
378
379     case 100:
380
```

```
      Serial.println("\nTrying position 0 (origin)");
      posicion(0);
      delay(1500);
      posicion(0);
      break;

    default:

      Serial.println("\nNo pump selected. Try to select again. \n\n");
  }
  delay(1000);

}

void accion() {

  while (y < 13) {
    posicion(15);
    for (int x = 1; x < 7; x++) {
      delay(1000);
      bombeo(O[x][y], A[(O[x][y])-2][y]);
    }
    delay(20000);                    //Stirring
    bombeo(Lagartija, "22");         //Purge volume
    posicion(0);                 //CNC table goes to position 1 to avoid decalibration and make it safer.
    delay(1000);
    posicion(y);                 //CNC table moves to 'y' position
    delay(1000);
    bombeo(Lagartija, MixVolume);   //The mixed of reagents is pumped in position 'y'
    posicion(0);
    delay(1000);
    posicion(15);
    washing();                       //The system is washed before starting the next position

    y++;                             //Y is increased to execute the next position
    /*while (!Serial.available()) {}
    int i = Serial.parseInt();
    switch (i) {
      case 1:

      Serial.println("Stopped");
      y = 999;
          break;

   }*/
  }
  y=1;                          //Una vez salimos del bucle while, "y" se reinicia.
}

void bombeo(int bomba, String volumen) {

  Wire.beginTransmission(bomba);
  Wire.write("d,");
  Wire.write(volumen.c_str());
  Wire.endTransmission();

  if (volumen=="W"){

    delay(60000);

    }

  while (s < volumen.toFloat()) {
    for (i = 0; i <= received_from_computer; i++) {                          //set all char to lower case, this is just so this exact
sample code can recognize the "sleep" command.
      computerdata[i] = tolower(computerdata[i]);
    }
    i = 0;                                                                   //reset i, we will need it later

    Wire.beginTransmission(bomba);                                        //call the device by its ID number.
    Wire.write("r");                                                    //transmit the command that was sent through the serial port.
    Wire.endTransmission();                                                  //end the I2C data transmission.

    if (strcmp("r", "sleep") != 0) {                                    //if the command that has been sent wait the correct amount of time
and request data.

      delay(time_);                                                          //wait the correct amount of time for the device to complete
its instruction.

```

```
      Wire.requestFrom(bomba, 20, 1);                                    //call the device and request 20 bytes (this may be more than we need)
      code = Wire.read();                                                  //the first byte is the response code, we read this separately.
    }

    while (Wire.available()) {          //are there bytes to receive.
      in_char = Wire.read();            //receive a byte.
      pmp_data[i] = in_char;            //load this byte into our array.
      i += 1;                           //incur the counter for the array element.
      if (in_char == 0) {
        i = 0;                          //reset the counter i to 0.
        break;                          //exit the while loop.
      }
    }
    s = atof(pmp_data);
    Serial.println(s);          //print the data.
  }
  s = 0;
}
void washing () {

  posicion(15); //Position 15 is set as waste water position and it is connected with a jerrycan of waste.

  WN =  4; // WN = número de lavados

  while (WN > 0) {

    bombeo(Conejillo, WashingVolume);
    bombeo(Lagartija, Washing2Volume);

    WN--;
  }

}

void movimientoinfinito() {

  for (int i = 0; i < 13; i++) {


    stepperX1.moveTo(p[i][0]);
    stepperX2.moveTo(p[i][0]);
    pareados.runSpeedToPosition();
    stepperY.runToNewPosition(p[i][1]);

    delay(3000);

    stepperX1.moveTo(p[0][0]);
    stepperX2.moveTo(p[0][0]);
    pareados.runSpeedToPosition();
    stepperY.runToNewPosition(p[0][1]);

  }
}

void posicion(int posicion) {

  stepperX1.moveTo(p[posicion][0]);
  stepperX2.moveTo(p[posicion][0]);
  pareados.runSpeedToPosition();
  stepperY.runToNewPosition(p[posicion][1]
}
```

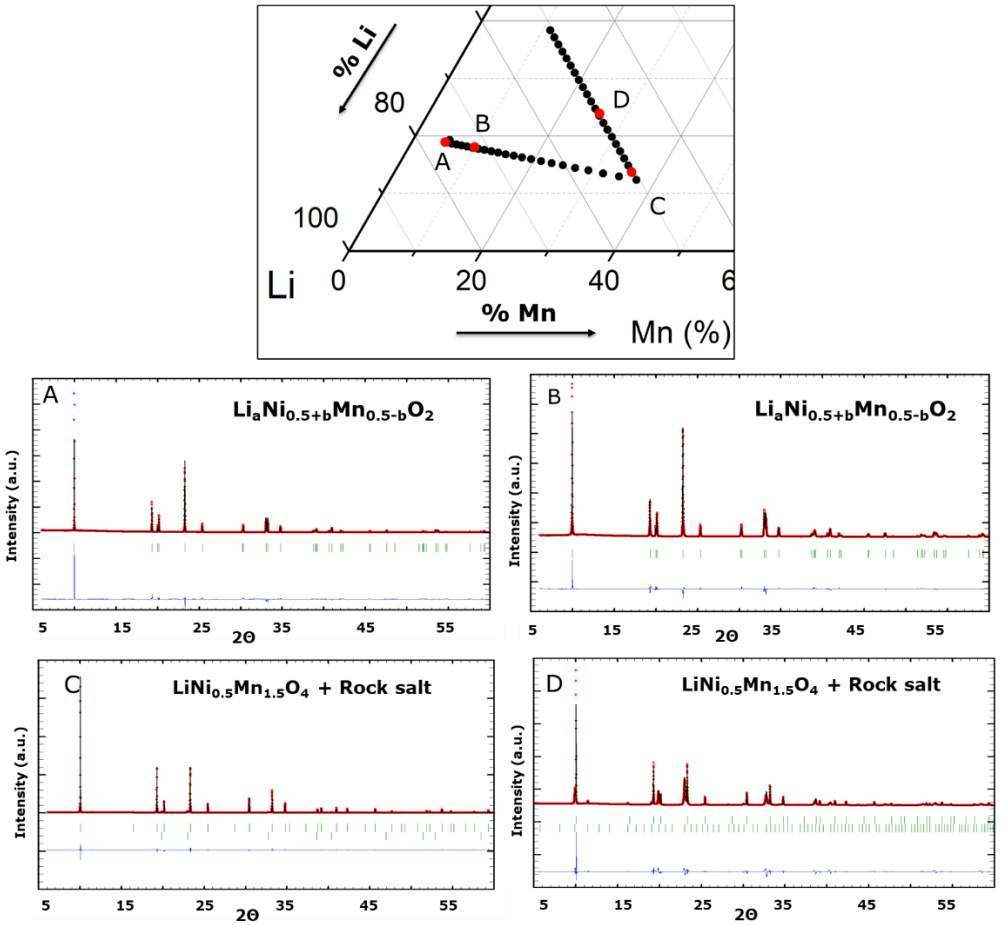

Figure 56: Pseudo-Rietveld refinements corresponding to the A, B, C and D points in the pseudo-ternary phase diagram. In green the Bragg positions, in black the calculated XRD pattern, in red the observed pattern is represented and, in blue the difference between observed and calculated is shown. Note that rock-salts were refined in Le Bail mode as their exact composition is unknown. The structural models used for the refinements correspond to LNMO (ICSD90650), Rock-salt (ICSD646099), $Li_aNi_{0.5+b}Mn_{0.5-b}O_2$ (COD4002582).

Conventional Pseudo-Rietveld R-factors	**Li-Ni-Mn oxides**					
Sample Name	**A**	**B**	**C-1st phase**	**C-2nd phase**	**D-1st phase**	**D-2nd phase**
Space group	*R*-3*m*	*R*-3*m*	*Fd*-3*m*	*Fd*-3*m*	*Fd*-3*m*	*Fd*-3*m*
Rp	20.5	15	9.70		25.2	
Rwp	21.7	16.3	11.7		29.4	
Rexp	2.32	1.24	1.17		1.98	
RBragg	16.70	8.88	2.91	2.23	8.12	0.83
Rf	7.32	5.06	2.66	2.37	4.98	2.02
χ^2 (Bragg)	88	175	100		220	

Table 28: Conventional Rietveld factors for the pseudo-Rietveld refinements of the 4 selected samples A,B,C and D of the studied-pseudo ternary Li-Ni-Mn phase diagram samples synthesized using the automated module Batteryino-I. Note that rock-salts were index in Le Bail mode as their exact composition is unknown.

Unit cell	**Li-Ni-Mn oxides**					
Sample Name	**A**	**B**	**C-1st phase**	**C-2nd phase**	**D-1st phase**	**D-2nd phase**
Cell par. *a* (Å)	2.8859(3)	2.8893(3)	8.1728(3)	8.28(2)	8.1694(9)	8.2758(3)
Cell par. *b* (Å)	2.8859(3)	2.8893(3)	8.1728(3)	8.28(2)	8.1694(9)	8.2758(3)
Cell par. *c* (Å)	14.261(3)	14.276(3)	8.1728(3)	8.28(2)	8.1694(9)	8.2758(3)
Volume (Å^3)	102.86(3)	103.21(3)	545.90(3)	569.3(3)	545.2(12)	566.813(3)

Table 29: Unit cell parameters and volume for the pseudo-Rietveld refinements of the 4 samples of the studied-pseudo ternary Li-Ni-Mn phase diagram samples synthesized using the automated module Batteryino-I. Note that rock-salts were index in Le Bail mode as their exact composition is unknown.

ANNEX II

Supercell numerator	Volume	Formula units	Cell parameters			KPOINT
1	1	4	0.00	4.13	-4.13	4
			0.00	4.13	4.13	4
			8.25	0.00	0.00	3
2	2	8	0.00	-4.13	4.13	4
			8.25	0.00	0.00	3
			0.00	8.25	8.25	2
3	2	8	0.00	-4.13	4.13	4
			8.25	4.13	4.13	2
			-8.25	4.13	4.13	2
4	2	8	0.00	4.13	-4.13	4
			0.00	4.13	4.13	4
			16.50	0.00	0.00	2
5	2	8	0.00	0.00	-8.25	3
			0.00	8.25	0.00	3
			8.25	-4.13	4.13	2
6	2	8	8.25	0.00	0.00	3
			0.00	8.25	0.00	3
			0.00	0.00	8.25	3
7	3	12	0.00	4.13	-4.13	4
			0.00	4.13	4.13	4
			24.75	0.00	0.00	1
8	3	12	0.00	-8.25	0.00	3
			8.25	4.13	4.13	2
			-8.25	0.00	8.25	2
9	3	12	0.00	-4.13	4.13	4
			8.25	0.00	0.00	3
			0.00	12.38	12.38	2
10	3	12	0.00	0.00	8.25	3
			8.25	4.13	-4.13	2
			-8.25	8.25	0.00	2
11	3	12	0.00	0.00	-8.25	3
			-8.25	4.13	4.13	2
			8.25	8.25	0.00	2
12	3	12	0.00	-8.25	0.00	3
			8.25	0.00	0.00	3
			0.00	4.13	12.38	2
13	3	12	0.00	4.13	-4.13	4
			-8.25	4.13	4.13	2
			8.25	8.25	8.25	2

Table 30: K points-grid for each supercell.

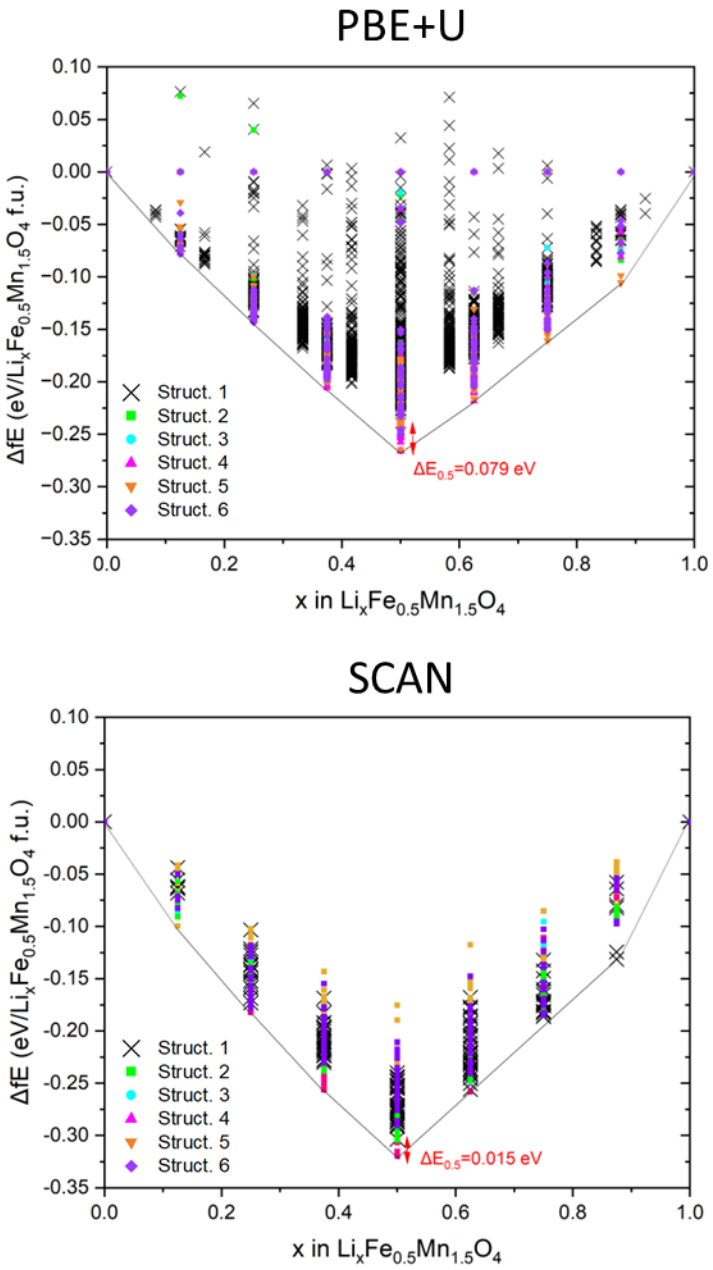

Figure 57: Formation energy (in eV/$Li_xFe_{0.5}$ $Mn_{1.5}O_4$ per formula unit) as a function of Li content for the 6 selected Fe/Mn distributions calculated using PBE+U (top) and SCAN (bottom) functionals. The difference in between the maximum and minimum energy for the ground states of the different Fe/Mn distributions at x=0.5 is indicated.

x in LixMn1.5Fe0.5O4														
0		0.125		0.25		0.5		0.75		0.875		1		
Atom	Bader charge	Atom	Bader charge	Atom	Bader charge	Atom	Bader charge	Atom	Bader charge	Atom	Bader charge	Atom	Bader charge	
O	-0.91	O	-0.94	O	-0.95	O	-0.96	O	-1.02	O	-1.12	O1	-1.14	
O	-0.92	O	-1.07	O	-1.06	O	-1.05	O	-1.11	O	-1.16	O2	-1.15	
O	-0.90	O	-0.93	O	-0.92	O	-0.89	O	-1.15	O	-1.08	O3	-1.10	
O	-0.91	O	-0.92	O	-0.92	O	-1.04	O	-1.09	O	-1.13	O4	-1.13	
O	-0.90	O	-0.91	O	-0.89	O	-0.98	O	-1.08	O	-1.05	O5	-1.12	
O	-0.91	O	-0.91	O	-0.91	O	-1.15	O	-1.08	O	-1.07	O6	-1.17	
O	-0.91	O	-0.91	O	-1.04	O	-0.98	O	-0.95	O	-0.96	O7	-1.13	
O	-0.92	O	-0.92	O	-0.91	O	-1.16	O	-0.92	O	-1.12	O8	-1.16	
O	-0.93	O	-1.09	O	-0.91	O	-1.10	O	-1.09	O	-1.10	O9	-1.12	
O	-0.92	O	-0.89	O	-1.09	O	-0.98	O	-1.09	O	-1.11	O10	-1.16	
O	-0.89	O	-0.92	O	-0.95	O	-1.06	O	-1.09	O	-1.18	O11	-1.08	
O	-0.92	O	-0.95	O	-0.95	O	-0.97	O	-1.08	O	-1.17	O12	-1.13	
O	-0.90	O	-0.96	O	-0.95	O	-0.91	O	-1.10	O	-1.13	O13	-1.08	
O	-0.90	O	-0.91	O	-0.96	O	-1.07	O	-1.11	O	-1.14	O14	-1.09	
O	-0.88	O	-0.93	O	-1.12	O	-0.96	O	-0.98	O	-1.05	O15	-1.10	
O	-0.90	O	-0.94	O	-0.95	O	-1.06	O	-1.18	O	-1.17	O16	-1.07	
		O	-0.92	O	-0.94			O	-1.16	O	-1.09			
		O	-0.97	O	-0.97			O	-1.17	O	-1.12			
		O	-1.10	O	-0.94			O	-1.02	O	-1.15			
		O	-0.92	O	-1.10			O	-0.96	O	-1.14			
		O	-0.90	O	-1.04			O	-1.11	O	-0.91			
		O	-0.91	O	-0.89			O	-1.16	O	-1.08			
		O	-0.94	O	-0.95			O	-1.16	O	-1.11			
		O	-0.91	O	-0.90			O	-1.17	O	-1.15			
		O	-0.91	O	-0.89			O	-1.11	O	-1.07			
		O	-0.92	O	-0.90			O	-1.12	O	-1.09			
		O	-0.96	O	-0.94			O	-1.10	O	-1.12			
		O	-0.92	O	-1.06			O	-1.15	O	-0.98			
		O	-1.09	O	-1.08			O	-0.99	O	-1.12			
		O	-0.91	O	-0.91			O	-1.12	O	-1.09			
		O	-0.92	O	-0.92			O	-1.09	O	-1.08			
		O	-0.90	O	-0.92			O	-1.06	O	-1.07			
								O	-1.09					
								O	-0.97					
								O	-1.01					
								O	-1.15					
								O	-1.08					
								O	-0.92					
								O	-0.92					
								O	-1.12					
								O	-1.10					
								O	-1.10					
								O	-1.10					
								O	-1.11					
								O	-0.97					
								O	-1.05					
								O	-1.09					
								O	-1.05					

Table 31: Bader charges of O calculated via PBE+U for the structure 1.

x in LixFe0.5Mn1.5O4												
0		0.125		0.25		0.5		0.75		0.875		1	
Atom	Bader charge	Atom	Bader charge	Atom	Bader charge	Atom	Bader charge	Atom	Bader charge	Atom	Bader charge	Atom	Bader charge
O	-0.92	O	-0.98	O	-0.97	O	-0.97	O	-1.05	O	-1.13	O	-1.10
O	-0.95	O	-1.10	O	-1.06	O	-1.09	O	-1.13	O	-1.18	O	-1.14
O	-0.96	O	-0.98	O	-0.94	O	-0.93	O	-1.14	O	-1.12	O	-1.08
O	-0.97	O	-0.95	O	-0.95	O	-1.07	O	-1.16	O	-1.17	O	-1.08
O	-0.94	O	-0.94	O	-0.93	O	-1.00	O	-1.10	O	-1.10	O	-1.11
O	-0.94	O	-0.96	O	-0.94	O	-1.16	O	-1.11	O	-1.12	O	-1.24
O	-0.93	O	-0.96	O	-1.06	O	-0.99	O	-0.97	O	-1.01	O	-1.10
O	-0.92	O	-0.96	O	-0.94	O	-1.15	O	-0.96	O	-1.15	O	-1.15
O	-0.93	O	-1.12	O	-0.94	O	-1.11	O	-1.09	O	-1.13	O	-1.16
O	-0.94	O	-0.91	O	-1.11	O	-0.99	O	-1.10	O	-1.12	O	-1.10
O	-0.94	O	-0.91	O	-0.95	O	-1.09	O	-1.12	O	-1.18	O	-1.09
O	-0.92	O	-0.97	O	-0.97	O	-0.99	O	-1.09	O	-1.18	O	-1.12
O	-0.95	O	-1.00	O	-0.95	O	-0.97	O	-1.17	O	-1.15	O	-1.10
O	-0.93	O	-0.92	O	-0.99	O	-1.08	O	-1.14	O	-1.17	O	-1.14
O	-0.94	O	-0.90	O	-1.12	O	-0.98	O	-1.00	O	-1.05	O	-1.11
O	-0.94	O	-0.97	O	-0.95	O	-1.08	O	-1.17	O	-1.20	O	-1.13
		O	-0.90	O	-0.95			O	-1.17	O	-1.12		
		O	-0.98	O	-0.98			O	-1.18	O	-1.12		
		O	-1.11	O	-0.95			O	-1.05	O	-1.18		
		O	-0.91	O	-1.11			O	-1.05	O	-1.17		
		O	-0.94	O	-1.06			O	-1.12	O	-0.96		
		O	-0.95	O	-0.93			O	-1.17	O	-1.13		
		O	-0.98	O	-0.97			O	-1.17	O	-1.13		
		O	-0.95	O	-0.94			O	-1.18	O	-1.17		
		O	-0.94	O	-0.94			O	-1.14	O	-1.11		
		O	-0.97	O	-0.95			O	-1.13	O	-1.14		
		O	-1.02	O	-0.98			O	-1.12	O	-1.13		
		O	-0.93	O	-1.09			O	-1.13	O	-1.03		
		O	-1.10	O	-1.10			O	-1.05	O	-1.13		
		O	-0.95	O	-0.94			O	-1.14	O	-1.12		
		O	-0.97	O	-0.96			O	-1.16	O	-1.11		
		O	-0.94	O	-0.95			O	-1.09	O	-1.12		
								O	-1.09				
								O	-1.01				
								O	-1.00				
								O	-1.17				
								O	-1.12				
								O	-0.97				
								O	-0.97				
								O	-1.14				
								O	-1.13				
								O	-1.13				
								O	-1.13				
								O	-1.13				
								O	-1.01				
								O	-1.13				
								O	-1.09				
								O	-1.12				

Table 32: Bader charges of O calculated via scan for the structure 1.

ANNEX III

Code	Position	Li excess	time gel formation (h)	Temperature heating ramp (°C/min)	Temperature annealing (°C)	time annealing (h)	Temperature cooling ramp (°C/min)	Purity	Cell parameter (Å)
158	a1	0.02	NR	5	900	10	NR	yes	8.2936
162	b1	0.02	NR	5	900	10	NR	yes	8.2841
166	c1	0.02	NR	5	900	10	NR	yes	8.2944
159	a2	0.02	NR	5	900	10	NR	yes	8.2889
163	b2	0.02	NR	5	900	10	NR	yes	8.2915
167	c2	0.02	NR	5	900	10	NR	No	8.2723
160	a3	0.02	NR	5	900	10	NR	No	8.2757
164	b3	0.02	NR	5	900	10	NR	No	8.2794
168	c3	0.02	NR	5	900	10	NR	No	8.2779
161	a4	0.02	NR	5	900	10	NR	No	8.2728
165	b4	0.02	NR	5	900	10	NR	yes	8.2856
169	c4	0.02	NR	5	900	10	NR	No	8.2732
37	a1	0.02	NR	5	700	5	NR	No	8.2679
42	b2	0.02	NR	5	700	7.5	NR	No	8.2726
43	b3	0.02	NR	5	700	10	NR	No	8.2718
38	a2	0.02	NR	5	800	5	NR	No	8.2744
41	b1	0.02	NR	5	800	7.5	NR	yes	8.2722
44	b4	0.02	NR	5	800	10	NR	yes	8.2967
39	a3	0.02	NR	5	900	5	NR	yes	8.2840
40	a4	0.02	NR	5	900	7.5	NR	yes	8.2944
45	c1	0.02	NR	5	900	10	NR	yes	8.2833
74	a2	0.02	NR	5	800	5	NR	yes	8.2714
75	a3	0.03	NR	5	800	5	NR	No	8.2777
76	a4	0.04	NR	5	800	5	NR	yes	8.2790
78	b2	0.02	NR	5	900	10	NR	yes	8.2734
79	b3	0.03	NR	5	900	10	NR	yes	8.2749
80	b4	0.04	NR	5	900	10	NR	no	8.2771
170	a1	0.02	NR	5	900	10	NR	yes	8.2951
171	a2	0.02	NR	5	900	10	NR	yes	8.2919
172	a3	0.02	NR	5	900	10	NR	yes	8.2780
173	a4	0.02	NR	5	900	10	NR	yes	8.2785
257	c4	0.04	5.5	1	800	7.5	NR	yes	8.2693
258	a1	0.08	5	2.5	850	7.5	NR	no	8.2878
259	a2	0.04	5	2.5	850	7.5	NR	no	8.2916
260	a3	0.06	3	2.5	850	7.5	NR	no	8.2916
261	a4	0.06	5.5	2.5	850	7.5	NR	no	8.2883
262	b1	0.08	5.5	2.5	850	7.5	NR	no	8.2840
263	b2	0	5.5	2.5	850	7.5	NR	no	8.2954
264	b3	0.02	4.5	2.5	850	7.5	NR	no	8.2898
134	a1	0.02	0	5	900	10	NR	yes	8.2657
308	b2	0.02	4.50	5.00	900.00	10.00	5.00	no	8.2607
309	a1	0.02	NR	5.00	800.00	10.00	5.00	yes	8.2637
310	a2	0.02	NR	5.00	800.00	10.00	5.00	yes	8.2996
311	a3	0.02	NR	5.00	800.00	10.00	5.00	yes	8.2866
312	a4	0.02	NR	5.00	800.00	10.00	5.00	yes	8.2872
313	b1	0.02	NR	5.00	800.00	10.00	5.00	yes	8.2933
314	b2	0.02	NR	5.00	800.00	10.00	5.00	yes	8.2992
315	b3	0.02	NR	5.00	800.00	10.00	5.00	yes	8.2871
316	b4	0.02	NR	5.00	800.00	10.00	5.00	yes	8.2937
317	c1	0.02	NR	5.00	800.00	10.00	5.00	yes	8.2892
318	c2	0.02	NR	5.00	800.00	10.00	5.00	yes	8.2837
319	c3	0.02	NR	5.00	800.00	10.00	5.00	yes	8.2883
320	c4	0.02	NR	5.00	800.00	10.00	5.00	yes	8.2831
321	a1	0.02	3.00	5.00	800.00	10.00	5.00	yes	8.2955
322	a2	0.02	3.00	5.00	800.00	10.00	5.00	yes	8.2738
323	a3	0.02	3.00	5.00	800.00	10.00	5.00	yes	8.2902
324	a4	0.02	3.00	5.00	800.00	10.00	5.00	yes	8.2998
347	a3	0.02	4.00	5.00	900.00	10.00	5.00	No	8.3151
348	a4	0.02	4.00	5.00	900.00	10.00	5.00	yes	8.2730
349	b1	0.02	4.00	5.00	900.00	10.00	5.00	yes	8.2739
325	b1	0.02	3.00	5.00	800.00	10.00	5.00	yes	8.2814
326	b2	0.02	3.00	5.00	800.00	10.00	5.00	yes	8.2693
327	b3	0.02	3.00	5.00	800.00	10.00	5.00	yes	8.2970
328	b4	0.02	3.00	5.00	800.00	10.00	5.00	yes	8.2804
329	c1	0.02	3.00	5.00	800.00	10.00	5.00	yes	8.2767
331	c3	0.02	3.00	5.00	800.00	10.00	5.00	No	8.3013
332	c4	0.02	3.00	5.00	800.00	10.00	5.00	yes	8.2855
333	a1	0.02	4.50	5.00	900.00	10.00	5.00	No	8.2658
341	c1	0.02	4.50	5.00	900.00	10.00	5.00	yes	8.2651

306	b2	0.02	4.50	5.00	900.00	10.00	5.00	no	8.2622
344	c4	0.02	4.50	5.00	900.00	10.00	5.00	yes	8.2782
345	a1	0.02	4.00	5.00	900.00	10.00	5.00	yes	8.2643
337	b1	0.02	4.50	5.00	900.00	10.00	5.00	yes	8.2726
338	b2	0.02	4.50	5.00	900.00	10.00	5.00	yes	8.2759
359	b2	0.02	4.00	5.00	700.00	10.00	5.00	yes	8.2673
360	a2	0.02	4.00	5.00	700.00	10.00	5.00	yes	8.2656
361	b2	0.02	4.00	5.00	700.00	10.00	5.00	yes	8.2557
362	a2	0.02	4.00	5.00	700.00	10.00	5.00	yes	8.2529
334	a2	0.02	4.50	5.00	900.00	10.00	5.00	yes	8.2673
246	a1	0.08	4	1	800	7.5	NR	no	8.2760
247	a2	0.06	5.5	1	800	7.5	NR	no	8.2753
248	a3	0	3	1	800	7.5	NR	no	8.2769
249	a4	0.08	5.5	1	800	7.5	NR	no	8.2679
250	b1	0.06	3	1	800	7.5	NR	no	8.2719
251	b2	0	5.5	1	800	7.5	NR	yes	8.2779
252	b3	0.06	3.5	1	800	7.5	NR	yes	8.2712
253	b4	0	3.5	1	800	7.5	NR	no	8.2748
254	c1	0.08	4	1	800	7.5	NR	no	8.2711
255	c2	0.02	4	1	800	7.5	NR	no	8.2762
256	c3	0.08	3	1	800	7.5	NR	no	8.2730
265	b4	0	3	2.5	850	7.5	NR	no	8.2863
266	c1	0.08	5	2.5	850	7.5	NR	no	8.2915
282	a1	0.04	5.5	2.50	750	7.5	2.00	yes	8.2622
307	b2	0.02	4.50	5.00	900.00	10.00	5.00	yes	8.2831
335	a3	0.02	4.50	5.00	900.00	10.00	5.00	yes	8.2889
336	a4	0.02	4.50	5.00	900.00	10.00	5.00	yes	8.2866
283	a2	0.04	4.5	2.50	750	7.5	2.00	yes	8.2625
267	c2	0.02	5	2.5	850	7.5	NR	no	8.2926
268	c3	0.02	5	2.5	850	7.5	NR	no	8.2901
269	c4	0.08	5	2.5	850	7.5	NR	no	8.2848
339	b3	0.02	4.50	5.00	900.00	10.00	5.00	No	8.2831
340	b4	0.02	4.50	5.00	900.00	10.00	5.00	yes	8.2852
342	c2	0.02	4.50	5.00	900.00	10.00	5.00	yes	8.2835
343	c3	0.02	4.50	5.00	900.00	10.00	5.00	yes	8.2824
346	a2	0.02	4.00	5.00	900.00	10.00	5.00	yes	8.2877
270	a1	0.08	5.5	1	850	5	2.00	yes	8.2848
271	a2	0.08	5	1	850	5	2.00	yes	8.2697
272	a3	0.06	4.5	1	850	5	2.00	yes	8.2855
273	a4	0.08	5	1	850	5	2.00	no?	8.2800
351	b3	0.02	4.00	5.00	900.00	10.00	5.00	yes	8.2882
352	b4	0.02	4.00	5.00	900.00	10.00	5.00	yes	8.2879
354	c2	0.02	4.00	5.00	900.00	10.00	5.00	yes	8.2932
355	c3	0.02	4.00	5.00	900.00	10.00	5.00	yes	8.2839
356	c4	0.02	4.00	5.00	900.00	10.00	5.00	yes	8.2883
274	b1	0.04	4	1	850	5	2.00	yes?	8.2718
275	b2	0.08	5	1	850	5	2.00	no	8.2782
276	b3	0.08	3.5	1	850	5	2.00	yes	8.2772
277	b4	0.08	3.5	1	850	5	2.00	yes	8.2694
278	c1	0.04	5.5	1	850	5	2.00	yes	8.2832
279	c2	0	3	1	850	5	2.00	no	8.2929
280	c3	0.04	5	1	850	5	2.00	yes	8.2890
281	c4	0.04	3.5	1	850	5	2.00	yes	8.2861
284	a3	0.04	4	2.50	750	7.5	2.00	yes	8.2619
285	a4	0.04	4	2.50	750	7.5	2.00	yes	8.2585
286	b1	0.02	4.5	2.50	750	7.5	2.00	yes	8.2603
234	a1	0.02	4.50	5.00	900.00	10.00	5.00	Yes	8.3045
236	a3	0.02	4.50	5.00	900.00	10.00	5.00	yes	8.3041
357	b2	0.02	4.00	5.00	700.00	10.00	5.00	yes	8.2443
358	a2	0.02	4.00	5.00	700.00	10.00	5.00	yes	8.2461
237	a4	0.02	4.50	5.00	900.00	10.00	5.00	yes	8.3005
239	b2	0.02	4.50	5.00	900.00	10.00	5.00	yes	8.3065
240	b3	0.02	4.50	5.00	900.00	10.00	5.00	yes	8.3023
241	b4	0.02	4.50	5.00	900.00	10.00	5.00	yes	8.2975
287	b2	0	3.5	2.50	750	7.5	2.00	yes	8.2683
288	b3	0.02	5.5	2.50	750	7.5	2.00	yes	8.2518
289	b4	0.06	3.5	2.50	750	7.5	2.00	yes	8.2602
290	c1	0.08	3.5	2.50	750	7.5	2.00	yes	8.2579

291	c2	0	5.5	2.50	750	7.5	2.00	yes	8.2705
292	c3	0.06	5.5	2.50	750	7.5	2.00	yes	8.2561
293	c4	0.02	4	2.50	750	7.5	2.00	yes	8.2677
242	c1	0.02	4.50	5.00	900.00	10.00	5.00	yes	8.3055
243	c2	0.02	4.50	5.00	900.00	10.00	5.00	no	8.2986
364	a4	0.02	4.00	5.00	700.00	10.00	5.00	yes	8.2524
244	c3	0.02	4.50	5.00	900.00	10.00	5.00	yes	8.2996
245	c4	0.02	4.50	5.00	900.00	10.00	5.00	no	8.3014
350	b2	0.02	4.00	5.00	900.00	10.00	5.00	yes	8.2908
363	a3	0.02	4.00	5.00	700.00	10.00	5.00	yes	8.2459

Figure 58: Synthetic parameters for the LFMO samples described in Chapter 4. Non reproducible samples are marked in orange while the reproducible samples used to find trends between synthetic parameters and LFMO structure are marked in green. NR stands for not registered.

ANNEX IV: List of contributions

A.1. Publications

- **Iciar Monterrubio**, Oier Lakuntza, Montse Casas-Cabanas, Marine Reynaud, Javier Carrasco, Amaia Saracibar. **Elucidating the electrochemical properties of $LiFe_{0.5}Mn_{1.5}O_4$ using first-principles calculations.** Submitted to *Electrochimica acta* (July 2023).
- **Iciar Monterrubio**, Maha Ismail, Joseba Orive, Evaristo Castillo, Amaia Saracibar, Javier Carrasco, Javier García, Ismael Redondo, Jean-Luc Dauvergne, Montse Casas-Cabanas, Marine Reynaud. **Building a Materials Acceleration Platform (MAP) for battery materials research: Automated modules for solid-state and solvothermal syntheses of inorganic compounds**. Under preparation.
- **Iciar Monterrubio**, Marcus Fehse, Aitor Herrán, Jose Javier Saiz Garitaonandia, Rosalia Cid, Amaia Saracibar, Marine Reynaud, Montse Casas-Cabanas. **Highlights on the structural defects and electrochemical mechanism of high-voltage $LiFe_{0.5}Mn_{1.5}O_4$ spinel.** Under preparation.
-

A.2. Conferences

- I. Monterrubio, J. Orive, M. Ismail, E. Castillo, A. Saracibar, J. Carrasco, J. García, I. Redondo, J.L. Dauvergne, M. Casas-Cabanas, M. Reynaud. A high-throughput experimental approach for battery materials exploration. International Conference on Materials for Advanced Technologies (**ICMAT23**). June 2023, Singapur (**oral**).
- I. Monterrubio, E. Castillo, A. Saracibar, J. Carrasco, M. Casas-Cabanas, M. Reynaud. High-throughput experimental automated module for the exploration of inorganic battery materials. **IBA22**. October 2022, Bled, Slovenia (**poster**).
- I. Monterrubio, E. Castillo, A. Saracibar, J. Carrasco, M. Reynaud, M. Casas-Cabanas. Accelerated design of new electrode materials for Li-ion batteries. XIII Reunión del Grupo

Especializado de Química de Estado Sólido (**QIES22**). January 2022, Sevilla, Spain (**oral**).

- I. Monterrubio, M. Reynaud, A. Wizner, N. A. Katcho, J. Rodríguez-Carvajal, A. Saracibar, J. Carrasco, M. Casas-Cabanas. Accelerated design of new electrode materials for Li-ion and Na-ion batteries. 6th European Crystallographic School (**ECS**). July 2021. Budapest, Hungary (**poster**).
- M. Reynaud, A. Wizner, I. Monterrubio*, N. A. Katcho, J. Rodríguez-Carvajal, A. Saracibar, J. Carrasco, M. Casas-Cabanas. Accelerated design of new electrode materials for Li-ion and Na-ion batteries. International Battery Seminar (**IBS**). July 2020. Orlando, USA (**poster**)
- M. Reynaud, A. Wizner, I. Monterrubio*, N. A. Katcho, J. Rodríguez-Carvajal, A. Saracibar, J. Carrasco, M. Casas-Cabanas. Accelerated design of new electrode materials for Li-ion and Na-ion batteries. **Materials project workshop 2020 on computational materials design and discovery**. July 2020. Berkeley, USA (**poster**)
- I. Monterrubio. From the synthesis of new materials to a more sustainable world. **Jornadas doctoriales transfronterizas**. October 2019**.** Pau, France (**poster**)

A.3. Stays in R&D centers.

- **Fraunhofer-Institut für Zuverlässigkeit und Mikrointegration (IZM**). Micro energy group lead by Robert Hahn. Berlin, Germany. From 1/8/2022 to 1/11/2022.
-

A.4. Patents

- **Iciar Monterrubio**, Marine Reynaud, Montse Casas-Cabanas. **Spinel materials with controlled atomic structure as electroactive materials.** Deposit 4th August 2023. Application Number: EP23382820.1.

REFERENCES

(1) Bhatt, M. D.; O'Dwyer, C. Recent Progress in Theoretical and Computational Investigations of Li-Ion Battery Materials and Electrolytes. *Phys. Chem. Chem. Phys.* **2015**, *17* (7), 4799–4844. https://doi.org/10.1039/C4CP05552G.

(2) *Climate Change: Atmospheric Carbon Dioxide | NOAA Climate.gov*. http://www.climate.gov/news-features/understanding-climate/climate-change-atmospheric-carbon-dioxide (accessed 2023-07-07).

(3) Coppola, P.; Arsenio, E. Driving Societal Changes towards an Electromobility Future. *Eur. Transp. Res. Rev.* **2015**, *7* (4), 1–2. https://doi.org/10.1007/s12544-015-0186-0.

(4) *Regulation (EU) 2023/851 of the European Parliament and of the Council of 19 April 2023 Amending Regulation (EU) 2019/631 as Regards Strengthening the CO2 Emission Performance Standards for New Passenger Cars and New Light Commercial Vehicles in Line with the Union's Increased Climate Ambition (Text with EEA Relevance)*; 2023; Vol. 110. http://data.europa.eu/eli/reg/2023/851/oj/eng (accessed 2023-08-18).

(5) Capasso, C.; Veneri, O. Experimental Analysis on the Performance of Lithium Based Batteries for Road Full Electric and Hybrid Vehicles. *Appl. Energy* **2014**, *136*, 921–930. https://doi.org/10.1016/j.apenergy.2014.04.013.

(6) *EQS Berlina | Mercedes-Benz*. https://www.mercedes-benz.es/passengercars/models/saloon/eqs/overview.html (accessed 2023-08-18).

(7) Wang, S.; Fan, Y.; Stroe, D.-I.; Fernandez, C.; Yu, C.; Cao, W.; Chen, Z. Chapter 1 - Lithium-Ion Battery Characteristics and Applications. In *Battery System Modeling*; Wang, S., Fan, Y., Stroe, D.-I., Fernandez, C., Yu, C., Cao, W., Chen, Z., Eds.; Elsevier, 2021; pp 1–46. https://doi.org/10.1016/B978-0-323-90472-8.00003-2.

(8) Liang, Y.; Zhao, C.-Z.; Yuan, H.; Chen, Y.; Zhang, W.; Huang, J.-Q.; Yu, D.; Liu, Y.; Titirici, M.-M.; Chueh, Y.-L.; Yu, H.; Zhang, Q. A Review of Rechargeable Batteries for Portable Electronic Devices. *InfoMat* **2019**, *1* (1), 6–32. https://doi.org/10.1002/inf2.12000.

(9) Armand, M.; Tarascon, J.-M. Building Better Batteries. *Nature* **2008**, *451* (7179), 652–657. https://doi.org/10.1038/451652a.

(10) Cunha, Á.; Martins, J.; Rodrigues, N.; Brito, F. P. Vanadium Redox Flow Batteries: A Technology Review. *Int. J. Energy Res.* **2015**, *39* (7), 889–918. https://doi.org/10.1002/er.3260.

(11) Dhar, S. K.; Ovshínsky, S. R.; Gifford, P. R.; Corrigan, D. A.; Fetcenko, M. A.; Venkatesan, S. Nickel/Metal Hydride Technology for Consumer and Electric Vehicle Batteries—a Review and up-Date. *J. Power Sources* **1997**, *65* (1), 1–7. https://doi.org/10.1016/S0378-7753(96)02599-2.

(12) Koehler, U. Chapter 2 - General Overview of Non-Lithium Battery Systems and Their Safety Issues. In *Electrochemical Power Sources: Fundamentals, Systems,*

and Applications; Garche, J., Brandt, K., Eds.; Elsevier, 2019; pp 21–46. https://doi.org/10.1016/B978-0-444-63777-2.00002-5.
(13) Garche, J.; Dyer, C. K. *Encyclopedia of Electrochemical Power Sources*; Elsevier, 2009.
(14) Tarascon, J.-M.; Armand, M. Issues and Challenges Facing Rechargeable Lithium Batteries. *Nature* **2001**, *414* (6861), 359–367. https://doi.org/10.1038/35104644.
(15) Vincent, C. Lithium Batteries: A 50-Year Perspective, 1959-2009. *Solid State Ion.* **2000**, *134*, 159–167. https://doi.org/10.1016/S0167-2738(00)00723-2.
(16) Dunn, B.; Kamath, H.; Tarascon, J.-M. Electrical Energy Storage for the Grid: A Battery of Choices. *Science* **2011**, *334* (6058), 928–935. https://doi.org/10.1126/science.1212741.
(17) Goodenough, J. B.; Park, K.-S. The Li-Ion Rechargeable Battery: A Perspective. *J. Am. Chem. Soc.* **2013**, *135* (4), 1167–1176. https://doi.org/10.1021/ja3091438.
(18) de las Casas, C.; Li, W. A Review of Application of Carbon Nanotubes for Lithium Ion Battery Anode Material. *J. Power Sources* **2012**, *208*, 74–85. https://doi.org/10.1016/j.jpowsour.2012.02.013.
(19) Zhang, L.; Zhu, C.; Yu, S.; Ge, D.; Zhou, H. Status and Challenges Facing Representative Anode Materials for Rechargeable Lithium Batteries. *J. Energy Chem.* **2022**, *66*, 260–294. https://doi.org/10.1016/j.jechem.2021.08.001.
(20) Liu, Y.-K.; Zhao, C.-Z.; Du, J.; Zhang, X.-Q.; Chen, A.-B.; Zhang, Q. Research Progresses of Liquid Electrolytes in Lithium-Ion Batteries. *Small* **2023**, *19* (8), 2205315. https://doi.org/10.1002/smll.202205315.
(21) Han, L.; Lehmann, M. L.; Zhu, J.; Liu, T.; Zhou, Z.; Tang, X.; Heish, C.-T.; Sokolov, A. P.; Cao, P.; Chen, X. C.; Saito, T. Recent Developments and Challenges in Hybrid Solid Electrolytes for Lithium-Ion Batteries. *Front. Energy Res.* **2020**, *8*.
(22) Li, S.; Zhang, S.-Q.; Shen, L.; Liu, Q.; Ma, J.-B.; Lv, W.; He, Y.-B.; Yang, Q.-H. Progress and Perspective of Ceramic/Polymer Composite Solid Electrolytes for Lithium Batteries. *Adv. Sci.* **2020**, *7* (5), 1903088. https://doi.org/10.1002/advs.201903088.
(23) Marcinek, M.; Syzdek, J.; Marczewski, M.; Piszcz, M.; Niedzicki, L.; Kalita, M.; Plewa-Marczewska, A.; Bitner, A.; Wieczorek, P.; Trzeciak, T.; Kasprzyk, M.; P.Łężak; Zukowska, Z.; Zalewska, A.; Wieczorek, W. Electrolytes for Li-Ion Transport – Review. *Solid State Ion.* **2015**, *276*, 107–126. https://doi.org/10.1016/j.ssi.2015.02.006.
(24) Feng, J. K.; Lu, L.; Lai, M. O. Lithium Storage Capability of Lithium Ion Conductor Li1.5Al0.5Ge1.5(PO4)3. *J. Alloys Compd.* **2010**, *501* (2), 255–258. https://doi.org/10.1016/j.jallcom.2010.04.084.
(25) Li, M.; Wang, C.; Chen, Z.; Xu, K.; Lu, J. New Concepts in Electrolytes. *Chem. Rev.* **2020**, *120* (14), 6783–6819. https://doi.org/10.1021/acs.chemrev.9b00531.

(26) Matsumoto, F.; Gunji, T. All-Solid-State LIBs. In *Water in Lithium-Ion Batteries*; Matsumoto, F., Gunji, T., Eds.; SpringerBriefs in Energy; Springer Nature: Singapore, 2022; pp 57–66. https://doi.org/10.1007/978-981-16-8786-0_7.
(27) Palacin, M. R. Battery Materials Design Essentials. *Acc. Mater. Res.* **2021**, *2* (5), 319–326. https://doi.org/10.1021/accountsmr.1c00026.
(28) Shiraishi, K.; Dokko, K.; Kanamura, K. Formation of Impurities on Phospho-Olivine LiFePO4 during Hydrothermal Synthesis. *J. Power Sources* **2005**, *146* (1), 555–558. https://doi.org/10.1016/j.jpowsour.2005.03.060.
(29) Antaya, M.; Dahn, J. R.; Preston, J. S.; Rossen, E.; Reimers, J. N. Preparation and Characterization of LiCoO2 Thin Films by Laser Ablation Deposition. *J. Electrochem. Soc.* **1993**, *140* (3), 575. https://doi.org/10.1149/1.2056123.
(30) Zhang, C.; Liu, X.; Su, Q.; Wu, J.; Huang, T.; Yu, A. Enhancing Electrochemical Performance of LiMn2O4 Cathode Material at Elevated Temperature by Uniform Nanosized TiO2 Coating. *ACS Sustain. Chem. Eng.* **2017**, *5* (1), 640–647. https://doi.org/10.1021/acssuschemeng.6b02011.
(31) Padhi, A. K.; Nanjundaswamy, K. S.; Goodenough, J. B. Phospho-olivines as Positive-Electrode Materials for Rechargeable Lithium Batteries. *J. Electrochem. Soc.* **1997**, *144* (4), 1188. https://doi.org/10.1149/1.1837571.
(32) Malik, R.; Abdellahi, A.; Ceder, G. A Critical Review of the Li Insertion Mechanisms in LiFePO4 Electrodes. *J. Electrochem. Soc.* **2013**, *160* (5), A3179. https://doi.org/10.1149/2.029305jes.
(33) Zhang, W.-J. Structure and Performance of LiFePO4 Cathode Materials: A Review. *J. Power Sources* **2011**, *196* (6), 2962–2970. https://doi.org/10.1016/j.jpowsour.2010.11.113.
(34) Chen, S.-P.; Lv, D.; Chen, J.; Zhang, Y.-H.; Shi, F.-N. Review on Defects and Modification Methods of LiFePO4 Cathode Material for Lithium-Ion Batteries. *Energy Fuels* **2022**, *36* (3), 1232–1251. https://doi.org/10.1021/acs.energyfuels.1c03757.
(35) Kim, D.-H.; Kim, J. Synthesis of LiFePO4 Nanoparticles and Their Electrochemical Properties. *J. Phys. Chem. Solids* **2007**, *68* (5), 734–737. https://doi.org/10.1016/j.jpcs.2007.03.019.
(36) Yu, W.; Ou, G.; Qi, L.; Wu, H. Textured LiFePO $_4$ Bulk with Enhanced Electrical Conductivity. *J. Am. Ceram. Soc.* **2016**, *99* (10), 3214–3216. https://doi.org/10.1111/jace.14426.
(37) Barker, J.; Saidi, M.; Swoyer, J. Electrochemical Insertion Properties of the Novel Lithium Vanadium Fluorophosphate, LiVPO4F. *Cheminform* **2004**, *35*. https://doi.org/10.1002/chin.200403013.
(38) Sharma, L.; Adiga, S. P.; Alshareef, H. N.; Barpanda, P. Fluorophosphates: Next Generation Cathode Materials for Rechargeable Batteries. *Adv. Energy Mater.* **2020**, *10* (43), 2001449. https://doi.org/10.1002/aenm.202001449.
(39) *LixCoO2 (0<x<-1): A new cathode material for batteries of high energy density | Semantic Scholar*. https://www.semanticscholar.org/paper/LixCoO2-

(0%3Cx%3C-1)%3A-A-new-cathode-material-for-of-Mizushima-Jones/0e9dcbc1f1454d1bf64a1106e8a31a7bc6a2ba51 (accessed 2023-06-23).
(40) Zhang, W.; Richter, F. H.; Culver, S. P.; Leichtweiss, T.; Lozano, J. G.; Dietrich, C.; Bruce, P. G.; Zeier, W. G.; Janek, J. Degradation Mechanisms at the Li10GeP2S12/LiCoO2 Cathode Interface in an All-Solid-State Lithium-Ion Battery. *ACS Appl. Mater. Interfaces* **2018**, *10* (26), 22226–22236. https://doi.org/10.1021/acsami.8b05132.
(41) Rozier, P.; Tarascon, J. M. Review—Li-Rich Layered Oxide Cathodes for Next-Generation Li-Ion Batteries: Chances and Challenges. *J. Electrochem. Soc.* **2015**, *162* (14), A2490. https://doi.org/10.1149/2.0111514jes.
(42) Andre, D.; Kim, S.-J.; Lamp, P.; Lux, S. F.; Maglia, F.; Paschos, O.; Stiaszny, B. Future Generations of Cathode Materials: An Automotive Industry Perspective. *J. Mater. Chem. A* **2015**, *3* (13), 6709–6732. https://doi.org/10.1039/C5TA00361J.
(43) Hou, P.; Yin, J.; Ding, M.; Huang, J.; Xu, X. Surface/Interfacial Structure and Chemistry of High-Energy Nickel-Rich Layered Oxide Cathodes: Advances and Perspectives. *Small* **2017**, *13* (45), 1701802. https://doi.org/10.1002/smll.201701802.
(44) Vadivel, S.; Phattharasupakun, N.; Wutthiprom, J.; Duangdangchote, S.; Sawangphruk, M. High-Performance Li-Ion Batteries Using Nickel-Rich Lithium Nickel Cobalt Aluminium Oxide-Nanocarbon Core-Shell Cathode: In Operando X-Ray Diffraction. *ACS Appl. Mater. Interfaces* **2019**, *11* (34), 30719–30727. https://doi.org/10.1021/acsami.9b06553.
(45) Zhu, L.; Bao, C.; Xie, L.; Yang, X.; Cao, X. Review of Synthesis and Structural Optimization of LiNi1/3Co1/3Mn1/3O2 Cathode Materials for Lithium-Ion Batteries Applications. *J. Alloys Compd.* **2020**, *831*, 154864. https://doi.org/10.1016/j.jallcom.2020.154864.
(46) Li, J.; Li, H.; Stone, W.; Weber, R.; Hy, S.; Dahn, J. R. Synthesis of Single Crystal LiNi0.5Mn0.3Co0.2O2 for Lithium Ion Batteries. *J. Electrochem. Soc.* **2017**, *164* (14), A3529. https://doi.org/10.1149/2.0401714jes.
(47) Tian, C.; Nordlund, D.; Xin, H. L.; Xu, Y.; Liu, Y.; Sokaras, D.; Lin, F.; Doeff, M. M. Depth-Dependent Redox Behavior of LiNi0.6Mn0.2Co0.2O2. *J. Electrochem. Soc.* **2018**, *165* (3), A696. https://doi.org/10.1149/2.1021803jes.
(48) Ruan, Y.; Song, X.; Fu, Y.; Song, C.; Battaglia, V. Structural Evolution and Capacity Degradation Mechanism of LiNi0.6Mn0.2Co0.2O2 Cathode Materials. *J. Power Sources* **2018**, *400*, 539–548. https://doi.org/10.1016/j.jpowsour.2018.08.056.
(49) Li, J.; Downie, L. E.; Ma, L.; Qiu, W.; Dahn, J. R. Study of the Failure Mechanisms of LiNi0.8Mn0.1Co0.1O2 Cathode Material for Lithium Ion Batteries. *J. Electrochem. Soc.* **2015**, *162* (7), A1401. https://doi.org/10.1149/2.1011507jes.
(50) Aribia, A.; Sastre, J.; Chen, X.; Futscher, M. H.; Rumpel, M.; Priebe, A.; Döbeli, M.; Osenciat, N.; Tiwari, A. N.; Romanyuk, Y. E. Unlocking Stable Multi-Electron

Cycling in NMC811 Thin-Films between 1.5 – 4.7 V. *Adv. Energy Mater.* **2022**, *12* (40), 2201750. https://doi.org/10.1002/aenm.202201750.
(51) Johnston, B. I. J. High Energy Density Positive Insertion Electrodes for next Generation Lithium-Ion Batteries.
(52) Luo, Y.; Wei, H.; Tang, L.; Huang, Y.; Wang, Z.; He, Z.; Yan, C.; Mao, J.; Dai, K.; Zheng, J. Nickel-Rich and Cobalt-Free Layered Oxide Cathode Materials for Lithium Ion Batteries. *Energy Storage Mater.* **2022**, *50*, 274–307. https://doi.org/10.1016/j.ensm.2022.05.019.
(53) Shao, Q.; Gao, P.; Yan, C.; Gao, M.; Du, W.; Chen, J.; Yang, Y.; Gan, J.; Wu, Z.; Zhang, C.; Chen, G.; Zheng, X.; Lin, Y.; Jiang, Y.; Sun, W.; Liu, Y.; Gao, M.; Pan, H. A Redox Couple Strategy Enables Long-Cycling Li- and Mn-Rich Layered Oxide Cathodes by Suppressing Oxygen Release. *Adv. Mater.* **2022**, *34* (14), 2108543. https://doi.org/10.1002/adma.202108543.
(54) Assat, G.; Tarascon, J.-M. Fundamental Understanding and Practical Challenges of Anionic Redox Activity in Li-Ion Batteries. *Nat. Energy* **2018**, *3* (5), 373–386. https://doi.org/10.1038/s41560-018-0097-0.
(55) Šutka, A.; Gross, K. A. Spinel Ferrite Oxide Semiconductor Gas Sensors. *Sens. Actuators B Chem.* **2016**, *222*, 95–105. https://doi.org/10.1016/j.snb.2015.08.027.
(56) Harrison, M. R.; Edwards, P. P.; Goodenough, J. B. The Superconductor-Semiconductor Transition in the Li1+xTi2-xO4 Spinel System. *Philos. Mag. B* **1985**, *52* (3), 679–699. https://doi.org/10.1080/13642818508240629.
(57) Dey, S.; Dhal, G. C. Catalytic Conversion of Carbon Monoxide into Carbon Dioxide over Spinel Catalysts: An Overview. *Mater. Sci. Energy Technol.* **2019**, *2* (3), 575–588. https://doi.org/10.1016/j.mset.2019.06.003.
(58) Sato, Y.; Kiyohara, J.; Hasegawa, A.; Hattori, T.; Ishida, M.; Hamada, N.; Oka, N.; Shigesato, Y. Study on Inverse Spinel Zinc Stannate, Zn2SnO4, as Transparent Conductive Films Deposited by Rf Magnetron Sputtering. *Thin Solid Films* **2009**, *518* (4), 1304–1308. https://doi.org/10.1016/j.tsf.2009.06.057.
(59) Windisch, C. F.; Exarhos, G. J.; Ferris, K. F.; Engelhard, M. H.; Stewart, D. C. Infrared Transparent Spinel Films with P-Type Conductivity. *Thin Solid Films* **2001**, *398–399*, 45–52. https://doi.org/10.1016/S0040-6090(01)01302-5.
(60) Thackeray, M. M.; Johnson, P. J.; de Picciotto, L. A.; Bruce, P. G.; Goodenough, J. B. Electrochemical Extraction of Lithium from LiMn2O4. *Mater. Res. Bull.* **1984**, *19* (2), 179–187. https://doi.org/10.1016/0025-5408(84)90088-6.
(61) Thackeray, M. M.; David, W. I. F.; Bruce, P. G.; Goodenough, J. B. Lithium Insertion into Manganese Spinels. *Mater. Res. Bull.* **1983**, *18* (4), 461–472. https://doi.org/10.1016/0025-5408(83)90138-1.
(62) Sevillano, J. S. Experimental and Theoretical Study of Structural Defects and Impact on Electrochemical Performance on Li-Rich Oxides.
(63) Häse, F.; Roch, L. M.; Aspuru-Guzik, A. Next-Generation Experimentation with Self-Driving Laboratories. *Trends Chem.* **2019**, *1* (3), 282–291. https://doi.org/10.1016/j.trechm.2019.02.007.

(64) Choi, S.; Wang, G. Advanced Lithium-Ion Batteries for Practical Applications: Technology, Development, and Future Perspectives. *Adv. Mater. Technol.* **2018**, *3* (9), 1700376. https://doi.org/10.1002/admt.201700376.
(65) Casas-Cabanas, M.; Ponrouch, A.; Palacín, M. R. Blended Positive Electrodes for Li-Ion Batteries: From Empiricism to Rational Design. *Isr. J. Chem.* **2021**, *61* (1–2), 26–37. https://doi.org/10.1002/ijch.202000099.
(66) Tsunoda, M.; Oshima, Y.; Yoshinaga, M.; Shirasu, T. Prismatic Lithium-Ion Rechargeable Battery with Manganese Spinel and Nickel-Cobalt Oxide Cathode. *NEC Res. Dev.* **2000**, *41*, 13–17.
(67) Sun, Y.-K.; Oh, I.-H.; Kim, K. Y. Synthesis of Spinel LiMn2O4 by the Sol−Gel Method for a Cathode-Active Material in Lithium Secondary Batteries. *Ind. Eng. Chem. Res.* **1997**, *36* (11), 4839–4846. https://doi.org/10.1021/ie970227b.
(68) Hwang, B. J.; Santhanam, R.; Liu, D. G. Effect of Various Synthetic Parameters on Purity of LiMn2O4 Spinel Synthesized by a Sol–Gel Method at Low Temperature. *J. Power Sources* **2001**, *101* (1), 86–89. https://doi.org/10.1016/S0378-7753(01)00657-7.
(69) Liang, X. Structural and Electronic Properties of Cation Doping on the Spinel LiMn2O4: A First-Principles Theory. *Int. J. Electrochem. Sci.* **2016**, *11*, 9394–9401. https://doi.org/10.20964/2016.11.59.
(70) Huang, Y.; Dong, Y.; Li, S.; Lee, J.; Wang, C.; Zhu, Z.; Xue, W.; Li, Y.; Li, J. Lithium Manganese Spinel Cathodes for Lithium-Ion Batteries. *Adv. Energy Mater.* **2021**, *11* (2), 2000997. https://doi.org/10.1002/aenm.202000997.
(71) Banerjee, A.; Ziv, B.; Shilina, Y.; Ziegelbauer, J. M.; Liu, H.; Harris, K. J.; Botton, G.; Goward, G. R.; Luski, S.; Aurbach, D.; Halalay, I. C. Review—Multifunctional Separators: A Promising Approach for Improving the Durability and Performance of Li-Ion Batteries. *J. Electrochem. Soc.* **2019**, *166* (3), A5369. https://doi.org/10.1149/2.0561903jes.
(72) Zhan, C.; Wu, T.; Lu, J.; Amine, K. Dissolution, Migration, and Deposition of Transition Metal Ions in Li-Ion Batteries Exemplified by Mn-Based Cathodes – a Critical Review. *Energy Environ. Sci.* **2018**, *11* (2), 243–257. https://doi.org/10.1039/C7EE03122J.
(73) Bhaskar, A.; Bramnik, N. N.; Senyshyn, A.; Fuess, H.; Ehrenberg, H. Synthesis, Characterization, and Comparison of Electrochemical Properties of LiM0.5Mn1.5O4 (M = Fe , Co, Ni) at Different Temperatures. *J. Electrochem. Soc.* **2010**, *157* (6), A689. https://doi.org/10.1149/1.3365025.
(74) Bhaskar, A. Investigations on LiM0.5Mn1.5O4 (M = Fe, Co, Ni) Spinels as High-Volt Cathode Materials for Rechargeable Lithium-Ion Batteries; 2011.
(75) Shigemura, H.; Tabuchi, M.; Kobayashi, H.; Sakaebe, H.; Hirano, A.; Kageyama, H. Structural and Electrochemical Properties of Li(Fe, Co)xMn2 −xO4 Solid Solution as 5 V Positive Electrode Materials for Li Secondary Batteries. *J. Mater. Chem.* **2002**, *12* (6), 1882–1891. https://doi.org/10.1039/B200690C.
(76) Fehse, M.; Etxebarria, N.; Otaegui, L.; Cabello, M.; Martín-Fuentes, S.; Cabañero, M. A.; Monterrubio, I.; Elkjær, C. F.; Fabelo, O.; Enkubari, N. A.;

López Del Amo, J. M.; Casas-Cabanas, M.; Reynaud, M. Influence of Transition-Metal Order on the Reaction Mechanism of LNMO Cathode Spinel: An Operando X-Ray Absorption Spectroscopy Study. *Chem. Mater. Publ. Am. Chem. Soc.* **2022**, *34* (14), 6529–6540. https://doi.org/10.1021/acs.chemmater.2c01360.

(77) *American Chemistry Council*. American Chemistry Council. https://www.americanchemistry.com/ (accessed 2023-06-08).

(78) Eftekhari, A. Electrochemical Performance and Cyclability of LiFe0.5Mn1.5O4 as a 5 V Cathode Material for Lithium Batteries. *J. Power Sources* **2003**, *124* (1), 182–190. https://doi.org/10.1016/S0378-7753(03)00602-5.

(79) Wang, F.; Suo, L.; Liang, Y.; Yang, C.; Han, F.; Gao, T.; Sun, W.; Wang, C. Spinel LiNi0.5Mn1.5O4 Cathode for High-Energy Aqueous Lithium-Ion Batteries. *Adv. Energy Mater.* **2017**, *7* (8), 1600922. https://doi.org/10.1002/aenm.201600922.

(80) Strobel, P.; Ibarra-Palos, A.; Poinsignon, C. Cation Ordering in Substituted LiMn2O4 Spinels. *MRS Online Proc. Libr. OPL* **2002**, *756*, EE5.4. https://doi.org/10.1557/PROC-756-EE5.4.

(81) Casas-Cabanas, M.; Kim, C.; Rodríguez-Carvajal, J.; Cabana, J. Atomic Defects during Ordering Transitions in LiNi0.5Mn1.5O4 and Their Relationship with Electrochemical Properties. *J. Mater. Chem. A* **2016**, *4* (21), 8255–8262. https://doi.org/10.1039/C6TA00424E.

(82) Yu, F.; Wang, Y.; Guo, C.; Liu, H.; Bao, W.; Li, J.; Zhang, P.; Wang, F. Spinel LiMn2O4 Cathode Materials in Wide Voltage Window: Single-Crystalline versus Polycrystalline. *Crystals* **2022**, *12* (3), 317. https://doi.org/10.3390/cryst12030317.

(83) Stüble, P.; Mereacre, V.; Geßwein, H.; Binder, J. R. On the Composition of LiNi0.5Mn1.5O4 Cathode Active Materials. *Adv. Energy Mater.* **2023**, *13* (10), 2203778. https://doi.org/10.1002/aenm.202203778.

(84) Eglitis, R. I. Theoretical Prediction of the 5 V Rechargeable Li Ion Battery Using $Li_2CoMn_3O_8$ as a Cathode. *Phys. Scr.* **2015**, *90* (9), 094012. https://doi.org/10.1088/0031-8949/90/9/094012.

(85) Idemoto, Y.; Narai, H.; Koura, N. Oxygen Content and Electrode Characterisitcs of LiMn1.5Ni0.5O4 as a 5 V Class Cathode Material for Lithium Secondary Battery. *Electrochemistry* **2002**, *70* (8), 587–589.

(86) Ohzuku, T.; Ariyoshi, K.; Takeda, S.; Sakai, Y. Synthesis and Characterization of 5 V Insertion Material of Li[FeyMn2−y]O4 for Lithium-Ion Batteries. *Electrochimica Acta* **2001**, *46* (15), 2327–2336. https://doi.org/10.1016/S0013-4686(00)00725-8.

(87) Cabana, J.; Casas-Cabanas, M.; Omenya, F. O.; Chernova, N. A.; Zeng, D.; Whittingham, M. S.; Grey, C. P. Composition-Structure Relationships in the Li-Ion Battery Electrode Material LiNi0.5Mn1.5O4. *Chem. Mater.* **2012**, *24* (15), 2952–2964. https://doi.org/10.1021/cm301148d.

(88) Lee, E.; Persson, K. A. Revealing the Coupled Cation Interactions behind the Electrochemical Profile of LixNi0.5Mn1.5O4. *Energy Environ. Sci.* **2012**, *5* (3), 6047–6051. https://doi.org/10.1039/C2EE03068C.
(89) Amine, K.; Tukamoto, H.; Yasuda, H.; Fujita, Y. Preparation and Electrochemical Investigation of LiMn2 − xMexO4 (Me: Ni, Fe, and x = 0.5, 1) Cathode Materials for Secondary Lithium Batteries. *J. Power Sources* **1997**, *68* (2), 604–608. https://doi.org/10.1016/S0378-7753(96)02590-6.
(90) Mateyshina, Y.; Lafont, U.; Uvarov, N.; Kelder, E. Physical and Electrochemical Properties of LiFe 0.5 Mn 1.5 O 4 Spinel Synthesized by Different Methods. *Russ. J. Electrochem. - Russ. J Electrochem.* **2009**, *45*, 602–605. https://doi.org/10.1134/S102319350905019X.
(91) Li, Y.; Ma, B.; Chen, N.; Lu, J.; Wang, A.; Liu, L.; Liu, Y.; Wang, W.; Li, X.; Cardona, Y.; Uwakweh, O. N. C.; Rong, C.; Gao, J.; Lu, J.; Xu, Z.; Ma, X.; Cao, G. Structural and Magnetic Properties of LiMn1.5Fe0.5O4 Spinel Oxide. *Phys. B Condens. Matter* **2010**, *405* (23), 4733–4739. https://doi.org/10.1016/j.physb.2010.08.050.
(92) Fadzil, A. F. M.; Puad, N. S. A.; Subban, R. H. Y.; Kamarulzaman, N. Comparative Study of Substituted LiMn(2-x)FexO4 via Sol-Gel Route.
(93) Li, Y.; Ma, B.; Wang, A.; Chen, N.; Liu, L.; Liu, Y.; Wang, W.; Li, X.; Cao, G.; Ma, X.; Lu, J. Comparison Study of Magnetic Ordering for Fe-Free and Fe-Doped $LiMn_2O_4$ Spinel Oxide. *J. Phys. Conf. Ser.* **2011**, *273*, 012117. https://doi.org/10.1088/1742-6596/273/1/012117.
(94) Pico, M. P.; Álvarez-Serrano, I.; López, M. L.; Veiga, M. L. Role of Morphology in the Performance of LiFe0.5Mn1.5O4 Spinel Cathodes for Lithium-Ion Batteries. *Dalton Trans.* **2014**, *43* (39), 14787–14797. https://doi.org/10.1039/C4DT01809E.
(95) Shigemura, H.; Sakaebe, H.; Kageyama, H.; Kobayashi, H.; West, A.; Kanno, R.; Morimoto, S.; Nasu, S.; Tabuchi, M. Structure and Electrochemical Properties of LiFexMn2-xO4 (0 ≤ x ≤ 0.5) Spinel as 5 V Electrode Material for Lithium Batteries. *J. Electrochem. Soc. - J ELECTROCHEM SOC* **2001**, *148*. https://doi.org/10.1149/1.1377593.
(96) Mu, Y.; Zeng, M.; Wu, X.; Tong, X. Electrochemical Performance of LiFexNi0.5-xMn1.5O4 Cathode Material for Lithium-Ion Batteries. *Int. J. Electrochem. Sci.* **2017**, *12* (7), 6045–6053. https://doi.org/10.20964/2017.07.18.
(97) Xu, H.; Zhu, Q.; Zhao, Y.; Du, Z.; Li, B.; Yang, S. Phase-Changeable Dynamic Conformal Electrode/Electrolyte Interlayer Enabling Pressure-Independent Solid-State Lithium Metal Batteries. *Adv. Mater.* **2023**, *35* (18), 2212111. https://doi.org/10.1002/adma.202212111.
(98) Aspuru-Guzik, A.; Persson, K. Materials Acceleration Platform: Accelerating Advanced Energy Materials Discovery by Integrating High-Throughput Methods and Artificial Intelligence. *Mission Innov.* **2018**.
(99) Flores-Leonar, M. M.; Mejía-Mendoza, L. M.; Aguilar-Granda, A.; Sanchez-Lengeling, B.; Tribukait, H.; Amador-Bedolla, C.; Aspuru-Guzik, A. Materials

Acceleration Platforms: On the Way to Autonomous Experimentation. *Curr. Opin. Green Sustain. Chem.* **2020**, *25*, 100370. https://doi.org/10.1016/j.cogsc.2020.100370.

(100) Stein, H. S.; Gregoire, J. M. Progress and Prospects for Accelerating Materials Science with Automated and Autonomous Workflows. *Chem. Sci.* **2019**, *10* (42), 9640–9649. https://doi.org/10.1039/C9SC03766G.

(101) Katcho, N. A.; Carrete, J.; Reynaud, M.; Rousse, G.; Casas-Cabanas, M.; Mingo, N.; Rodríguez-Carvajal, J.; Carrasco, J. An Investigation of the Structural Properties of Li and Na Fast Ion Conductors Using High-Throughput Bond-Valence Calculations and Machine Learning. *J. Appl. Crystallogr.* **2019**, *52* (1), 148–157. https://doi.org/10.1107/S1600576718018484.

(102) Filsø, M. Ø.; Turner, M. J.; Gibbs, G. V.; Adams, S.; Spackman, M. A.; Iversen, B. B. Visualizing Lithium-Ion Migration Pathways in Battery Materials. *Chem. – Eur. J.* **2013**, *19* (46), 15535–15544. https://doi.org/10.1002/chem.201301504.

(103) Liu, Y.; Jiang, X.; Zhao, J.; Hu, M. Electronic Charge Density as a Fast Approach for Predicting Li-Ion Migration Pathways in Superionic Conductors with First-Principles Level Precision. *Comput. Mater. Sci.* **2021**, *192*, 110380. https://doi.org/10.1016/j.commatsci.2021.110380.

(104) *Enhancing first-principles simulations of complex solid-state ion conductors using topological analysis of procrystal electron density | npj Computational Materials*. https://www.nature.com/articles/s41524-022-00877-6 (accessed 2023-02-09).

(105) Brown, I. D. Recent Developments in the Methods and Applications of the Bond Valence Model. *Chem. Rev.* **2009**, *109* (12), 6858–6919. https://doi.org/10.1021/cr900053k.

(106) *Bond Valence Pathway Analyzer—An Automatic Rapid Screening Tool for Fast Ion Conductors within softBV | Chemistry of Materials*. https://pubs.acs.org/doi/abs/10.1021/acs.chemmater.0c03893 (accessed 2023-02-09).

(107) Adams, S. From Bond Valence Maps to Energy Landscapes for Mobile Ions in Ion-Conducting Solids. *Solid State Ion.* **2006**, *177*, 1625–1630. https://doi.org/10.1016/j.ssi.2006.03.054.

(108) Reynaud, M.; Rousse, G.; Abakumov, A. M.; Sougrati, M. T.; Tendeloo, G. V.; Chotard, J.-N.; Tarascon, J.-M. Design of New Electrode Materials for Li-Ion and Na-Ion Batteries from the Bloedite Mineral Na2Mg(SO4)2·4H2O. *J. Mater. Chem. A* **2014**, *2* (8), 2671–2680. https://doi.org/10.1039/C3TA13648E.

(109) *Materials Genome Initiative | WWW.MGI.GOV*. https://www.mgi.gov/ (accessed 2023-06-21).

(110) de Pablo, J. J.; Jackson, N. E.; Webb, M. A.; Chen, L.-Q.; Moore, J. E.; Morgan, D.; Jacobs, R.; Pollock, T.; Schlom, D. G.; Toberer, E. S.; Analytis, J.; Dabo, I.; DeLongchamp, D. M.; Fiete, G. A.; Grason, G. M.; Hautier, G.; Mo, Y.; Rajan, K.; Reed, E. J.; Rodriguez, E.; Stevanovic, V.; Suntivich, J.; Thornton, K.;

Zhao, J.-C. New Frontiers for the Materials Genome Initiative. *Npj Comput. Mater.* **2019**, *5* (1), 1–23. https://doi.org/10.1038/s41524-019-0173-4.
(111) Jain, A.; Hautier, G.; Moore, C. J.; Ping Ong, S.; Fischer, C. C.; Mueller, T.; Persson, K. A.; Ceder, G. A High-Throughput Infrastructure for Density Functional Theory Calculations. *Comput. Mater. Sci.* **2011**, *50* (8), 2295–2310. https://doi.org/10.1016/j.commatsci.2011.02.023.
(112) Merrifield, R. B.; Stewart, J. M. Automated Peptide Synthesis. *Nature* **1965**, *207* (996), 522–523. https://doi.org/10.1038/207522a0.
(113) Fitzpatrick, D. E.; Ley, S. V. Engineering Chemistry for the Future of Chemical Synthesis. *Tetrahedron* **2018**, *74* (25), 3087–3100. https://doi.org/10.1016/j.tet.2017.08.050.
(114) Steiner, S.; Wolf, J.; Glatzel, S.; Andreou, A.; Granda, J. M.; Keenan, G.; Hinkley, T.; Aragon-Camarasa, G.; Kitson, P. J.; Angelone, D.; Cronin, L. Organic Synthesis in a Modular Robotic System Driven by a Chemical Programming Language. *Science* **2019**, *363* (6423), eaav2211. https://doi.org/10.1126/science.aav2211.
(115) Wang, H.; Fokwa, B. P. T. *Inorganic Battery Materials*; John Wiley & Sons, 2019.
(116) Schubert, U. S.; Hüsing, N. *Synthesis of Inorganic Materials*; John Wiley & Sons, 2019.
(117) Smith, M. *Organic Synthesis*; Academic Press, 2016.
(118) McCalla, E.; Rowe, A. W.; Shunmugasundaram, R.; Dahn, J. R. Structural Study of the Li–Mn–Ni Oxide Pseudoternary System of Interest for Positive Electrodes of Li-Ion Batteries. *Chem. Mater.* **2013**, *25* (6), 989–999. https://doi.org/10.1021/cm4001619.
(119) Whitacre, J. F.; West, W. C.; Ratnakumar, B. V. A Combinatorial Study of Li y Mn x Ni2 − x O 4 Cathode Materials Using Microfabricated Solid-State Electrochemical Cells. *J. Electrochem. Soc.* **2003**, *150* (12), A1676. https://doi.org/10.1149/1.1622957.
(120) Carey, G. H.; Dahn, J. R. Combinatorial Synthesis of Mixed Transition Metal Oxides for Lithium-Ion Batteries. *ACS Comb. Sci.* **2011**, *13* (2), 186–189. https://doi.org/10.1021/co1000597.
(121) Fujimoto, K.; Kato, T.; Ito, S.; Inoue, S.; Watanabe, M. Development and Application of Combinatorial Electrostatic Atomization System “M-Ist Combi”: High-Throughput Preparation of Electrode Materials. *Solid State Ion.* **2006**, *177* (26), 2639–2642. https://doi.org/10.1016/j.ssi.2006.04.043.
(122) Brown, C. R.; McCalla, E.; Watson, C.; Dahn, J. R. Combinatorial Study of the Li–Ni–Mn–Co Oxide Pseudoquaternary System for Use in Li–Ion Battery Materials Research. *ACS Comb. Sci.* **2015**, *17* (6), 381–391. https://doi.org/10.1021/acscombsci.5b00048.
(123) Adhikari, T.; Hebert, A.; Adamič, M.; Yao, J.; Potts, K.; McCalla, E. Development of High-Throughput Methods for Sodium-Ion Battery Cathodes.

ACS Comb. Sci. **2020**, *22* (6), 311–318. https://doi.org/10.1021/acscombsci.9b00181.

(124) Jonderian, A.; Ting, M.; McCalla, E. Metastability in Li–La–Ti–O Perovskite Materials and Its Impact on Ionic Conductivity. *Chem. Mater.* **2021**, *33* (12), 4792–4804. https://doi.org/10.1021/acs.chemmater.1c01490.

(125) Li, Z.; Najeeb, M. A.; Alves, L.; Sherman, A. Z.; Shekar, V.; Cruz Parrilla, P.; Pendleton, I. M.; Wang, W.; Nega, P. W.; Zeller, M.; Schrier, J.; Norquist, A. J.; Chan, E. M. Robot-Accelerated Perovskite Investigation and Discovery. *Chem. Mater.* **2020**, *32* (13), 5650–5663. https://doi.org/10.1021/acs.chemmater.0c01153.

(126) *Home - BIG-MAP*. https://www.big-map.eu. https://www.big-map.eu/ (accessed 2023-01-24).

(127) *Acceleration Consortium*. https://acceleration.utoronto.ca/ (accessed 2023-01-24).

(128) *DIADEM: an exploratory Priority Research Programme and Infrastructure linking materials and AI | CNRS*. https://www.cnrs.fr/en/diadem-exploratory-priority-research-programme-and-infrastructure-linking-materials-and-ai (accessed 2023-01-24).

(129) Christensen, M.; Yunker, L. P. E.; Shiri, P.; Zepel, T.; Prieto, P. L.; Grunert, S.; Bork, F.; Hein, J. E. Automation Isn't Automatic. *Chem. Sci.* **2021**, *12* (47), 15473–15490. https://doi.org/10.1039/D1SC04588A.

(130) *Discover 2.0 - Microwave Synthesizer*. https://cem.com/en/discover-2 (accessed 2023-02-07).

(131) Nayyar, A.; Puri, V. A Review of Arduino Board's, Lilypad's & Arduino Shields. In *2016 3rd International Conference on Computing for Sustainable Global Development (INDIACom)*; 2016; pp 1485–1492.

(132) *Arduino Official Store | Boards Shields Kits Accessories*. Arduino Official Store. https://store.arduino.cc/ (accessed 2023-01-23).

(133) *FullProf Suite Homepage*. https://www.ill.eu/sites/fullprof/ (accessed 2023-05-19).

(134) Rodríguez-Carvajal, J. Recent Advances in Magnetic Structure Determination by Neutron Powder Diffraction. *Phys. B Condens. Matter* **1993**, *192* (1), 55–69. https://doi.org/10.1016/0921-4526(93)90108-I.

(135) Roisnel, T.; Rodríquez-Carvajal, J. WinPLOTR: A Windows Tool for Powder Diffraction Pattern Analysis. *Mater. Sci. Forum* **2001**, *378–381*, 118–123. https://doi.org/10.4028/www.scientific.net/MSF.378-381.118.

(136) Casas-Cabanas, M.; Kim, C.; Rodríguez-Carvajal, J.; Cabana, J. Atomic Defects during Ordering Transitions in LiNi0.5Mn1.5O4 and Their Relationship with Electrochemical Properties. *J. Mater. Chem. A* **2016**, *4* (21), 8255–8262. https://doi.org/10.1039/C6TA00424E.

(137) Prisms-Center/CASMcode, 2022. https://github.com/prisms-center/CASMcode (accessed 2023-01-20).

(138) Perdew, J. P.; Burke, K.; Ernzerhof, M. Generalized Gradient Approximation Made Simple. *Phys. Rev. Lett.* **1996**, *77* (18), 3865–3868. https://doi.org/10.1103/PhysRevLett.77.3865.

(139) Zhang, Y.; Sun, J.; Perdew, J. P.; Wu, X. Comparative First-Principles Studies of Prototypical Ferroelectric Materials by LDA, GGA, and SCAN Meta-GGA. *Phys. Rev. B* **2017**, *96* (3), 035143. https://doi.org/10.1103/PhysRevB.96.035143.

(140) Hinuma, Y.; Hayashi, H.; Kumagai, Y.; Tanaka, I.; Oba, F. Comparison of Approximations in Density Functional Theory Calculations: Energetics and Structure of Binary Oxides. *Phys. Rev. B* **2017**, *96* (9), 094102. https://doi.org/10.1103/PhysRevB.96.094102.

(141) Zhang, Y.; Kitchaev, D. A.; Yang, J.; Chen, T.; Dacek, S. T.; Sarmiento-Pérez, R. A.; Marques, M. A. L.; Peng, H.; Ceder, G.; Perdew, J. P.; Sun, J. Efficient First-Principles Prediction of Solid Stability: Towards Chemical Accuracy. *Npj Comput. Mater.* **2018**, *4* (1), 9. https://doi.org/10.1038/s41524-018-0065-z.

(142) Kothakonda, M.; Kaplan, A. D.; Isaacs, E. B.; Bartel, C. J.; Furness, J. W.; Ning, J.; Wolverton, C.; Perdew, J. P.; Sun, J. Testing the r2SCAN Density Functional for the Thermodynamic Stability of Solids with and without a van Der Waals Correction. *ACS Mater. Au* **2023**, *3* (2), 102–111. https://doi.org/10.1021/acsmaterialsau.2c00059.

(143) Kitchaev, D. A.; Peng, H.; Liu, Y.; Sun, J.; Perdew, J. P.; Ceder, G. Energetics of MnO 2 Polymorphs in Density Functional Theory. *Phys. Rev. B* **2016**, *93* (4), 045132. https://doi.org/10.1103/PhysRevB.93.045132.

(144) Chakraborty, A.; Dixit, M.; Aurbach, D.; Major, D. T. Predicting Accurate Cathode Properties of Layered Oxide Materials Using the SCAN Meta-GGA Density Functional. *Npj Comput. Mater.* **2018**, *4* (1), 1–9. https://doi.org/10.1038/s41524-018-0117-4.

(145) Kresse, G.; Hafner, J. Ab Initio Molecular Dynamics for Liquid Metals. *Phys. Rev. B* **1993**, *47* (1), 558–561. https://doi.org/10.1103/PhysRevB.47.558.

(146) Kresse, G.; Furthmüller, J. Efficiency of Ab-Initio Total Energy Calculations for Metals and Semiconductors Using a Plane-Wave Basis Set. *Comput. Mater. Sci.* **1996**, *6* (1), 15–50. https://doi.org/10.1016/0927-0256(96)00008-0.

(147) Tang, W.; Sanville, E.; Henkelman, G. A Grid-Based Bader Analysis Algorithm without Lattice Bias. *J. Phys. Condens. Matter* **2009**, *21* (8), 084204. https://doi.org/10.1088/0953-8984/21/8/084204.

(148) Csonka, G. I.; Perdew, J. P.; Ruzsinszky, A.; Philipsen, P. H. T.; Lebègue, S.; Paier, J.; Vydrov, O. A.; Ángyán, J. G. Assessing the Performance of Recent Density Functionals for Bulk Solids. *Phys. Rev. B* **2009**, *79* (15), 155107. https://doi.org/10.1103/PhysRevB.79.155107.

(149) Yang, J. H.; Kitchaev, D. A.; Ceder, G. Rationalizing Accurate Structure Prediction in the Meta-GGA SCAN Functional. *Phys. Rev. B* **2019**, *100* (3), 035132. https://doi.org/10.1103/PhysRevB.100.035132.

(150) Isaacs, E. B.; Wolverton, C. Performance of the Strongly Constrained and Appropriately Normed Density Functional for Solid-State Materials. *Phys. Rev. Mater.* **2018**, *2* (6), 063801. https://doi.org/10.1103/PhysRevMaterials.2.063801.

(151) Abdellahi, A.; Urban, A.; Dacek, S.; Ceder, G. Understanding the Effect of Cation Disorder on the Voltage Profile of Lithium Transition-Metal Oxides. *Chem. Mater.* **2016**, *28* (15), 5373–5383. https://doi.org/10.1021/acs.chemmater.6b01438.

(152) Abdellahi, A.; Urban, A.; Dacek, S.; Ceder, G. *The Effect of Cation Disorder on the Average Li Intercalation Voltage of Transition-Metal Oxides*. ACS Publications. https://doi.org/10.1021/acs.chemmater.6b00205.

(153) Li, X.; Wang, J.; Zhang, S.; Sun, L.; Zhang, W.; Dang, F.; Seifert, H. J.; Du, Y. Intrinsic Defects in LiMn2O4: First-Principles Calculations. *ACS Omega* **2021**, *6* (33), 21255–21264. https://doi.org/10.1021/acsomega.1c01162.

(154) Xiao, R.; Li, H.; Chen, L. Density Functional Investigation on Li2MnO3. *Chem. Mater.* **2012**, *24* (21), 4242–4251. https://doi.org/10.1021/cm3027219.

(155) Kubota, K.; Asari, T.; Yoshida, H.; Yaabuuchi, N.; Shiiba, H.; Nakayama, M.; Komaba, S. Understanding the Structural Evolution and Redox Mechanism of a NaFeO2–NaCoO2 Solid Solution for Sodium-Ion Batteries. *Adv. Funct. Mater.* **2016**, *26* (33), 6047–6059. https://doi.org/10.1002/adfm.201601292.

(156) Saubanère, M.; McCalla, E.; Tarascon, J.-M.; Doublet, M.-L. The Intriguing Question of Anionic Redox in High-Energy Density Cathodes for Li-Ion Batteries. *Energy Environ. Sci.* **2016**, *9* (3), 984–991. https://doi.org/10.1039/C5EE03048J.

(157) *random — Generate pseudo-random numbers*. Python documentation. https://docs.python.org/3/library/random.html (accessed 2023-08-29).

(158) Fadzil, A. F. M.; Muhammad, F. H. A Study of LiMn(2-X)FexO4 Cathodic Nano Material for Lithium-Ion Batteries. *Adv. Mater. Res.* **2014**, *1043*, 7–11. https://doi.org/10.4028/www.scientific.net/AMR.1043.7.

(159) *Shannon Radii*. http://abulafia.mt.ic.ac.uk/shannon/ptable.php (accessed 2023-07-19).

(160) *Database of Ionic Radii*. http://abulafia.mt.ic.ac.uk/shannon/ (accessed 2023-08-19).

(161) Kawai, H.; Nagata, M.; Tabuchi, M.; Tukamoto, H.; West, A. R. Novel 5 V Spinel Cathode $Li_2FeMn_3O_8$ for Lithium Ion Batteries. *Chem. Mater.* **1998**, *10* (11), 3266–3268. https://doi.org/10.1021/cm9807182.

(162) Kushida, K.; Kuriyama, K. Observation of Li-Atomic Array in Spinel-LiMn2O4 Films Spin-Coated on Si Substrates Using an Atomic Force Microscopy. *Appl. Phys. Lett.* **2000**, *76* (16), 2238–2240. https://doi.org/10.1063/1.126307.

(163) Lee, J. H.; Hong, J. K.; Jang, D. H.; Sun, Y.-K.; Oh, S. M. Degradation Mechanisms in Doped Spinels of LiM0.05Mn1.95O4 (M=Li, B, Al, Co, and Ni) for Li Secondary Batteries. *J. Power Sources* **2000**, *89* (1), 7–14. https://doi.org/10.1016/S0378-7753(00)00375-X.

(164) Reynaud, M.; Serrano-Sevillano, J.; Casas-Cabanas, M. Imperfect Battery Materials: A Closer Look at the Role of Defects in Electrochemical Performance. *Chem. Mater.* **2023**, *35* (9), 3345–3363. https://doi.org/10.1021/acs.chemmater.2c03481.

(165) Zhang, S.; Xu, K.; Jow, R. Study of LiBF[Sub 4] as an Electrolyte Salt for a Li-Ion Battery. *J. Electrochem. Soc.* **2002**, *149*, A586–A590. https://doi.org/10.1149/1.1466857.

(166) Saurel, D.; Pendashteh, A.; Jáuregui, M.; Reynaud, M.; Fehse, M.; Galceran, M.; Casas-Cabanas, M. Experimental Considerations for Operando Metal-Ion Battery Monitoring Using X-Ray Techniques. *Chemistry–Methods* **2021**, *1* (6), 249–260. https://doi.org/10.1002/cmtd.202100009.

(167) Yu, L.; Tian, Y.; Xing, Y.; Hou, C.; Si, Y.; Lu, H.; Zhao, Y. Unraveling the Overlithiation Mechanism of LiMn2O4 and LiFePO4 Using Lithium-Metal Batteries. *Ionics* **2021**, *27* (12), 5021–5035. https://doi.org/10.1007/s11581-021-04211-w.

(168) Kurth, S.; Marques, M. A. L.; Gross, E. K. U. Density-Functional Theory. In *Encyclopedia of Condensed Matter Physics*; Bassani, F., Liedl, G. L., Wyder, P., Eds.; Elsevier: Oxford, 2005; pp 395–402. https://doi.org/10.1016/B0-12-369401-9/00445-9.

(169) Sun, J.; Ruzsinszky, A.; Perdew, J. P. Strongly Constrained and Appropriately Normed Semilocal Density Functional. *Phys. Rev. Lett.* **2015**, *115* (3), 036402. https://doi.org/10.1103/PhysRevLett.115.036402.

(170) Anisimov, V. I.; Solovyev, I. V.; Korotin, M. A.; Czyżyk, M. T.; Sawatzky, G. A. Density-Functional Theory and NiO Photoemission Spectra. *Phys. Rev. B* **1993**, *48* (23), 16929–16934. https://doi.org/10.1103/PhysRevB.48.16929.

(171) Anisimov, V. I.; Zaanen, J.; Andersen, O. K. Band Theory and Mott Insulators: Hubbard U Instead of Stoner I. *Phys. Rev. B* **1991**, *44* (3), 943–954. https://doi.org/10.1103/PhysRevB.44.943.

(172) Dudarev, S. L.; Botton, G. A.; Savrasov, S. Y.; Humphreys, C. J.; Sutton, A. P. Electron-Energy-Loss Spectra and the Structural Stability of Nickel Oxide: An LSDA+U Study. *Phys. Rev. B* **1998**, *57* (3), 1505–1509. https://doi.org/10.1103/PhysRevB.57.1505.

(173) *Phys. Rev. B 71, 035105 (2005) - Linear response approach to the calculation of the effective interaction parameters in the $\mathrm{LDA}+\mathrm{U}$ method*. https://journals.aps.org/prb/abstract/10.1103/PhysRevB.71.035105 (accessed 2023-08-02).

(174) Li, L.; Yu, W.; Jin, C. First-Principles Study of Pressure-Induced Phase Transition in the Strongly Correlated Compound $\mathrm{Y}\mathrm{Cr}{\mathrm{O}}_{4}$. *Phys. Rev. B* **2006**, *73* (17), 174115. https://doi.org/10.1103/PhysRevB.73.174115.

(175) Zhou, F.; Cococcioni, M.; Marianetti, C. A.; Morgan, D.; Ceder, G. First-Principles Prediction of Redox Potentials in Transition-Metal Compounds with

$\mathrm{LDA}+U$. *Phys. Rev. B* **2004**, *70* (23), 235121. https://doi.org/10.1103/PhysRevB.70.235121.

(176) Wang, L.; Maxisch, T.; Ceder, G. Oxidation Energies of Transition Metal Oxides within the $\mathrm{GGA}+\mathrm{U}$ Framework. *Phys. Rev. B* **2006**, *73* (19), 195107. https://doi.org/10.1103/PhysRevB.73.195107.

(177) Jain, A.; Ong, S. P.; Hautier, G.; Chen, W.; Richards, W. D.; Dacek, S.; Cholia, S.; Gunter, D.; Skinner, D.; Ceder, G.; Persson, K. A. Commentary: The Materials Project: A Materials Genome Approach to Accelerating Materials Innovation. *APL Mater.* **2013**, *1* (1), 011002. https://doi.org/10.1063/1.4812323.

(178) Lozano, A.; Escribano, B.; Akhmatskaya, E.; Carrasco, J. Assessment of van Der Waals Inclusive Density Functional Theory Methods for Layered Electroactive Materials. *Phys. Chem. Chem. Phys.* **2017**, *19* (15), 10133–10139. https://doi.org/10.1039/C7CP00284J.

(179) Lander, L.; Reynaud, M.; Carrasco, J.; Katcho, N. A.; Bellin, C.; Polian, A.; Baptiste, B.; Rousse, G.; Tarascon, J.-M. Unveiling the Electrochemical Mechanisms of Li2Fe(SO4)2 Polymorphs by Neutron Diffraction and Density Functional Theory Calculations. *Phys. Chem. Chem. Phys.* **2016**, *18* (21), 14509–14519. https://doi.org/10.1039/C6CP02175A.

(180) Kresse, G.; Joubert, D. From Ultrasoft Pseudopotentials to the Projector Augmented-Wave Method. *Phys. Rev. B* **1999**, *59* (3), 1758–1775. https://doi.org/10.1103/PhysRevB.59.1758.

(181) Yang, Z.; Peng, H.; Sun, J.; Perdew, J. P. More Realistic Band Gaps from Meta-Generalized Gradient Approximations: Only in a Generalized Kohn-Sham Scheme. *Phys. Rev. B* **2016**, *93* (20), 205205. https://doi.org/10.1103/PhysRevB.93.205205.

(182) *CASM Code | Anton Van der Ven Research Lab | Materials Department | UC Santa Barbara*. https://labs.materials.ucsb.edu/vanderven/anton/research/casm-code (accessed 2023-08-02).

(183) Puchala, B.; Thomas, J. C.; Natarajan, A. R.; Goiri, J. G.; Behara, S. S.; Kaufman, J. L.; Van der Ven, A. CASM — A Software Package for First-Principles Based Study of Multicomponent Crystalline Solids. *Comput. Mater. Sci.* **2023**, *217*, 111897. https://doi.org/10.1016/j.commatsci.2022.111897.

(184) Rietveld, H. M. A Profile Refinement Method for Nuclear and Magnetic Structures. *J. Appl. Crystallogr.* **1969**, *2* (2), 65–71. https://doi.org/10.1107/S0021889869006558.

(185) Momma, K.; Izumi, F. VESTA 3 for Three-Dimensional Visualization of Crystal, Volumetric and Morphology Data. *J. Appl. Crystallogr.* **2011**, *44* (6), 1272–1276. https://doi.org/10.1107/S0021889811038970.

(186) Fauth, F.; Peral, I.; Popescu, C.; Knapp, M. The New Material Science Powder Diffraction Beamline at ALBA Synchrotron. *Powder Diffr.* **2013**, *28* (S2), S360–S370. https://doi.org/10.1017/S0885715613000900.

(187) Fauth, F.; Boer, R.; Gil-Ortiz, F.; Popescu, C.; Vallcorba, O.; Peral, I.; Fullà, D.; Benach, J.; Juanhuix, J. The Crystallography Stations at the Alba Synchrotron. *Eur. Phys. J. Plus* **2015**, *130* (8), 160. https://doi.org/10.1140/epjp/i2015-15160-y.